

Quarterly Technical Report

Solid State Research

1991:1

Lincoln Laboratory

MASSACHUSETTS INSTITUTE OF TECHNOLOGY

LEXINGTON, MASSACHUSETTS



Prepared for the Department of the Air Force under Contract F19628-90-C-0002.

Approved for public release; distribution is unlimited.

ADA241025

This report is based on studies performed at Lincoln Laboratory, a center for research operated by Massachusetts Institute of Technology. The work was sponsored by the Department of the Air Force under Contract F19628-90-C-0002.

This report may be reproduced to satisfy needs of U.S. Government agencies.

The ESD Public Affairs Office has reviewed this report, and it is releasable to the National Technical Information Service, where it will be available to the general public, including foreign nationals.

This technical report has been reviewed and is approved for publication.

FOR THE COMMANDER

Hugh L. Southall

Hugh L. Southall, Lt. Col., USAF
Chief, ESD Lincoln Laboratory Project Office

Non-Lincoln Recipients

PLEASE DO NOT RETURN

Permission is given to destroy this document
when it is no longer needed.

MASSACHUSETTS INSTITUTE OF TECHNOLOGY
LINCOLN LABORATORY

SOLID STATE RESEARCH

QUARTERLY TECHNICAL REPORT

1 NOVEMBER 1990 — 31 JANUARY 1991

ISSUED 8 JULY 1991

Approved for public release; distribution is unlimited.

ABSTRACT

This report covers in detail the research work of the Solid State Division at Lincoln Laboratory for the period 1 November 1990 through 31 January 1991. The topics covered are Electrooptical Devices, Quantum Electronics, Materials Research, Submicrometer Technology, High Speed Electronics, Microelectronics, and Analog Device Technology. Funding is provided primarily by the Air Force, with additional support provided by the Army, DARPA, Navy, SDIO, NASA, and DOE.

TABLE OF CONTENTS

Abstract	iii
List of Illustrations	vii
List of Tables	xii
Introduction	xiii
Reports on Solid State Research	xvii
Organization	xxvii
1. ELECTROOPTICAL DEVICES	1
1.1 Buried-Heterostructure InGaAs/GaAs/GaInP Strained-Layer Quantum-Well Lasers ($\lambda = 980$ nm) Fabricated by Mass Transport	1
1.2 Analysis of Vapor Diffusion in Surface-Energy-Induced Mass Transport	4
2. QUANTUM ELECTRONICS	9
2.1 5-GHz Mode Locking of a Nd:YLF Laser with 10-ps Pulses	9
2.2 Theoretical Analysis of the Q-Switched Microchip Laser	12
2.3 Theoretical Analysis of the Polarization-Switchable Microchip Laser	17
2.4 Microchip Laser Arrays	18
2.5 Single-Axial-Mode Intracavity-Doubled Nd:YAG Laser	22
2.6 CW Operation of a Diode-Pumped Rotating Nd:Glass Disk Laser	25
2.7 High-Average-Intensity Sum-Frequency Mixing of Nd:YAG Laser Radiation in LiB_3O_5	27
3. MATERIALS RESEARCH	33
3.1 Long-Wavelength $\text{Ge}_x\text{Si}_{1-x}/\text{Si}$ Heterojunction Infrared Detectors and 400×400 -Element Imager Arrays	33
3.2 High-Efficiency, High-Power GaInAsSb/AlGaAsSb Diode Lasers Emitting at $2.3 \mu\text{m}$	37
3.3 Role of GaAs Bounding Layers in OMVPE Growth of Strained-Layer InGaAs/AlGaAs Diode Lasers	40
4. SUBMICROMETER TECHNOLOGY	49
4.1 Large-Area Mosaic Diamond Films Approaching Single-Crystal Quality	49
4.2 Silylation of Resists Exposed by Focused Ion Beams	52
5. HIGH SPEED ELECTRONICS	59
5.1 GaAs MISFET with a Low-Temperature-Grown Epitaxial Layer as the Insulator	59
5.2 Magneto-optical Study of Donor Level Crossing in Tipped GaAs/AlGaAs Quantum Wells	62

TABLE OF CONTENTS (Continued)

6.	MICROELECTRONICS	67
6.1	Improvements to an Analog-Signal-Processing Chain for a CCD Camera	67
6.2	Fabrication Process for Non-Overlapping-Gate CCDs	69
7.	ANALOG DEVICE TECHNOLOGY	73
7.1	Off-Axis Sputter Deposition of $\text{YBa}_2\text{Cu}_3\text{O}_{7-x}$	73
7.2	Integration of Superconductive Devices for Analog-Signal-Processing Applications	77

LIST OF ILLUSTRATIONS

Figure No.		Page
1-1	SEM of a cleaved and stained transverse cross section of the buried heterostructure. A drawing of this view is provided as an aid to understanding the micrograph.	2
1-2	Threshold current density vs inverse cavity length for broad-area (225 μm wide) devices. Comparison is made with the lowest reported threshold current densities [6] (solid line).	2
1-3	Power per facet vs current for buried-heterostructure devices in pulsed operation, showing operation to ~ 35 times threshold current and facet power densities of $\sim 15 \text{ MW/cm}^2$.	3
1-4	Illustration of the present model of surface-energy-induced mass transport via vapor diffusion.	4
2-1	Schematic of the mode-locked Nd:YLF laser. The distance between the mirrors is 1.6 cm, and the output coupler has a 5-cm radius of curvature and 2% transmission at 1.053 μm . The Y axis of the LiTaO ₃ is along the laser optical axis, and the Nd:YLF crystal is 3 mm long.	10
2-2	Autocorrelation of the mode-locked Nd:YLF laser output. For this measurement, a beamsplitting mirror in the autocorrelator splits the incoming beam into two, both beams pass twice through a rotating prism, and the beams are recombined on the beamsplitter and frequency doubled in MgO-doped LiNbO ₃ .	10
2-3	Fabry-Perot spectra of the Nd:YLF laser. (a) Under free-running conditions a number of modes are observed; spatial hole burning in the Nd:YLF allows simultaneous operation of these modes. (b) Under mode-locked conditions all of the modes within the bandwidth observed under free-running conditions lase; these modes are separated by 5.37 GHz.	11
2-4	Normalized optical intensity X of a Q-switched pulse obtained for a normalized inversion density Y_{0+} of 2, 3, 4, 5, 6, 7, 8, 9, and 10 as a function of normalized time T , calculated for $X_0 = 10^{-14}$.	13
2-5	Normalized peak pulse intensity X_p as a function of normalized inversion density Y_{0+} .	14
2-6	Normalized pulse width T_w (FWHM) as a function of normalized inversion density Y_{0+} .	14
2-7	Pulse width t_w as a function of the cavity lifetime τ_c after Q-switching.	15
2-8	Peak output intensity I_{po} as a function of the cavity lifetime τ_c after Q-switching for negligible parasitic loss.	16

LIST OF ILLUSTRATIONS (Continued)

Figure No.		Page
2-9	(a) Side view and (b) top view of the geometry used to pump the microchip laser array. The magnification of the cylindrical lenses was 10 times in the dimension perpendicular to the diode junction and unity in the dimension parallel to the junction. The individual 6- μm diodes were spaced 1 mm on center.	19
2-10	Near-field pattern of the output from the microchip laser array.	20
2-11	Far-field pattern of the output from the microchip laser array. The three black dots correspond to the centroid of the outputs from the three individual elements.	21
2-12	Round-trip transmission for a cavity containing a polarizer P and a waveplate W between two mirrors M as a function of ϕ . The curves are for three different values of single-pass power transmission for the lossy polarization through the polarizer, $T = 0$, $T = 0.72$, and $T = 0.51$. These values of T represent an ideal polarizer, a single Brewster-angle surface on YAG, and two Brewster-angle surfaces on YAG, respectively. The axial modes are also plotted assuming that $L/\Delta nl = 30$.	22
2-13	Schematic of the single-axial-mode intracavity-doubled Nd:YAG laser. The axes of the KTP are oriented 45° to the axes of the Brewster-angle faces. The Nd:YAG was placed close to the mirror with 5-cm radius of curvature, and the KTP was placed close to the mirror with 50-cm radius of curvature.	23
2-14	Output of the scanning confocal interferometer and a monitor photodiode under (a) single-mode operation and (b) multimode operation.	24
2-15	Schematic of the end-pumped rotating Nd:glass disk laser. M1 and M2 serve as the cavity mirrors. Lenses L1 and L2 collimate the diode radiation and focus it into the disk.	26
2-16	1.054- μm output power vs rotation rate (linear velocity), with absorbed pump power as a parameter.	26
2-17	Relative doubling and mixing efficiencies of LiB_3O_5 as a function of temperature.	29
2-18	Schematic of the 1.06- and 1.32- μm Nd:YAG laser system for sum-frequency mixing in LiB_3O_5 .	30
2-19	Sum-frequency-mixing efficiency as a function of total input power. In this experiment, only the output of the oscillators was used. The resulting data are roughly linear except for the last data point, at which we were no longer able to maintain the ratio of the 1.06- to 1.32- μm radiation at 1.24. The last data point corresponds to the generation of 5.2 W of 589-nm radiation with an input of 21.5 and 12.5 W of 1.06- and 1.32- μm radiation, respectively.	31

LIST OF ILLUSTRATIONS (Continued)

Figure No.		Page
3-1	Schematic cross section of single pixel of GeSi infrared focal plane array.	34
3-2	Plots of J/T^2 vs $1/T$ for three GeSi detectors operated at a reverse voltage V_R of 1 V.	35
3-3	Quantum efficiency as a function of wavelength for the detectors of Figure 3-2 and an IrSi detector.	35
3-4	Uncorrected thermal images obtained with 400×400 GeSi imager array for (a) a 10-K test pattern and (b) a man's face. The imager was operated at a frame rate of 30 Hz with an $f/2.35$ cold shield and a $7.5\text{-}\mu\text{m}$ long-pass filter.	36
3-5	Emission spectrum of GaInAsSb/AlGaAsSb diode laser for pulsed operation at room temperature.	38
3-6	Light output vs current for a laser $300\text{ }\mu\text{m}$ wide by $300\text{ }\mu\text{m}$ long.	38
3-7	Dependence of threshold current density on cavity length.	39
3-8	Dependence of inverse differential quantum efficiency on cavity length.	39
3-9	Dependence of threshold current density on temperature for a laser $300\text{ }\mu\text{m}$ wide by $300\text{ }\mu\text{m}$ long.	40
3-10	Schematic diagram showing structure of InGaAs/AlGaAs GRINSCH-SQW diode laser.	41
3-11	Scanning electron micrographs showing surface morphology of (a) GRINSCH-SQW structure A and (b) GRINSCH-SQW structure E.	43
3-12	Room-temperature PL spectra for GRINSCH-SQW structures A, C, D, and E. For each sample the thicknesses (in nanometers) of the lower and upper GaAs bounding layers, respectively, are given by the first and second numbers in parentheses (see Table 3-1).	44
3-13	Schematic cross-sectional diagram of InGaAs/GaAs test structure.	45
3-14	Scanning electron micrographs showing surface morphology of (a) test-structure sample A and (b) test-structure sample B.	45
3-15	Room-temperature PL spectra for test-structure samples A and B.	46
3-16	Depth profiles of In concentration, obtained by Auger electron spectroscopy combined with Ar-ion sputtering, for test-structure samples A and B.	46

LIST OF ILLUSTRATIONS (Continued)

Figure No.		Page
4-1	X-ray diffraction from the (400) plane of diamond seeds on a pit-patterned Si substrate as a function of the angle between the $\langle 400 \rangle$ axis of the Si substrate and the axis bisecting the primary and diffracted x-ray beams. The tip angle (HWHM) of the diamond seeds is $\sim 0.35^\circ$. The x-ray diffraction from the Si substrate is intended to show the resolution of the system and is not to scale.	50
4-2	(a) X-ray diffraction from the {311} planes of diamond on a seeded substrate as a function of rotation in the substrate plane. (b) Expanded view of the x-ray diffraction intensity centered about 270° . The x-ray diffraction from a (311) Si plane is superimposed.	51
4-3	Scanning electron micrographs of (a) a diamond-seeded Si substrate having an array of pyramidal pits with one unseeded pit in the second column from the right, and (b) a similar sample after epitaxial diamond overgrowth to $\sim 240 \mu\text{m}$ (80 h), where the effect of missing seeds can be seen as holes in the film. The micrographs are to the same scale.	52
4-4	Schematic representation of the process for silylation of FIB-exposed resists.	53
4-5	Scanning electron micrograph of 80- and 100-nm lines patterned in SAL 601 with a single beam pass of 240-keV Be^{++} at a dose of 8 and 9×10^{13} ions/cm ² , respectively. Silylation was carried out at 100°C for this sample.	55
4-6	Scanning electron micrograph of a $0.5\text{-}\mu\text{m}$ line patterned in SAL 601 using 240-keV Be^{++} at a dose of 4×10^{13} ions/cm ² . The pattern changes from an isolated line to one separated from $5 \times 5\text{-}\mu\text{m}$ exposed areas by $0.3 \mu\text{m}$ on either side.	56
5-1	Schematic cross section of the epitaxial layer structure of the GaAs MISFET.	59
5-2	$I_{\text{DS}}\text{-}V_{\text{DS}}$ characteristics of a $600\text{-}\mu\text{m}$ -wide GaAs MISFET. The upper trace is for $V_{\text{GS}} = 2 \text{ V}$.	60
5-3	Measured output power and power-added efficiency vs input power for a GaAs MISFET.	61
5-4	Photoconductivity spectra obtained by sweeping the magnetic field at fixed laser frequency. The arrows indicate the $1s \rightarrow 2p_{+1}$ transitions. Other prominent features that appear in the spectra are labeled A, B, and C.	63
5-5	Plots of peak positions of the transition energy vs magnetic field for the $1s \rightarrow 2p_{+1}$ transition. The theoretical curves for the Faraday ($\theta = 0^\circ$) and Voigt ($\theta = 90^\circ$) geometries are shown, with the corresponding points representing experimental results.	64

LIST OF ILLUSTRATIONS (Continued)

Figure No.		Page
5-6	(a) Plots of peak positions of the transition energy vs magnetic field, showing the theoretical curves for the Faraday geometry ($\theta = 0^\circ$) and the theoretical curves and experimental points for $\theta = 16^\circ$. (b) Plots of peak positions of the transition energy vs magnetic field, showing the theoretical curves for the Faraday geometry ($\theta = 0^\circ$) and the theoretical curves and experimental points for $\theta = 31^\circ$.	65
6-1	Block diagram and schematic of (a) original and (b) redesigned analog-signal-processing chain starting with the CCD output as the analog chain input and ending at the A/D converter at the chain output.	68
6-2	Major patterning steps of the non-overlapping-gate CCD process. Shown is a cross section of the wafer (a) after the polysilicon, pad oxide, and nitride deposition, the photoresist definition, and the nitride etch and photoresist strip, (b) after the LOCOS process, demonstrating oxide encroachment under the nitride, and (c) after the etch of the nitride and the etch of the polysilicon using the oxide as a mask.	70
6-3	Cross section of the finished non-overlapping-gate CCD, showing the submicrometer spacings.	70
6-4	(a) Top view of array of CCD polysilicon electrodes. (b) Expanded view showing etched submicrometer spacing between the electrodes.	71
6-5	Channel potential under two successive electrodes separated by submicrometer spacings of (a) $0.4 \mu\text{m}$ and (b) $0.8 \mu\text{m}$. An effective oxide surface charge of 10^{11} charges/cm ² and a gate-oxide thickness of 800 nm were used.	71
7-1	Summary of the deposition conditions used to produce in-situ superconducting YBCO. The solid line indicates the perovskite stability line established by Bormann and Nölting [3]. Under equilibrium conditions the perovskite structure of bulk YBCO is stable above the line and unstable below it.	73
7-2	(a) Variation of T_c and J_c with substrate temperature for films deposited using an oxygen pressure of 10 mTorr. The argon pressure was 150 mTorr. (b) Variation of T_c with oxygen pressure for films deposited at substrate temperatures of 760, 700, and 640°C. The argon pressure was adjusted to maintain a total pressure of 160 mTorr.	75
7-3	X-ray diffraction pattern of (a) a <i>c</i> -axis-oriented film deposited at 780°C using an oxygen pressure of 10 mTorr, and (b) an <i>a</i> -axis-oriented film deposited at 640°C using an oxygen pressure of 20 mTorr.	76
7-4	End view of the cryogenic probe, with the superconductive dispersive delay line (circular package) and time-integrating correlator (rectangular package) mounted.	77

LIST OF ILLUSTRATIONS (Continued)

Figure No.		Page
7-5	Block diagram showing the integration of superconductive components to measure the autocorrelation of wideband chirp waveforms.	78
7-6	Block diagram of time-integrating correlator showing the on-chip integration of analog and digital superconductive circuitry.	79
7-7	(a) Reconstructed output of the time-integrating correlator, showing the measured autocorrelation of a 2.6-GHz chirp waveform. (b) Mathematical calculation of the chirp autocorrelation function.	80

LIST OF TABLES

Table No.		Page
2-1	Phase-Matching Characteristics for Frequency Summing of 1.06- and 1.32- μm Radiation in Several Nonlinear Crystals	28
3-1	Effect of Upper and Lower GaAs Bounding Layers on Laser Structures	42
4-1	Sensitivity of SAL 601 Resist for a Range of Ion Species	54
4-2	Comparison of Observed and Projected Electron-Beam and Ion-Beam Writing Times	57

INTRODUCTION

1. ELECTROOPTICAL DEVICES

Buried-heterostructure quantum-well lasers have been fabricated for the first time by mass transport using $\text{Ga}_{0.51}\text{In}_{0.49}\text{P}$ as the cladding material, which transports to encapsulate a separate-confinement optical cavity of GaAs and a quantum well of strained $\text{In}_{0.18}\text{Ga}_{0.82}\text{As}$. The high performance of these devices that emit at 980-nm wavelength makes them attractive candidates for pumping Er-doped fiber amplifiers.

A simple analytical model has been developed for surface-energy-induced mass transport via vapor diffusion. The predicted decay rate of a sinusoidal surface profile shows a familiar fourth-power spatial-wavelength dependence but with an additional dependence on an effective channel width for diffusion, which is related to both the wafer-cover separation and the spatial wavelength of the surface profile.

2. QUANTUM ELECTRONICS

A LiTaO_3 phase modulator placed inside a Nd:YLF laser cavity has been used to implement frequency-modulated mode locking of the laser at 5.37 GHz. Pulse durations of 10 ps were obtained with only 80 mW of microwave drive power.

Theoretical modeling has resulted in explicit expressions for the minimum output pulse width and maximum output power obtainable from a Q-switched laser for a given CW pump power and pulse repetition rate. The expressions indicate that Nd:YAG microchip lasers pumped with diode lasers can be Q-switched to produce pulses with a full width at half-maximum of < 100 ps and peak power > 100 kW.

A rate-equation analysis has indicated that it may be difficult to switch the polarization of a polarization-switchable Nd:YAG microchip laser at rates in excess of several megahertz. However, because of its small size and potential for low-cost mass production, the polarization-switchable microchip laser may find applications in specialized areas of optical communications.

Diode-pumped microchip laser arrays have been shown to produce parallel output beams that incoherently overlap in the far field. Since each element in the microchip array performs as an independent device, such arrays can be scaled to arbitrary sizes, representing a new approach to robust, high-power laser sources.

A diode-pumped, single-axial-mode intracavity-doubled laser has been demonstrated using a cavity consisting of only two mirrors, a Brewster-angle-cut piece of Nd:YAG, and a KTP doubling crystal. Up to 4-mW single-ended output power has been obtained for 260-mW incident power on the Nd:YAG.

A diode-pumped, CW rotating Nd:glass disk laser has been demonstrated. With 2 W of absorbed pump power and at the optimum rotation rate of 2.5 Hz the laser operated in the TEM_{00} mode and had a CW output power of 0.55 W.

Efficient sum-frequency mixing of 1.06- and 1.32- μm Nd:YAG laser radiation with relatively low input peak powers has been achieved by focusing the radiation into a LiB_3O_5 crystal. The crystal was subjected to an average intensity at the focus of $0.3 \text{ MW}/\text{cm}^2$ without sustaining either photorefractive or physical damage.

3. MATERIALS RESEARCH

Heterojunction $\text{Ge}_x\text{Si}_{1-x}/\text{Si}$ internal photoemission infrared detectors exhibiting nearly ideal thermionic-emission dark-current characteristics have been fabricated with cutoff wavelengths out to $16\text{ }\mu\text{m}$. High-quality imaging without uniformity correction has been demonstrated in the long-wavelength infrared spectral band for 400×400 -element focal plane arrays consisting of $\text{Ge}_{0.44}\text{Si}_{0.56}/\text{Si}$ detectors, having a cutoff wavelength of $9.3\text{ }\mu\text{m}$, and monolithic CCD readout circuitry.

Double-heterostructure $\text{Ga}_{0.84}\text{In}_{0.16}\text{As}_{0.14}\text{Sb}_{0.86}/\text{Al}_{0.5}\text{Ga}_{0.5}\text{As}_{0.04}\text{Sb}_{0.96}$ diode lasers emitting at $2.27\text{ }\mu\text{m}$ have been grown by molecular beam epitaxy on GaSb substrates. For pulsed operation of broad-stripe lasers $300\text{ }\mu\text{m}$ wide, differential quantum efficiency as high as 50% and output power as high as 900 mW per facet were obtained for a cavity length of $300\text{ }\mu\text{m}$, and threshold current density as low as 1.5 kA cm^{-2} was obtained for a cavity length of $700\text{ }\mu\text{m}$.

Experiments on the organometallic vapor phase epitaxy growth of strained-layer InGaAs/AlGaAs single-quantum-well diode laser structures, in which the InGaAs quantum-well layer is sandwiched between two thin GaAs bounding layers, have shown that laser performance is influenced more by the upper bounding layer than by the lower bounding layer. By using Auger analysis in combination with Ar-ion sputtering to determine the composition depth profile of InGaAs/GaAs test structures, it has been found that the role of the upper bounding layer is to prevent the evaporation of In from the InGaAs quantum-well layer during the interval when the growth temperature is increased prior to deposition of the upper AlGaAs cladding layer.

4. SUBMICROMETER TECHNOLOGY

Thin films of nearly single-crystal diamond have been grown on silicon substrates using oriented faceted diamond seeds. The orientation of the seeds was achieved by etching appropriate relief structures in the substrates.

A process has been developed for silylation of novolac-based resists exposed by focused-ion-beam lithography. Resolution better than 100 nm has been demonstrated, without noticeable proximity effects.

5. HIGH SPEED ELECTRONICS

A GaAs metal-insulator-semiconductor field-effect transistor (MISFET) has been developed that uses a gate insulator made of high-resistivity GaAs grown by molecular beam epitaxy at low temperature (200°C). At 1.1 GHz this MISFET demonstrated a power density of 1.57 W/mm of gate width, which is the highest reported for any GaAs-based FET.

A photoconductivity method has been used to study the anticrossing between the $2p_{+1}$ and $2p_0$ levels of Si donors situated near the center of a GaAs quantum well. This work represents the first known observation of an anticrossing between two p-like donor levels in a quantum well.

6. MICROELECTRONICS

The analog-signal-processing chain of a high-frame-rate charge-coupled device (CCD) camera has been redesigned to take advantage of the low-noise performance of the on-chip output amplifier. These changes have resulted in an improved signal-to-noise ratio and an output voltage drift that is below the CCD amplifier noise.

The lateral-encroachment property of the local oxidation of silicon has been used to form an oxide mask over polysilicon with $0.4\text{-}\mu\text{m}$ -wide spacings between electrodes, starting from $1.5\text{-}\mu\text{m}$ -wide photoresist lines defined by a conventional projection aligner. This technology has led to the fabrication of a three-phase non-overlapping-gate CCD with a single layer of polysilicon and a measured charge-transfer efficiency of 0.9998.

7. ANALOG DEVICE TECHNOLOGY

Single-target off-axis magnetron sputtering has been used to deposit superconductive YBCO thin films in situ, over a wide range of deposition conditions. The best film properties measured include a transition temperature ($R = 0$) of 90.5 K and a critical current density of $1.7 \times 10^6 \text{ A/cm}^2$ at 77 K.

Two separately fabricated superconductive devices, a chirp waveform generator and a time-integrating correlator, have been integrated into a prototype subsystem suitable for use in spread-spectrum communications.

REPORTS ON SOLID STATE RESEARCH

1 November 1990 Through 31 January 1991

PUBLICATIONS

20-GHz Optical Analog Link Using an External Modulator	G. E. Betts C. H. Cox III K. G. Ray	<i>IEEE Photon. Technol. Lett.</i> 2 , 923 (1990)
Room-Temperature CW Operation of GaAs/AlGaAs Diode Lasers Grown on Silicon-on-Insulator Wafers	H. K. Choi N. H. Karam* C. A. Wang	<i>Proceedings of the IEEE Lasers and Electro-Optics Society Annual Meeting</i> (IEEE, New York, 1990), p. 490
III-V Diode Lasers for New Emission Wavelengths	H. K. Choi C. A. Wang S. J. Eglash	<i>Lincoln Lab. J.</i> 3 , 395 (1990)
Two-Dimensional Surface-Emitting Arrays of Diode Lasers	J. P. Donnelly	<i>Lincoln Lab. J.</i> 3 , 361 (1990)
Semiconductor Integrated Optic Devices	J. P. Donnelly F. J. Leonberger*	In <i>Guided-Wave Optoelectronics</i> , edited by T. Tamir (Springer-Verlag, New York, 1990), p. 403
Diode-Pumped Solid-State Lasers	T. Y. Fan	<i>Lincoln Lab. J.</i> 3 , 413 (1990)
Starting Dynamics of Additive Pulse Mode-Locking in the TiAl ₂ O ₃ Laser	J. Goodberlet * J. Wang* J. G. Fujimoto* P. A. Schulz	<i>Opt. Lett.</i> 15 , 1300 (1990)
Silylation Processes Based on Ultraviolet Laser-Induced Crosslinking	M. A. Hartney M. Rothschild R. R. Kunz D. J. Ehrlich D. C. Shaver	<i>J. Vac. Sci. Technol. B</i> 8 , 1476 (1990)

*Author not at Lincoln Laboratory.

Plasma-Deposited Organosilicon Thin Films as Dry Resists for Deep Ultraviolet Lithography	M. W. Horn S. W. Pang M. Rothschild	<i>J. Vac. Sci. Technol. B</i> 8 , 1493 (1990)
Linearization of an Interferometric Modulator at Microwave Frequencies by Polarization Mixing	L. M. Johnson H. V. Roussell	<i>IEEE Photon. Technol. Lett.</i> 2 , 810 (1990)
Polysilyne Thin Films as Resists for Deep Ultraviolet Lithography	R. R. Kunz M. W. Horn R. B. Goodman P. A. Bianconi* D. A. Smith* C. A. Freed*	<i>J. Vac. Sci. Technol. B</i> 8 , 1820 (1990)
Microlens Integration with Diode Lasers and Coherent Phase Locking of Laser Arrays	Z. L. Liao V. Diadiuk J. N. Walpole	<i>Lincoln Lab. J.</i> 3 , 385 (1990)
Passive Microwave Device Applications of High T_c Superconducting Thin Films	W. G. Lyons R. S. Withers	<i>Microwave J.</i> 33 (11), 85 (1990)
Laser Development at Lincoln Laboratory	I. Melngailis	<i>Lincoln Lab. J.</i> 3 , 347 (1990)
Plasma-Deposited Amorphous Carbon Films as Planarization Layers	S. W. Pang M. W. Horn	<i>J. Vac. Sci. Technol. B</i> 8 , 1980 (1990)
Polyimide Optical Waveguides Fabricated with Electron Beam Lithography	M. J. Rooks H. V. Roussell L. M. Johnson	<i>Appl. Opt.</i> 29 , 3880 (1990)
Fast Electro-optic Wavelength Selection and Frequency Modulation in Solid State Lasers	P. A. Schulz	<i>Lincoln Lab. J.</i> 3 , 463 (1990)
Lateral-Mode Selectivity in External-Cavity Diode Lasers with Residual Facet Reflectivity	W. F. Sharfin A. Mooradian	<i>IEEE J. Quantum Electron.</i> 26 , 1756 (1990)
High-Speed Optical Interconnections Between Digital Circuits	D. Z. Tsang	<i>Proc. SPIE</i> 1291 , 218 (1990)

*Author not at Lincoln Laboratory.

Titanium Sapphire Lasers	K. F. Wall A. Sanchez	<i>Lincoln Lab. J.</i> 3 , 447 (1990)
AlInGaAs/AlGaAs' Strained Single-Quantum-Well Diode Lasers	C. A. Wang J. N. Walpole L. J. Missaggia H. K. Choi J. P. Donnelly	<i>Proceedings of the IEEE Lasers and Electro-Optics Society Annual Meeting</i> (IEEE, New York, 1990), p. 650
Electrical Characterization of Zn ⁺ and P ⁺ Co-implanted InP:Fe	J. D. Woodhouse M. C. Gaidis J. P. Donnelly	<i>Solid-State Electron.</i> 33 , 1089 (1990)
Microchip Lasers	J. J. Zayhowski	<i>Lincoln Lab. J.</i> 3 , 427 (1990)

ACCEPTED FOR PUBLICATION

High-Power-Density GaAs MISFET's with a Low-Temperature-Grown Epitaxial Layer as the Insulator	C. L. Chen F. W. Smith B. J. Clifton L. J. Mahoney M. J. Manfra A. R. Calawa	<i>IEEE Electron Device Lett.</i>
Ultraviolet, Visible and Infrared Response of PtSi Schottky-Barrier Detectors Operated in the Front-Illumination Mode	C. K. Chen B-Y. Tsaur B. A. Nechay	<i>IEEE Trans. Electron Devices</i>
Efficient Coupling of Multiple Diode Laser Arrays to an Optical Fiber by Geometric Multiplexing	T. Y. Fan	<i>Appl. Opt.</i>
Diamond Transistor Performance and Fabrication	M. W. Geis	<i>IEEE Electron Device Lett.</i>
Suppression of Laser Spiking by Intracavity Second-Harmonic Generation	T. H. Jeys	<i>Appl. Opt.</i>
Prevention of In Evaporation and Preservation of Smooth Surface in Thermal Annealing and Mass Transport of InP	Z. L. Liao	<i>Appl. Phys. Lett.</i>

Surface Impedance Measurements
of Superconducting NbN Films

D. E. Oates
A. C. Anderson
C. C. Chin
J. S. Derov*
G. Dresselhaus*
M. S. Dresselhaus*

Phys. Rev. B

Operation of a Coherent Ensemble of
Five Diode Lasers in an External
Cavity

R. H. Rediker
K. A. Rauschenbach
R. P. Schloss

IEEE J. Quantum Electron.

Frequency-Modulated Nd:YAG Laser

P. A. Schulz
S. R. Henion

Opt. Lett.

Liquid-Nitrogen-Cooled TiAl_2O_3
Laser

P. A. Schulz
S. R. Henion

IEEE J. Quantum Electron.

PRESENTATIONS[†]

Buried-Heterostructure InGaAs/GaAs/
GaInP Strained-Layer Quantum-Well
Lasers Fabricated by Mass Transport

Z. L. Liao
S. C. Palmateer
S. H. Groves
J. N. Walpole

1-Watt CW Semiconductor Diode
Laser Amplifiers

C. D. Nabors
R. L. Aggarwal
H. K. Choi
C. A. Wang
A. Mooradian

Surface-Emitting Diode Lasers with
Integrated Beam Deflectors

R. C. Williamson

Efficient Coupling of Multiple Diode
Laser Arrays to an Optical Fiber

T. Y. Fan

Solid-State Lasers Pumped by
Advanced Diode Laser Sources

T. Y. Fan

IEEE/Lasers and Electro-Optics
Society Annual Meeting,
Boston, Massachusetts,
4-9 November 1990

OSA Annual Meeting,
Boston, Massachusetts,
4-9 November 1990

*Author not at Lincoln Laboratory.

[†]Titles of presentations are listed for information only. No copies are available for distribution.

Ultrashort Pulse Generation with Additive Pulse Modelocking in Solid State Lasers	J. Goodberlet* J. Jacobson* G. Gabetta* P. A. Schulz T. Y. Fan J. Fujimoto*	} OSA Annual Meeting, Boston, Massachusetts, 4-9 November 1990
Diode-Pumped Electro-optically-Tuned, Single-Frequency Nd:YAG Laser	S. R. Henion P. A. Schulz	
TiAl ₂ O ₃ Lasers: Electro-optical Tuning of a Single-Frequency Laser and the Potential for High Average Power Oscillators	P. A. Schulz	
Diamond Transistors	M. W. Geis	Second Annual Diamond Technology Workshop, Detroit, Michigan, 6 November 1990
Efficient 1 Gb/s Free-Space Optical Interconnections	D. Z. Tsang	GOMAC 1990, Las Vegas, Nevada, 6-8 November 1990
Surface Impedance Measurements of YBa ₂ Cu ₃ O _{7-x} Thin Films in Stripline Resonators	D. E. Oates A. C. Anderson	2nd International Symposium on Superconductivity, Sendai, Japan, 6-9 November 1990
Microwave and Millimeter-Wave Resonant Tunneling Devices	T. C. L. G. Sollner E. R. Brown W. D. Goodhue	Lincoln Laboratory Technical Seminar Series: Georgia Institute of Technology, Atlanta, Georgia, 9 November 1990; University of Pittsburgh, Pittsburgh, Pennsylvania, 19 November 1990; Massachusetts Institute of Technology, Cambridge, Massachusetts, 24 January 1991

*Author not at Lincoln Laboratory.

Dry Chemical Etching of GaAs
in an OMVPE Reactor

Techniques for Intrinsic Gain
in Analog Fiber-Optic Links

Excimer Processing
Program Review

Buried-Heterostructure InGaAs/GaAs/
GaInP Strained-Layer Quantum-Well
Lasers Fabricated by Mass Transport

A CCD Parallel Processing
Architecture and Simulation of
CCD Implementation of the
Neocognitron

Cylindrical Magnetron Sputtering of
Y-Ba-Cu-O Superconducting Films

Substrate Temperature Measurements
in High- T_c Superconductor Film
Deposition

MBE Growth of GaInAsSb/AlGaAsSb
Double Heterostructures for Diode
Lasers Emitting Beyond 2 μm

C. W. Krueger
M. Flytzani-
Stephanopoulos*
R. A. Brown*
C. A. Wang

C. H. Cox III

D. C. Shaver
M. Rothschild
M. W. Horn
M. A. Hartney
R. R. Kunz

J. N. Walpole

M. L. Chuang
A. M. Chiang

A. C. Anderson
R. L. Slattery
L. S. Yu-Jahnes
A. C. Westerheim

B. I. Choi*
A. C. Anderson
M. I. Flik*

S. J. Eglash
H. K. Choi
G. W. Turner
M. C. Finn

1990 Meeting of the American
Institute of Engineers,
Chicago, Illinois,
11-16 November 1990

Lincoln Laboratory
Technical Seminar Series,
Drexel Institute of Technology,
Philadelphia, Pennsylvania,
14 November 1990

Program Technical Review,
Lincoln Laboratory,
15 November 1990

Seminar, Raytheon Company,
Lexington, Massachusetts,
21 November 1990

IEEE Neural Information
Processing Systems 1990,
Denver, Colorado,
26-29 November 1990

1990 Fall Meeting of the
Materials Research Society,
Boston, Massachusetts,
26-30 November 1990

*Author not at Lincoln Laboratory.

Photoreactions in Polyalkylsilynes
Induced by ArF-Laser Irradiation

R. R. Kunz
M. W. Horn
P. A. Bianconi*
D. A. Smith*
C. A. Freed*

Use of Ion Scattering Spectroscopy
to Monitor the Nb Target Nitridation
During Reactive Sputtering

D. J. Lichtenwalner
A. C. Anderson
D. A. Rudman*

Surface Impedance Measurements
of Superconducting NbN Films

D. E. Oates
A. C. Anderson
C. C. Chin
J. S. Derov*
G. Dresselhaus*
M. S. Dresselhaus*

Off-Axis Sputter Deposition of
 $\text{YBa}_2\text{Cu}_3\text{O}_{7-x}$: The Role of
Deposition Temperature and
Oxygen

A. C. Westerheim
L. S. Yu-Jahnes
A. C. Anderson
M. J. Cima*

On the Role of Atomic Oxygen in the
Formation of Superconducting
Y-Ba-Cu-O Films

L. S. Yu-Jahnes
A. C. Westerheim
A. C. Anderson
M. J. Cima*

OMVPE of GaAs/AlGaAs and
InGaAs/AlGaAs for Quantum-
Well Diode Lasers

C. A. Wang

1990 Fall Meeting of the
Materials Research Society,
Boston, Massachusetts,
26-30 November 1990

Optical Interconnections Between
Digital Circuits

D. Z. Tsang

Lincoln Laboratory
Technical Seminar Series,
University of Illinois,
Champaign, Illinois,
28 November 1990

OMVPE of GaAs/AlGaAs and
InGaAs/AlGaAs for Quantum-
Well Diode Lasers

C. A. Wang

Lincoln Laboratory
Technical Seminar Series,
Rensselaer Polytechnic Institute,
Troy, New York,
29 November 1990

Heterostructure Seminar Series,
Cambridge, Massachusetts,
3 December 1990

*Author not at Lincoln Laboratory.

Silylation Using Focused Ion Beam Lithography	M. A. Hartney D. C. Shaver M. I. Shepard* J. S. Huh* J. Melngailis	} Second U.S. Japan Seminar on Focused Ion Beams, Portland, Oregon, 3-7 December 1990
Increase in Silicon CCD Speed with Focused-Ion-Beam Implanted Channels	A. L. Lattes S. C. Munroe M. M. Seaver J. E. Murguia* M. I. Shepard* J. Melngailis	
Resonant-Tunneling Devices and Circuits	T. C. L. G. Sollner	Advanced Heterostructure Transistors Conference, Keauhou Kona, Hawaii, 3-8 December 1990
Bulk-Wave Transduction at 1 GHz Using Volume-Holographic Gratings in Lithium Niobate	R. B. Koo* D. E. Oates H. A. Haus*	1990 IEEE Ultrasonics Symposium, Honolulu, Hawaii, 4-7 December 1990
Multiple-Quantum-Well Optoelectronic Devices	K. B. Nichols	Lincoln Laboratory Technical Seminar Series, University of Illinois, Champaign, Illinois, 5 December 1990
Electronic Aspects of Superconducting Thin Films	A. C. Anderson	Lincoln Laboratory Technical Seminar Series, Dartmouth College, Hanover, New Hampshire, 6 December 1990
Application of Analog Fiber-Optic Links to the Advanced Over-the-Horizon Radar System	C. H. Cox III	} 1st Annual DARPA/RADC Symposium on Photonics Systems for Antenna Applications, Monterey, California, 13-14 December 1990
Overview of Integrated-Optic Modulators for Antenna Applications	C. H. Cox III	

*Author not at Lincoln Laboratory.

Consortium for Superconducting Electronics: Overview of Technical Programs	R. W. Ralston	Meeting, Boston Chapter, IEEE Electron Devices Society, Waltham, Massachusetts, 20 December 1990
High- T_c Microstrip Filters and Delay Lines	W. G. Lyons R. S. Withers	2nd Nordic Symposium on Superconductivity, Roeros, Norway, 7-11 January 1991
Surface Impedance Measurements of $\text{YBa}_2\text{Cu}_3\text{O}_{7-x}$ Thin Films in Stripline Resonators	R. S. Withers D. E. Oates A. C. Anderson	Seminar, Kernforschungsanlage, Juelich, Germany, 15 January 1991
Dry Etching	R. R. Paladugu	Seminar, M/A-COM, Burlington, Massachusetts, 17 January 1991
Wideband Analog Signal Processing with Superconducting Circuits	R. S. Withers J. B. Green	Lincoln Laboratory Technical Seminar Series, Massachusetts Institute of Technology, Cambridge, Massachusetts, 24 January 1991

ORGANIZATION

SOLID STATE DIVISION

A. L. McWhorter, *Head*
I. Melngailis, *Associate Head*
E. Stern, *Associate Head*
J. F. Goodwin, *Assistant*

D. J. Ehrlich, *Senior Staff*
N. L. DeMeo, Jr., *Associate Staff*
J. W. Caunt, *Assistant Staff*
K. J. Challberg, *Administrative Staff*

SUBMICROMETER TECHNOLOGY

D. C. Shaver, *Leader*
M. Rothschild, *Assistant Leader*

Astolfi, D. K.	Hartney, M. A.
Craig, D. M.	Horn, M. W.
Dennis, C. L.	Kunz, R. R.
Doran, S. P.	Lyszczarz, T. M.
Efremow, N. N., Jr.	Maki, P. A.
Forte, A. R.	Melngailis, J. [†]
Gajar, S. A.*	Paladugu, R. R.
Geis, M. W.	Sedlacek, J. H. C.
Goodman, R. B.	Uttaro, R. S.

QUANTUM ELECTRONICS

A. Mooradian, *Leader*
P. L. Kelley, *Associate Leader*
A. Sanchez-Rubio, *Assistant Leader*

Aggarwal, R. L.	Jeys, T. H.
Barch, W. E.	Korn, J. A.
Cook, C. C.	Lacovara, P.
Daneu, V.	Le, H. Q.
DeFeo, W. E.	Menyuk, N. [†]
DiCecca, S.	Nabors, C. D.
Dill, C. D., III	Ochoa, J. R.
Fan, T. Y.	Schulz, P. A.
Hancock, R. C.	Seemungal, W. A.
Henion, S. R.	Sullivan, D. J.
Hotaling, T. C.	Wall, K. F.
Hsu, L.*	Zayhowski, J. J.

ELECTRONIC MATERIALS

A. J. Strauss, *Leader*
B-Y. Tsaur, *Associate Leader*

Anderson, C. H., Jr.	Iseler, G. W.
Button, M. J.	Kolesar, D. F.
Chen, C. K.	Krohn, L., Jr.
Choi, H. K.	Marino, S. A.
Clark, H. R., Jr.	Mastromattei, E. L.
Connors, M. K.	McGilvary, W. L.
Delaney, E. J.	Nitishin, P. M.
Eglash, S. J.	Pantano, J. V.
Fahey, R. E.	Turner, G. W.
Finn, M. C.	Wang, C. A.

HIGH SPEED ELECTRONICS

R.A. Murphy, *Leader*
M. A. Hollis, *Assistant Leader*
R. W. Chick, *Senior Staff*

Actis, R.	Mahoney, L. J.
Bales, J. W.*	Manfra, M. J.
Barlas, A. D.	Mathews, R. H.
Bergeron, N. J.	Mattia, J. P.*
Bozler, C. O.	McIntosh, K. A.
Brown, E. R.	McMorran, R. A.
Calawa, A. R.	McNamara, M. J.
Chen, C. L.	Nichols, K. B.
Clifton, B. J.	Parker, C. D.
Crenshaw, D. L.*	Rabe, S.
Gladden, D. B. [‡]	Rathman, D. D.
Goodhue, W. D.	Smith, F. W., III
Gray, R. V.	Vera, A.
Lincoln, G. A., Jr.	

* Research Assistant

[†] Part Time

[‡] Leave of Absence

ELECTROOPTICAL DEVICES

R. C. Williamson, *Leader*
D. L. Spears, *Assistant Leader*
R. H. Rediker, *Senior Staff*

Aull, B. F. [‡]	Missaggia, L. J.
Bailey, R. J.	Mull, D. E.
Barwick, D. S.*	O'Donnell, F. J.
Betts, G. E.	Palmacci, S. T.
Corcoran, C. J.*	Palmateer, S. C.
Cox, C. H., III	Pheiffer, B. K.*
Diadiuk, V.	Rauschenbach, K.
Donnelly, J. P.	Reeder, R. E.
Ferrante, G. A.	Roussell, H. V.
Groves, S. H.	Shiple, S. D.*
Harman, T. C.	Tsang, D. Z.
Hovey, D. L.	Walpole, J. N.
Johnson, L. M.	Woodhouse, J. D.
Liau, Z. L.	Yee, A. C.
Lind, T. A.	

ANALOG DEVICE TECHNOLOGY

R. W. Ralston, *Leader*
R. S. Withers, *Associate Leader*
T. C. L. G. Sollner, *Assistant Leader*
A. C. Anderson, *Senior Staff*
R. M. Lerner, *Senior Staff*

Arsenault, D. R.	Lyons, W. G.
Bhushan, M.	Macedo, E. M., Jr.
Boisvert, R. R.	Minnick, R. G.
Brogan, W. T.	Oates, D. E.
Denneno, A. P.	Sage, J. P.
Fitch, G. L.	Seaver, M. M.
Green, J. B.	Slattery, R. L.
Hamm, J. M.	Westerheim, A. C.*
Holtham, J. H.	Whitley, D. B.
Lattes, A. L.	Yu-Jahnes, L. S.*

MICROELECTRONICS

E. D. Savoye, *Leader*
B. B. Kosicki, *Assistant Leader*
B. E. Burke, *Senior Staff*
A. M. Chiang, *Senior Staff*

Chuang, M. L.*	Felton, B. J.	Loomis, A. H.
Collins, I. K.	Gregory, J. A.	McGonagle, W. H.
Cooper, M. J.	Huang, C. M.	Mountain, R. W.
Daniels, P. J.	Hurley, E. T.	Percival, K. A.
Doherty, C. L., Jr.	Johnson, B. W.	Pichler, H. H.
Dolat, V. S.	Johnson, K. F.	Reich, R. K.
Donahue, T. C.	LaFranchise, J. R.	Reinold, J. H., Jr.
Durant, G. L.		Young, D. J.

* Research Assistant

† Part Time

‡ Leave of Absence

1. ELECTROOPTICAL DEVICES

1.1 BURIED-HETEROSTRUCTURE InGaAs /GaAs /GaInP STRAINED-LAYER QUANTUM-WELL LASERS ($\lambda = 980$ nm) FABRICATED BY MASS TRANSPORT

GaAs-based diode lasers with alloys of GaInAsP replacing those of AlGaAs appear to have superior resistance to degradation [1],[2] and can be readily fabricated by epitaxial regrowth and/or mass transport [3]. Here, we demonstrate the first fabrication of buried-heterostructure (BH) quantum-well lasers by mass transport. This result has been achieved by using a separate-confinement heterostructure with cladding layers of $\text{Ga}_{0.51}\text{In}_{0.49}\text{P}$ (hereafter abbreviated as GaInP). As shown in [3], this alloy, which is lattice matched to GaAs, can be mass transported without change in alloy composition. The active layer of the laser is a single strained-layer quantum well of $\text{In}_{0.18}\text{Ga}_{0.82}\text{As}$, and the confining layers are formed of GaAs. Ridge-guide lasers emitting at wavelengths slightly longer than $1\ \mu\text{m}$ and having excellent performance have been made from a similar structure [2]. Our devices emit at $\lambda = 980$ nm, which is the wavelength for most efficient pumping of Er-doped fiber amplifiers [4].

The scanning electron micrograph (SEM) in Figure 1-1 shows a transverse cross section of the BH device. The structure has been grown at 650°C by atmospheric-pressure organometallic vapor phase epitaxy (OMVPE) on a Si-doped GaAs substrate ($n \approx 1 \times 10^{18}\ \text{cm}^{-3}$) oriented 5° off (001) toward [110]. Growth of GaInP can show surface roughness when viewed by differential interference microscopy, but with substrates of this direction and degree of off-orientation the growth is smooth. Details of the growth apparatus have been given elsewhere [3],[5]. In order of growth, the layers of the structure are a $0.2\text{-}\mu\text{m}$ -thick n -GaAs buffer layer, a $1.2\text{-}\mu\text{m}$ -thick n -GaInP cladding layer, a $900\text{-}\text{\AA}$ -thick undoped GaAs confining layer, an $80\text{-}\text{\AA}$ -thick undoped $\text{In}_{0.18}\text{Ga}_{0.82}\text{As}$ strained-layer quantum well, a $900\text{-}\text{\AA}$ -thick undoped GaAs confining layer, a $1.2\text{-}\mu\text{m}$ -thick p -GaInP cladding layer, a $0.2\text{-}\mu\text{m}$ -thick p^+ -GaAs contact layer, and a $0.15\text{-}\mu\text{m}$ -thick p^+ -GaInP cap layer. Silicon and zinc have been used as n - and p -type dopants, respectively, and the doped layers have carrier concentrations of $\sim 2 \times 10^{18}\ \text{cm}^{-3}$, with the p^+ layers doped about an order of magnitude higher. An undoped region of GaInP, $600\ \text{\AA}$ thick, was grown before starting the p -type doping in the upper cladding layer. The purpose of the cap layer, mentioned above but not shown in Figure 1-1, is to permit cooling under a phosphine, rather than arsine, flow and thus minimize the compensation of zinc by atomic hydrogen. This layer is removed by a selective etch prior to device fabrication.

Figure 1-2 shows the broad-area threshold current density J_{th} vs inverse cavity length for these devices. A $225\text{-}\mu\text{m}$ -wide stripe has been defined by etched isolation grooves, and devices have been cleaved to various cavity lengths. Wang and Choi [6], using strained-layer single-quantum-well lasers with $\text{Al}_{0.7}\text{Ga}_{0.3}\text{As}$ cladding, have reported the lowest J_{th} values for InGaAs strained-layer lasers. A line representing their data is included in Figure 1-2, showing that our results are only slightly above these lowest values.

A procedure for making BH lasers with GaInP/GaAs double heterostructures was described in [3]. Improvements in performance of double-heterostructure devices as well as a simplified BH fabrication technique have been reported more recently [7],[8]. A similar fabrication process has been used here to produce the BH quantum-well devices. Deposited and patterned stripes of SiO_2 on the GaAs contact layer serve as a mask for chemical etching of the structure. This SiO_2 is left as a cover over the GaAs to avoid

complications with the GaInP mass transport, which is carried out in a phosphorus overpressure at 725°C for ~ 1 h. The transported GaInP provides good sidewall passivation and waveguiding to the 1- μm -lateral-width active region. It also provides good current confinement because of its wide bandgap and narrow width. This structure is well suited for high-speed modulation.

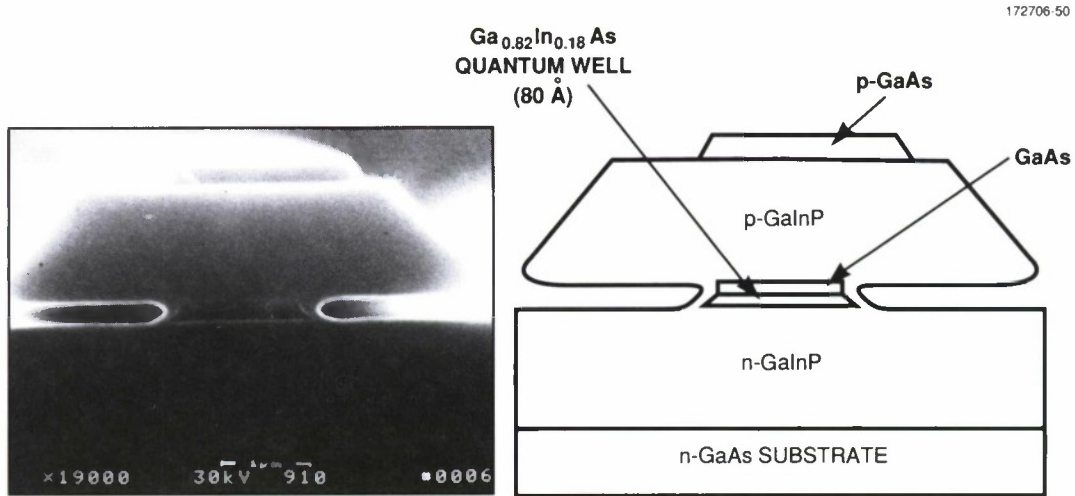


Figure 1-1. SEM of a cleaved and stained transverse cross section of the buried heterostructure. A drawing of this view is provided as an aid to understanding the micrograph.

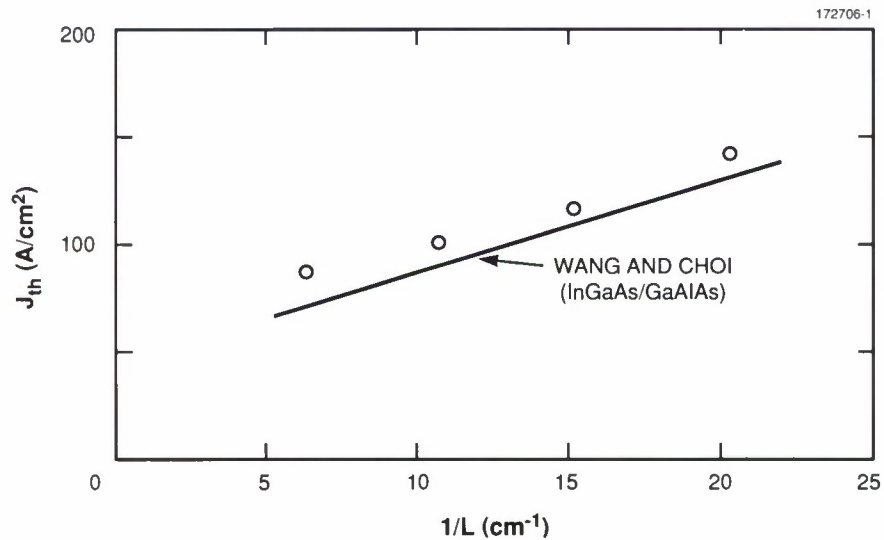


Figure 1-2. Threshold current density vs inverse cavity length for broad-area (225 μm wide) devices. Comparison is made with the lowest reported threshold current densities [6] (solid line).

Pulsed output power vs drive current for a BH device is shown in Figure 1-3. The threshold current is about 3 mA, and the device can be driven to ~ 35 times this level. At 30 mW per facet output, the power densities are 30 mW per micrometer width or ~ 15 MW per square centimeter of separate-confinement heterostructure area. We are unaware of any published values that are this high for uncoated facets. For CW operation there was only a 0.5-mA increase in threshold current, and output powers in excess of 10 mW per facet were measured.

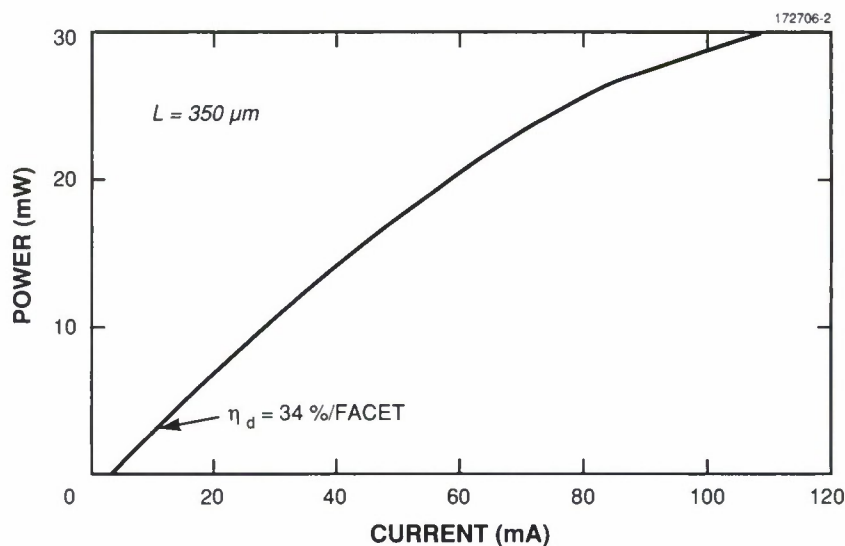


Figure 1-3. Power per facet vs current for buried-heterostructure devices in pulsed operation, showing operation to ~ 35 times threshold current and facet power densities of ~ 15 MW/cm².

Two observations have been made regarding the resistance to degradation of GaInAsP/GaAs structures. Repeated cycling over the full power range shown in Figure 1-3 produced no change, an observation that is consistent with [2] and that indicates a high resistance to catastrophic mirror damage. In CW operation there was a 10% increase in threshold during the first 50 h of operation and then very little change for the next 700 h that the device was tested. This is consistent with the observations of [1] and suggests that these alloys have good resistance to rapid degradation by dark-line-defect propagation.

S. H. Groves	S. C. Palmateer
Z. L. Liao	J. N. Walpole
L. J. Missaggia	

1.2 ANALYSIS OF VAPOR DIFFUSION IN SURFACE-ENERGY-INDUCED MASS TRANSPORT

Mass transport in compound semiconductor surfaces is of considerable interest for epitaxial crystal growth as well as for device-structure formation. Diffusions both along the surface [9],[10] and through the vapor phase [10]-[12] have been discussed as possible transport mechanisms. A comprehensive model has recently been developed for surface diffusion and has yielded considerable insight [13]. Here, a similar model is presented for the vapor-phase diffusion.

Consider an InP wafer with a (spatially) slowly varying sinusoidal surface profile

$$f(x,t) = A(t) \sin \frac{2\pi x}{\Lambda} , \quad (1.1)$$

as illustrated in Figure 1-4. This simple profile can also represent a Fourier component of a more general profile. At an elevated temperature, some dissociation and vaporization occur near the surface. The equilibrium In vapor concentration depends on the high phosphorus vapor concentration supplied in the system. To prevent excess evaporation loss, a cover is applied [14], whose separation s from the substrate is approximated as constant because of the small amplitude of the surface profile. We further assume no vapor permeation through or adsorption on the cover.

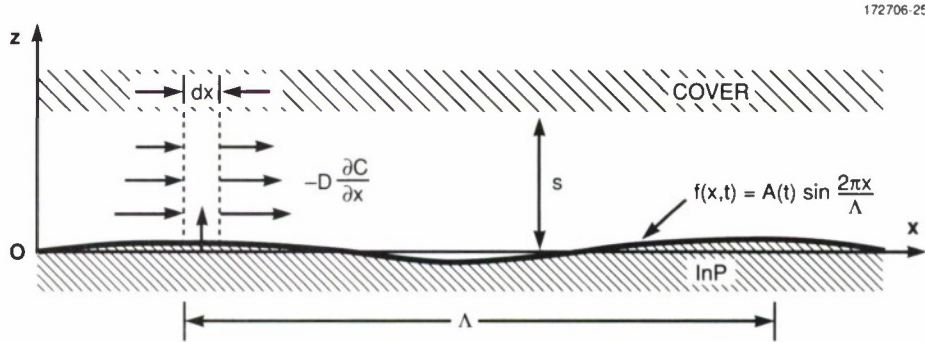


Figure 1-4. Illustration of the present model of surface-energy-induced mass transport via vapor diffusion.

Since the degree of dissociation depends on surface energy, a variation of the vapor concentration occurs that corresponds with the variation of the surface profile curvature. In the parameter ranges of interest it can be shown that quasi-equilibrium exists, and the In vapor concentration along the surface is given simply by [13]

$$C(x,t) \approx C_0 \left(1 + \frac{\epsilon}{kT} \right) , \quad (1.2)$$

where C_0 is the equilibrium vapor concentration of a flat surface and ε is the surface energy due to the curvature. For a slowly varying surface profile,

$$\begin{aligned}\varepsilon &= -\alpha v \frac{\partial^2 f}{\partial x^2} \\ &= \frac{(2\pi)^2 \alpha v A}{\Lambda^2} \sin \frac{2\pi x}{\Lambda} ,\end{aligned}\tag{1.3}$$

where α and v are, respectively, the coefficient of surface tension and the molecular volume [13].

The diffusion of the In vapor in the space between the wafer and the cover is governed by the continuity equation

$$D \left(\frac{\partial^2 C}{\partial x^2} + \frac{\partial^2 C}{\partial z^2} \right) = \frac{\partial C}{\partial t} ,\tag{1.4}$$

where D is the diffusivity. However, it can be shown that $\partial C / \partial t$ can be neglected. The simplified equation can then be solved by separation of variables, and the solution satisfying the boundary conditions is

$$C(x, z, t) = C_0 \left[1 + \frac{(2\pi)^2 \alpha v A(t)}{kT\Lambda^2} \left(\sin \frac{2\pi x}{\Lambda} \right) \frac{\cosh \frac{s-z}{L}}{\cosh \frac{s}{L}} \right] ,\tag{1.5}$$

with

$$-\left(\frac{2\pi}{\Lambda} \right)^2 + \left(\frac{1}{L} \right)^2 = 0 ,\tag{1.6a}$$

or

$$L = \frac{\Lambda}{2\pi} .\tag{1.6b}$$

Next, consider the In vapor diffusion across a volume element bounded by x and $x + dx$, as illustrated in Figure 1-4. The net outdiffusion in the x -direction can be evaluated by integrating Equation (1.4) along the z -direction and by noting that $\partial C / \partial t = 0$ in that equation, and thus

$$-dx \int_0^s D \frac{\partial^2 C}{\partial x^2} dz = D \frac{\partial C}{\partial z} \Big|_{z=0}^{z=s} dx .\tag{1.7a}$$

Since , $(\partial C/\partial t)|_{z=s} = 0$ as assumed in the present model, the right-hand side of Equation (1.7a) is simply the rate of indiffusion across $z = 0$, which must equal the evaporation rate there. Hence,

$$-\frac{1}{v} \frac{\partial f}{\partial t} = - \int_0^s D \frac{\partial^2 C}{\partial x^2} dz . \quad (1.7b)$$

By substituting for f and C , as given by Equations (1.1) and (1.5), respectively, and after some rearranging, Equation (1.7b) becomes

$$\frac{1}{v} \frac{dA}{dt} = - \frac{(2\pi)^3 \alpha v C_0 D}{kT\Lambda^3} \left(\tanh \frac{2\pi s}{\Lambda} \right) A . \quad (1.8)$$

This equation can then be solved to yield the time evolution of the profile amplitude,

$$A(t) = A(0) e^{-t/\tau} , \quad (1.9)$$

with

$$\frac{1}{\tau} \equiv \frac{(2\pi)^3 \alpha v^2 C_0 D}{kT\Lambda^3} \tanh \frac{2\pi s}{\Lambda} . \quad (1.10)$$

In the case of $s \ll \Lambda/2\pi$, Equation (1.10) simplifies to

$$\frac{1}{\tau} \approx \frac{(2\pi)^4 \alpha v^2 C_0 D s}{kT\Lambda^4} . \quad (1.11)$$

Note that this decay rate shows the same Λ^{-4} dependence as that of the previously considered surface diffusion [13]. However, there is an additional dependence on s , which can be interpreted as the width of the diffusion channel. In the other extreme case, $s \gg \Lambda/2\pi$, Equation (1.10) becomes

$$\frac{1}{\tau} \approx \frac{(2\pi)^3 \alpha v^2 C_0 D}{kT\Lambda^3} , \quad (1.12)$$

in which the s -dependence drops out and the Λ -dependence becomes cubic. This shows that the maximum diffusion channel is limited to $\Lambda/2\pi$.

In conclusion, a simple analytical model has been developed for surface-energy-induced mass transport through vapor diffusion. The predicted s -dependence can be used to experimentally distinguish the vapor process from the surface one. It can also be used to maximize the mass-transport rate. However, an accurate control of s may present a considerable practical challenge. Also, one should guard against possible deviations from the ideal cover assumed here, which does not allow for vapor permeation or adsorption.

Z. L. Liao

REFERENCES

1. D. Z. Garbuzov, N. Y. Antonishkis, A. D. Bondarev, S. N. Zhigulin, A. V. Kochergin, N. I. Katsavets, and E. U. Rafailov, presented at 12th Int. Semiconductor Laser Conference, Davos, Switzerland, 9-14 Sept. 1990, Paper L-33.
2. T. Ijichi, M. Ohkubo, N. Matsumoto, and H. Okamoto, *ibid.*, Paper D-2.
3. S. H. Groves, Z. L. Liao, S. C. Palmateer, and J. N. Walpole, *Appl. Phys. Lett.* **56**, 312 (1990).
4. See, for example, Y. Kimura, M. Nakazawa, and K. Suzuki, *Appl. Phys. Lett.* **57**, 2635 (1990).
5. S. C. Palmateer, S. H. Groves, J. W. Caunt, and D. L. Hovey, *J. Electron. Mater.* **18**, 645 (1989).
6. C. A. Wang and H. K. Choi, to be published in *IEEE J. Quantum Electron.*, March 1991.
7. J. N. Walpole, S. H. Groves, Z. L. Liao, S. C. Palmateer, and D. Z. Tsang, presented at 12th Int. Semiconductor Laser Conference, Davos, Switzerland, 9-14 Sept. 1990, Paper J-5.
8. Solid State Research Report, Lincoln Laboratory, MIT, 1990:2, p. 4.
9. H. Nagai, Y. Noguchi, and T. Matsuoka, *J. Cryst. Growth* **71**, 225 (1985).
10. E. Colas, E. M. Clausen, Jr., E. Kapon, D. M. Hwang, and S. Simhony, *Appl. Phys. Lett.* **57**, 2472 (1990).
11. M. Ayabe, H. Nagasawa, and K. Kaneko, *J. Cryst. Growth* **58**, 180 (1982).
12. T. R. Chen, L. C. Chiu, A. Hasson, K. L. Yu, U. Koren, S. Margalit, and A. Yariv, *J. Appl. Phys.* **54**, 2407 (1983).
13. Z. L. Liao and H. J. Zeiger, *J. Appl. Phys.* **67**, 2434 (1990).
14. Solid State Research Report, Lincoln Laboratory, MIT, 1990:3, p. 1.

2. QUANTUM ELECTRONICS

2.1 5-GHz MODE LOCKING OF A Nd:YLF LASER WITH 10-ps PULSES

Interest in sampling at rates above 1 GHz and in accurate clocking for optical communication systems has fostered the development of high-repetition-rate solid state lasers. Electrooptic, acoustooptic, and passive mode-locking techniques all are capable of generating high repetition rates. Acoustooptic mode locking has been studied recently because of the realization that good diffraction efficiency at high acoustic frequencies can be achieved using Al_2O_3 [1] or GaP [2] as the acoustic material. Weingarten and coworkers [1] obtained a repetition rate of 2 GHz with a mode-locked Nd:YLF laser. Even by using the best acoustooptic materials, however, the loss modulation of acoustooptic devices becomes inadequate for mode locking at frequencies much higher than 2 GHz. In principle, passive mode-locking techniques are capable of generating still higher repetition rates, but in practice it is difficult to incorporate the required optical elements, for example, a dispersion compensator or a saturable absorber, in the necessarily short cavity. On the other hand, electrooptic modulation with good sensitivity can be achieved in the microwave region [3]. We have realized frequency-modulated mode locking with a LiTaO_3 modulator in a Nd:YLF laser at 5.37 GHz, which is the highest mode-locking frequency obtained to date.

The Nd:YLF laser cavity, illustrated in Figure 2-1, contains the Nd:YLF crystal, the LiTaO_3 modulator, a pump-side mirror having high reflectivity at the laser wavelength, and an output coupler. A $\text{Ti:Al}_2\text{O}_3$ laser operating at 790 nm provides 500 mW of pump light, 85% of which is transmitted by the pump-side mirror. The laser generates 60 mW of output at $1.053 \mu\text{m}$ under both mode-locked and free-running conditions. The Nd:YLF crystal, which is 3 mm thick with both sides antireflection coated, is tilted 10° , because even small on-axis reflections can destroy mode locking [4]. The Brewster-angle LiTaO_3 crystal is 1 mm (X) by 4 mm (Y) by 1.5 mm (Z), where X, Y, and Z refer to crystallographic axes. The applied and laser polarizations are in the Z direction to take advantage of the large electrooptic coefficient of LiTaO_3 for this case.

To take advantage of the limited amount of microwave voltage available, the coupling of the source voltage across the LiTaO_3 crystal must be efficient, which requires the input, output, and transmission line impedances to be equal. Since the output impedance of the microwave source and the transmission line impedance of the cable are 50Ω , the input impedance into the phase modulator should also be 50Ω . Measurements of the input impedance as a function of applied frequency show that at 5.4 GHz the impedance is $12 - i21 \Omega$. The length of the laser cavity was selected so that the mode-locked repetition rate was at this frequency. The optical path length change of the laser cavity is only 1 nm for 100 mW of microwave power, as measured by placing the modulator in one arm of a Mach-Zehnder interferometer.

The output pulse duration was measured with a collinear autocorrelator. Figure 2-2 shows the autocorrelation measurement for 80 mW of microwave power, which reveals pulses with ~ 10 -ps duration, assuming a Gaussian temporal pulse shape. The theory of forced mode locking predicts that sufficiently above threshold the pulse duration $t \sim P^{-1/4}$, where P is the applied microwave power [5]. When only 20 mW of microwave power was applied, the pulse duration increased to 15 ps, as expected.

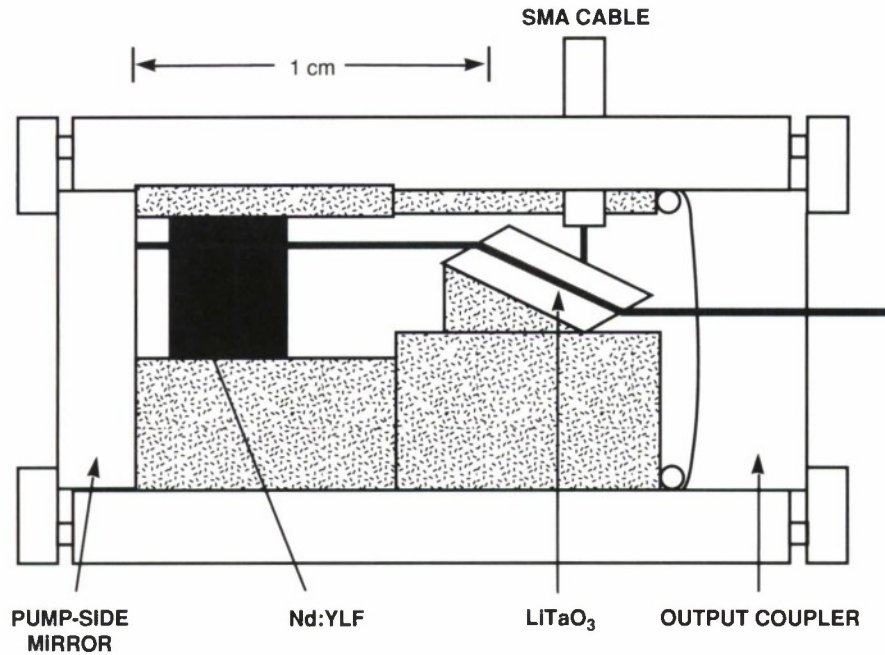


Figure 2-1. Schematic of the mode-locked Nd:YLF laser. The distance between the mirrors is 1.6 cm, and the output coupler has a 5-cm radius of curvature and 2% transmission at $1.053 \mu\text{m}$. The Y axis of the LiTaO_3 is along the laser optical axis, and the Nd:YLF crystal is 3 mm long.

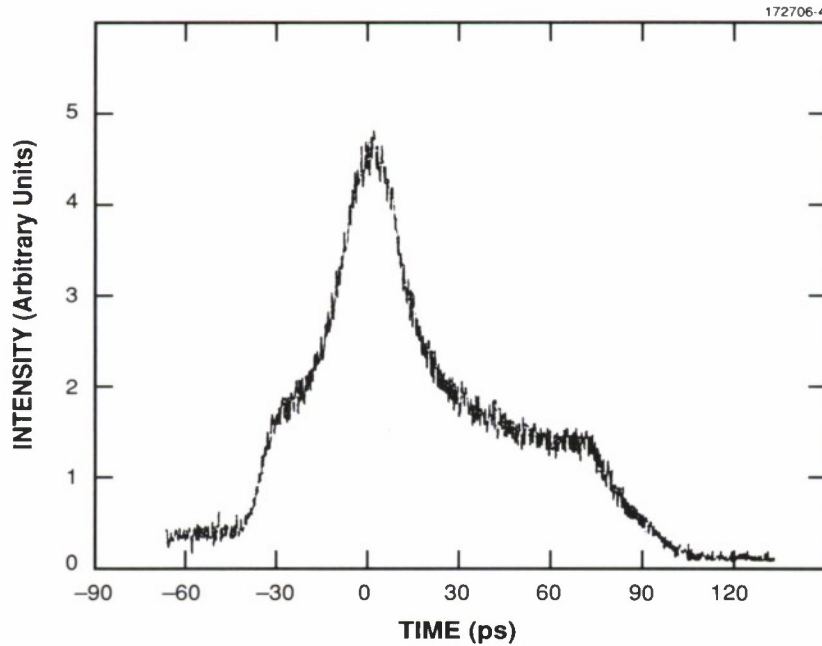


Figure 2-2. Autocorrelation of the mode-locked Nd:YLF laser output. For this measurement, a beamsplitting mirror in the autocorrelator splits the incoming beam into two, both beams pass twice through a rotating prism, and the beams are recombined on the beamsplitter and frequency doubled in MgO-doped LiNbO_3 .

In frequency-modulated mode locking the laser pulses can occur for either of two different phases in the cavity, passing through the phase modulator at either the path length minimum or the path length maximum. It has been noted, however, that under some circumstances the phase selection is stable [6]. In our laser no hopping between the two alternative phase states was observed over 30 min. This observation was made by triggering a sampling oscilloscope with the applied microwave signal, so a 180° phase change would cause a 93-ps shift in the location of the pulse. Even turning the microwave source off and back on did not result in phase-state hopping, but tuning the microwave frequency did cause hopping.

Spectra of the laser output for free-running and mode-locked operation are shown in Figure 2-3. The spectral envelope did not increase significantly upon mode locking, but the spectral stability and the presence

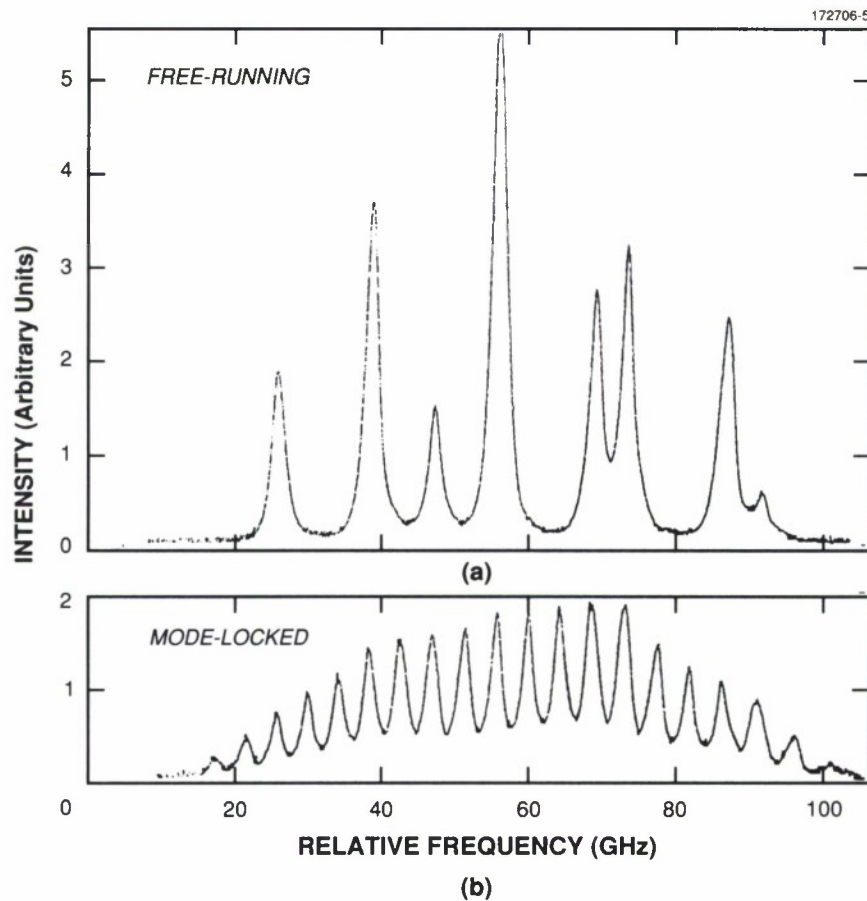


Figure 2-3. Fabry-Perot spectra of the Nd:YLF laser. (a) Under free-running conditions a number of modes are observed; spatial hole burning in the Nd:YLF allows simultaneous operation of these modes. (b) Under mode-locked conditions all of the modes within the bandwidth observed under free-running conditions lase; these modes are separated by 5.37 GHz.

of a smooth spectral envelope are properties of mode-locked operation. The fairly large spectral width under free-running conditions is a result of spatial hole burning. For mode-locked conditions, approximately ten modes lie within the spatial bandwidth. The product of the pulse duration and spectral bandwidth of 0.75 for a microwave power of 20 mW is close to the theoretical limit for frequency-modulated mode locking (0.63).

S. R. Henion
P. A. Schulz

2.2 THEORETICAL ANALYSIS OF THE Q-SWITCHED MICROCHIP LASER

Recently, we reported the generation of 6-ns Q-switched pulses from a microchip laser [7]. In order to understand our experimental results and as an aid in optimizing the performance of future Q-switched microchip lasers, it is useful to do theoretical modeling of the device. Most of the results obtained in this section are from a standard rate-equation analysis [8]. Two new results include explicit expressions for the minimum output pulse width and maximum output power obtainable for a given population inversion. These expressions are applicable to all Q-switched lasers (within the approximations stated below) and should help the laser designer optimize the performance of a Q-switched device.

To model the Q-switched operation of the microchip laser, we assume uniform CW pumping of the gain medium, use a plane-wave approximation for the transverse mode profile, and model the intracavity optical intensity as axially uniform. Since the Q-switched output pulses from the laser are much shorter than both the spontaneous lifetime and the pump period (time between output pulses), spontaneous relaxation and pumping can be safely neglected during the development of the output pulse. We further assume that at time $t = 0$ the Q of the laser cavity is rapidly switched such that for $t = 0^-$ the inversion density within the cavity is below its threshold value and for $t = 0^+$ it is Y_{0+} times the threshold inversion density. With these assumptions, the development of the output pulse in a four-level laser can be modeled by the equations [8]

$$dX/dT = (Y - 1)X \quad (2.1a)$$

and

$$dY/dT = -XY, \quad (2.1b)$$

where

$$X \equiv 2In/chvN_t \quad (2.2a)$$

is the normalized intracavity optical intensity,

$$Y \equiv N/N_t \quad (2.2b)$$

is the normalized inversion density, and

$$T \equiv t/\tau_c \quad (2.2c)$$

is normalized time. In the above equations, I is the circulating intracavity optical intensity, N is the population inversion density, $N_t = \gamma/2\sigma\ell$ is the threshold population inversion density for $t > 0$, $\tau_c = 2n\ell/\gamma$ is the cavity lifetime, ℓ is the cavity length, $\gamma \approx \gamma_p + \gamma_o$ is the total round-trip cavity loss, γ_p is the round-trip parasitic loss, γ_o is the output coupling, σ is the emission cross section at the lasing wavelength ($3 \times 10^{-19} \text{ cm}^2$ for the

1.064- μm transition in Nd:YAG), ν is the lasing frequency, n is the refractive index (1.82 for Nd:YAG), c is the speed of light in vacuum, and h is Planck's constant. Equations (2.1a) and (2.1b) can be solved numerically for the pulse shape if we assume a small initial value of X_0 at $t = 0$. The calculated normalized intensity vs time for several values of Y_{0+} is shown in Figure 2-4. From the pulse shape we can derive universal curves for the normalized peak pulse intensity X_p and the normalized pulse full width at half-maximum (FWHM), T_w , as shown in Figures 2-5 and 2-6. (Note that X_p can be obtained as an analytic function of Y_{0+} [10].) These two curves are independent of the initial value of X_0 , as long as it is much smaller than the peak value.

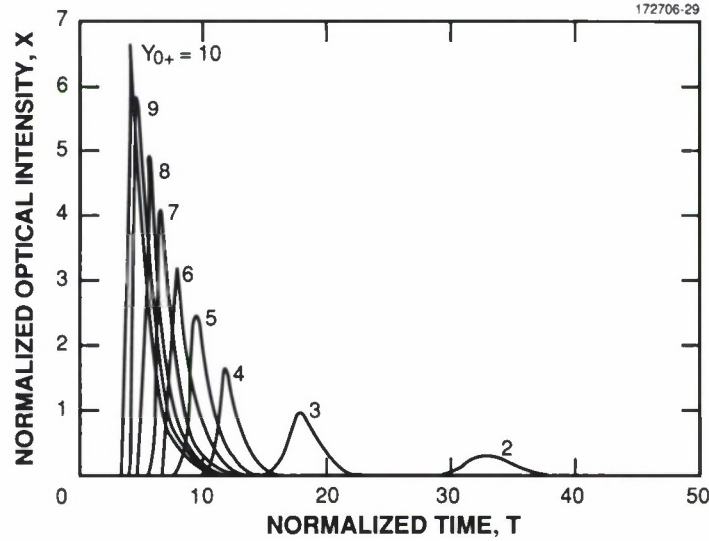


Figure 2-4. Normalized optical intensity X of a Q-switched pulse obtained for a normalized inversion density Y_{0+} of 2, 3, 4, 5, 6, 7, 8, 9, and 10 as a function of normalized time T , calculated for $X_0 = 10^{-14}$.

An expression for the FWHM of the pulse, t_w , can be obtained by combining (2.2b) and (2.2c) to yield

$$t_w = T_w Y_{0+} n / N_0 c \sigma, \quad (2.3)$$

where N_0 is the inversion density at $t = 0$. The product $T_w Y_{0+}$ has a minimum value of 8.1 at $Y_{0+} = 3.1$, $T_w = 2.6$. The minimum pulse width obtainable for a given inversion density is, therefore,

$$t_{w,\min} = 8.1 n / N_0 c \sigma \quad (2.4)$$

and is obtained when the cavity is designed so that just after Q-switching ($t = 0+$) the cavity lifetime is $3.1 n / N_0 c \sigma$. It can be seen from Figure 2-7 that the pulse width is relatively insensitive to the new cavity lifetime, staying within 50% of the minimum value for $1.5 < \tau_c N_0 c \sigma / n < 10$.

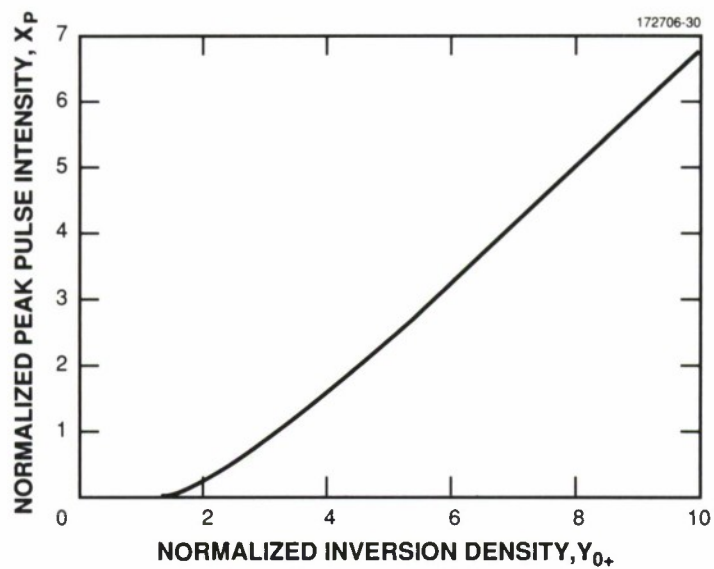


Figure 2-5. Normalized peak pulse intensity X_p as a function of normalized inversion density Y_{0+} .

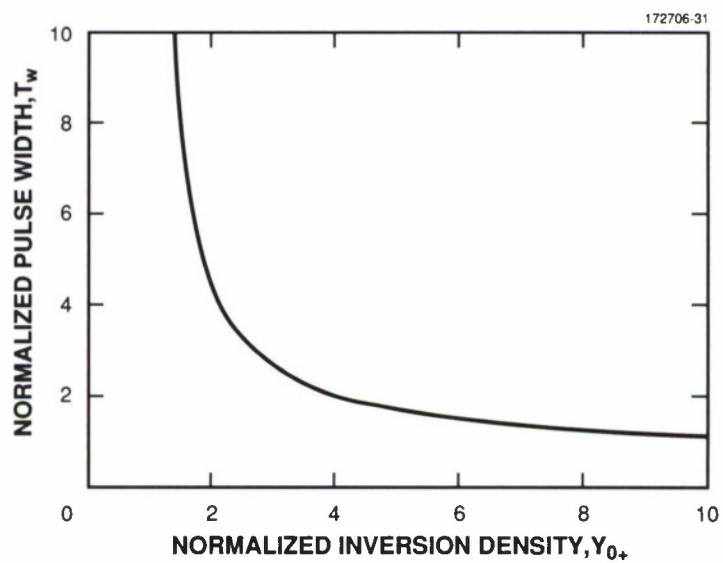


Figure 2-6. Normalized pulse width T_w (FWHM) as a function of normalized inversion density Y_{0+} .

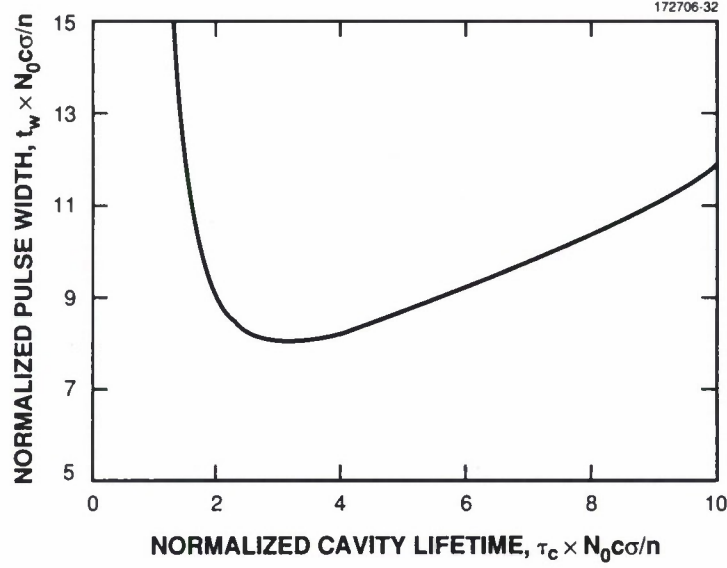


Figure 2-7. Pulse width t_w as a function of the cavity lifetime τ_c after Q-switching.

The peak output intensity I_{po} is given by

$$I_{po} = \frac{X_p}{Y_{0+}^2} \left(1 - \frac{Y_{0+} \gamma_p}{2N_0 \sigma \ell} \right) \frac{N_0^2 c \sigma \ell h \nu}{n} . \quad (2.5)$$

For negligible parasitic loss ($\gamma_p \ll \gamma_o$), the maximum value of I_{po} occurs at $Y_{0+} = 3.5$, $X = 1.3$. (At $Y_{0+} = 3.1$, corresponding to the minimum pulse width, the value of X_p/Y_{0+}^2 is 0.101.) In this case, the maximum peak pulse intensity for a given inversion density is

$$I_{po, \max} = 0.102 N_0^2 c \sigma \ell h \nu / n \quad (2.6)$$

and is obtained when the cavity is designed so that just after Q-switching the cavity lifetime is $3.5n / N_0 c \sigma$. It can be seen from Figure 2-8 that the peak pulse intensity is also relatively insensitive to the new cavity lifetime. It is interesting to note that except for a 20% decrease in the numerical constant, Equation (2.6) is the same as the result that would be obtained if one assumed a top-hat-shaped pulse with a pulse width given by Equation (2.4). When parasitic loss cannot be ignored, the peak intensity and the optimal value of the new cavity lifetime are reduced.

The pulse buildup time t_b cannot be calculated in the same way as the pulse width or peak intensity, since it is dependent on the initial value of the intracavity optical intensity. However, since the optical intensity is small during most of the buildup time, the inversion density can be approximated as constant during the pulse

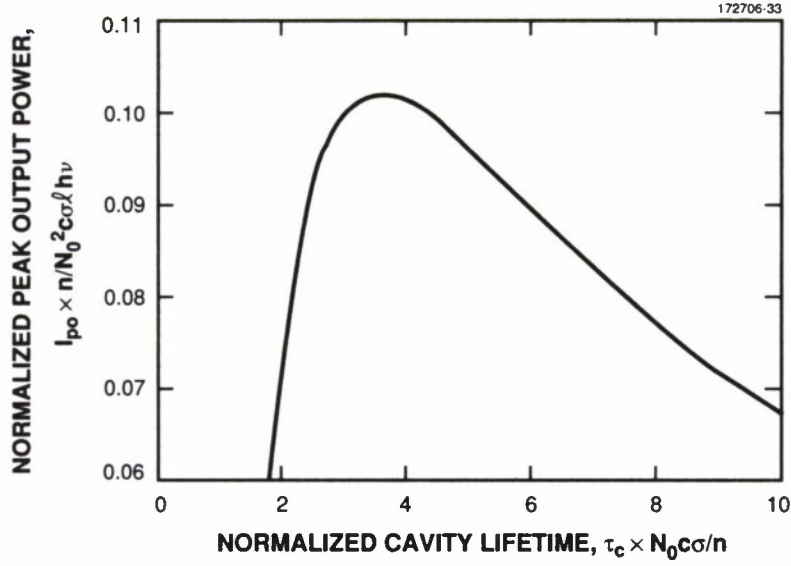


Figure 2-8. Peak output intensity I_{po} as a function of the cavity lifetime τ_c after Q-switching for negligible parasitic loss.

development. This allows us to solve Equation (2.1a) analytically to obtain an approximate expression for the normalized pulse buildup time:

$$T_b \approx \frac{\ln(X_p/X_0)}{Y_{0+} - 1} . \quad (2.7)$$

For a laser cavity that is sufficiently lossy between output pulses, the pulse must build up from spontaneous emission, giving

$$X_0 = (2\pi r_m^2 \ell N_t)^{-1} , \quad (2.8)$$

where r_m is the radius of the lasing mode. The pulse buildup time for a minimum-width pulse is thus given by

$$t_{b,\min} \approx 0.48 \ln(0.63 N_0 \pi r_m^2 \ell) \tau_c . \quad (2.9)$$

In practice, the way the Q of a laser cavity is switched is by changing the cavity loss. This often requires the switching of high voltages and is difficult to do very rapidly. As a result, the instantaneous Q-switching approximation is often not valid. Fortunately, the width of the Q-switched output pulse is determined by the cavity Q at the time of the output pulse (within t_w of its peak) and is insensitive to the details of the way in which it is switched. The pulse buildup time, on the other hand, is strongly dependent on how the Q is switched. Depending on the value of the cavity Q before and after switching, and the way in which the Q is switched,

the allowed switching time for a given output pulse width may be considerably longer than Equation (2.9) indicates. As an example, if the value of the cavity loss changes linearly with time between an initial value corresponding to $Y_{0+} = 1$ and a value corresponding to $Y_p = 3.1$ just before the peak of the output pulse, then as Equation (2.1a) shows, the pulse buildup time can be increased by a factor of 3.3:

$$T_b \approx \frac{\ln(X_p/X_0)}{Y_p \ln(Y_p - 1) - 1} . \quad (2.10)$$

If a pulse width of 1.5 times the minimum value is acceptable (corresponding to $Y_p = 1.5$), we can gain an additional factor of ~ 4 in the pulse buildup time of Equation (2.8), or ~ 3.2 in the buildup time of Equation (2.10). The switching time is further increased if the initial value of Y_{0+} is < 1 . Also, the change in cavity Q can continue beyond the time when the output pulse is generated, as long as it is reversed early enough to prevent the generation of a second pulse.

The simple model presented here does a good job of explaining the behavior of the Q-switched microchip laser [7]. The calculated value of $t_{w,\min}$ for the experimental conditions reported (100 mW of CW pump power absorbed at 808 nm, 12.5 μs between Q-switched pulses, 650- μm -long cavity, 100- μm mode radius) is ~ 6 ns, in excellent agreement with the 6-ns pulse width obtained. The pulse buildup time calculated from Equation (2.9) for the experiment is 32 ns. The actual switching time was 6.25 μs . This illustrates the amount by which the actual switching time can be longer than the calculated buildup time of Equation (2.9) if the cavity Q is properly switched.

The formulas derived here provide a simple relationship between pump power, pulse repetition rate, output pulse width, peak output power, and cavity parameters that can be used in the design of Q-switched lasers. Using Equations (2.4) and (2.6), we can quickly calculate the minimum obtainable pulse width and maximum peak pulse intensity for a given pump power. The cavity can then be designed with the proper lifetime to obtain optimal performance. With a pump power of 1 W, a 10-kHz train of 100-ps pulses with peak powers > 100 kW is feasible from a Q-switched microchip laser.

J. J. Zayhowski

2.3 THEORETICAL ANALYSIS OF THE POLARIZATION-SWITCHABLE MICROCHIP LASER

Recently, we have demonstrated a way to quickly switch the polarization of microchip lasers [9]. Polarization switching is realized by increasing the Q of the cavity for one polarization mode while at the same time decreasing the Q for the orthogonally polarized mode. Since the two polarization modes correspond to the same axial mode, the oscillating mode completely depletes the gain for the orthogonal mode, such that spatial hole burning does not make it possible for the two modes to lase simultaneously.

To analyze the polarization-switching time of the microchip laser, we will assume that the two polarizations see the same cavity Q 's in their ON and OFF states and that the Q 's are switched instantaneously and simultaneously. We will assume that in the OFF state the Q of the cavity is reduced such that the inversion density is well below the threshold inversion density, allowing the oscillating mode to quickly decay. The

switching time is, therefore, determined by the buildup time of the new mode. For the polarization-switchable microchip laser the inversion density immediately after switching the Q of the cavity is equal to the CW threshold inversion density for the new mode (i.e., $Y_{0+} = 1$ in the notation of Section 2.2), since it was clamped at that value by the previous lasing mode. This is in strong contrast to the Q-switched microchip laser discussed in Section 2.2 and results in a much longer mode buildup time. The pumping of the laser during the mode buildup time can no longer be ignored, although we will still assume that spontaneous emission can be neglected. The new rate equations [8], again using the notation of Section 2.2, are

$$dX/dT = (Y - 1)X \quad (2.11a)$$

and

$$dY/dT = R - XY, \quad (2.11b)$$

where $R \equiv P_{\text{abs}} \tau_c / N_t h \nu_p \pi r_m^2 \ell$ is the normalized pump rate, P_{abs} is the pump power absorbed within the lasing mode volume, and ν_p is the pump frequency. To perform the calculation, we again make use of the fact that during most of the buildup time the intracavity optical intensity is small, so that the second term of Equation (2.11b) is unimportant. We will define the mode buildup time t_b as the time from the moment the cavity Q is switched until the time when the stimulated emission rate is equal to the pump rate, corresponding to $X \approx R$. With these approximations, the solution to Equation (2.11a) is

$$t_b^2 \approx 2 \ln(R/X_0) / R. \quad (2.12)$$

Since the new mode must start from spontaneous emission,

$$t_b^2 \approx \frac{2 h \nu_p n \pi r_m^2 \ell}{P_{\text{abs}} c \sigma} \ln \frac{4 P_{\text{abs}} n \ell}{h \nu_p \gamma c}. \quad (2.13)$$

For the polarization-switching experiment reported earlier [9], the calculated mode buildup time (assuming the cavity Q is switched instantaneously) is $\sim 0.6 \mu\text{s}$, an order of magnitude shorter than was obtained. This discrepancy is probably due to the slow Q-switching in the experiment; the Q was switched over a period longer than the observed mode buildup time.

Although it is possible to obtain faster polarization switching rates than we have demonstrated, the mode buildup times predicted by Equation (2.13) limit the maximum switching rates of the polarization-switchable Nd:YAG microchip laser to several megahertz for reasonable diode pump powers. Because of its small size and potential for low-cost mass production, however, the polarization-switchable microchip laser may find applications in specialized areas of optical communications.

J. J. Zayhowski

2.4 MICROCHIP LASER ARRAYS

Microchip lasers are flat-flat wafers of optical gain material, typically Nd:YAG, with mirror coatings deposited on their surfaces [10]. A stable laser cavity is formed by optical guiding from the pump-induced

radial index gradient [11]. As a result, the dielectrically coated wafers become microchip laser arrays when pumped with appropriately spaced diode laser arrays. Since the output of the diode pump defines the position of the oscillating mode, registration between the laser and pump source is automatic.

A 1×3 -element Nd:YAG microchip laser array was pumped by reimaging a linear diode-laser array in the gain medium using cylindrical optics, as shown in Figure 2-9. The spacing between the centers of the diodes in the array was 1 mm. A magnification factor of 10 was used in the dimension perpendicular to the diode junction (large divergence direction) to reduce the divergence of the pump light. In the dimension parallel to the junction the magnification was close to unity. Figure 2-10 shows the near-field intensity profiles. Each individual output beam was nearly circularly symmetric, with an eccentricity < 1.02 , an astigmatism of 9%, and a far-field divergence of 3.2 mrad. Careful measurements showed that the individual output beams were < 1.5 times diffraction limited compared to an ideal Gaussian beam. The three output beams were parallel to within 0.26 mrad and overlapped incoherently in the far field, as shown in Figure 2-11.

The crystal gain medium used in this experiment was polished to a thickness of 2.2 mm. This thickness was chosen to facilitate handling of the array and reduce the pump power required to reach threshold. Each of the three lasers operated in three longitudinal modes. By reducing the thickness of the gain medium it is possible to obtain single-longitudinal-mode operation, although for many applications this is not required.

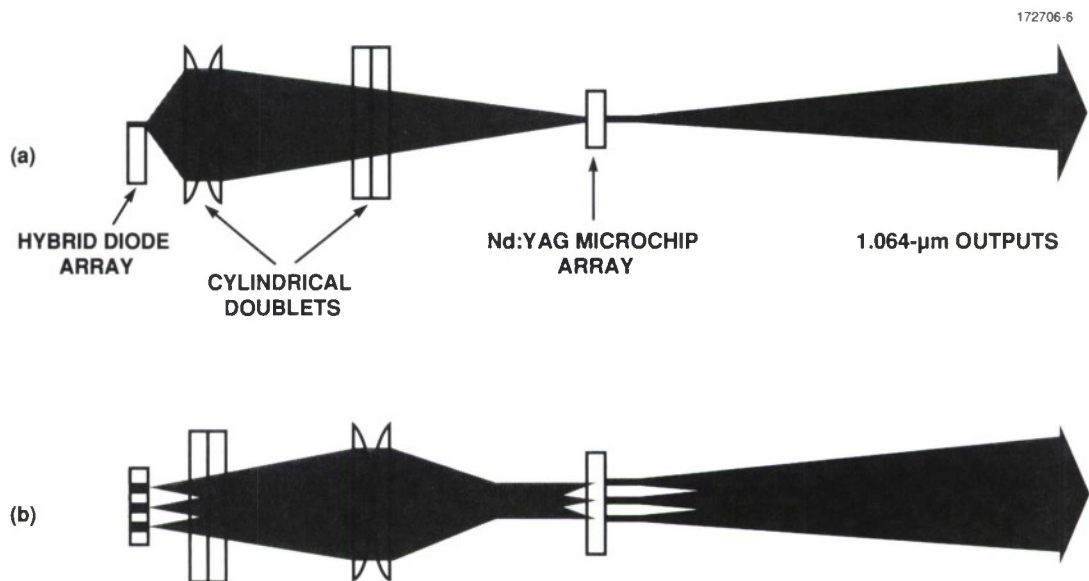


Figure 2-9. (a) Side view and (b) top view of the geometry used to pump the microchip laser array. The magnification of the cylindrical lenses was 10 times in the dimension perpendicular to the diode junction and unity in the dimension parallel to the junction. The individual $6\text{-}\mu\text{m}$ diodes were spaced 1 mm on center.

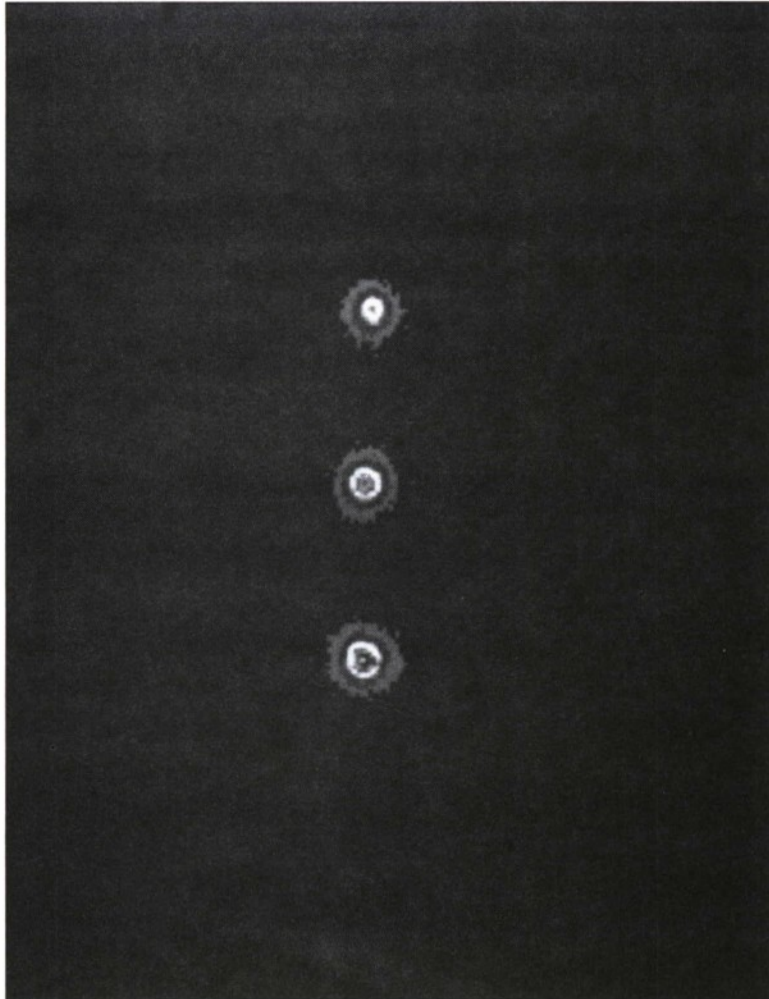


Figure 2-10. Near-field pattern of the output from the microchip laser array.

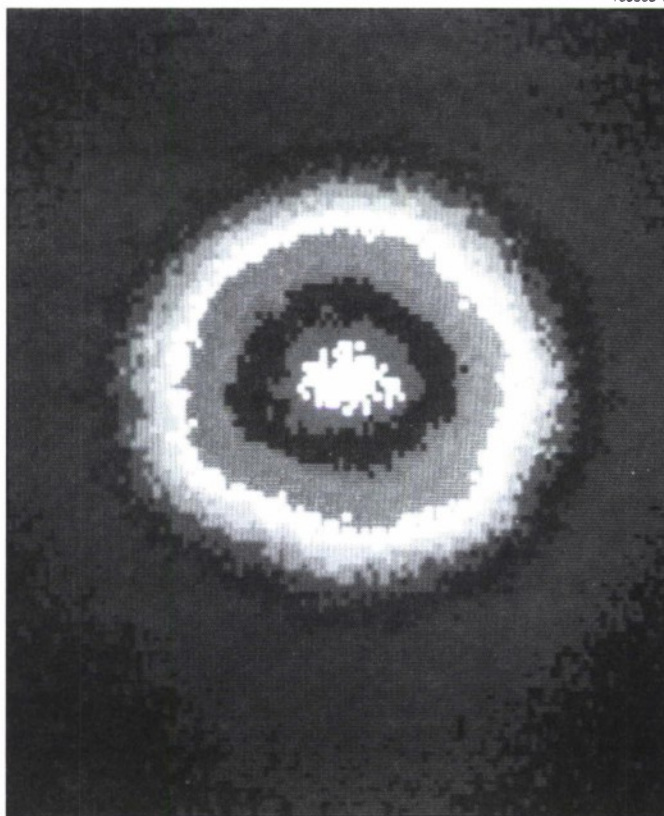


Figure 2-11. Far-field pattern of the output from the microchip laser array. The three black dots correspond to the centroid of the outputs from the three individual elements.

The pump-side mirror of the microchip laser array transmitted the pump light and had a reflectivity of 99.9% at the lasing wavelength. The output-side mirror reflected the pump light back into the laser crystal for improved efficiency and had a transmissivity of 2% at $1.064\ \mu\text{m}$. The three elements of the microchip array reached threshold at about the same pump power, corresponding to a total incident pump power of 225 mW. The overall slope power efficiency of the array was 18.4%. This poor efficiency is attributed to poor focusing in the dimension perpendicular to the junction of the diodes. Less than 50% of the light transmitted by the optics was focused into the lasing volume because of aberrations of the cylindrical optics. The same microchip laser arrays pumped with good mode quality $\text{Ti:Al}_2\text{O}_3$ lasers have achieved slope power efficiencies $> 70\%$.

The microchip laser array was also pumped with a butt-coupled diode laser array. Butt coupling increases the pump power required to reach threshold, but results in higher slope efficiencies. More detailed measurements need to be made for the butt-coupled geometry.

The spacing of the elements in the microchip laser array (1 mm on center) was chosen to be sufficiently large that the thermal waveguide for an element was not strongly affected by neighboring elements and that coherent optical interactions did not occur between neighboring lasers. This results in extremely robust devices, since the far-field pattern of the array is independent of the relative intensity and position of each of the individual elements. Such arrays have the potential to be scaled to arbitrary powers by increasing the number of array elements.

C. D. Nabors
J. J. Zayhowski
A. Mooradian

2.5 SINGLE-AXIAL-MODE INTRACAVITY-DOUBLED Nd:YAG LASER

A diode-pumped, single-axial-mode intracavity-doubled laser has been demonstrated using a cavity consisting of only two mirrors, a Brewster-angle-cut piece of Nd:YAG, and a KTP doubling crystal. Up to 4-mW single-ended output power has been obtained for 260-mW incident power on the Nd:YAG. Single-axial-mode operation is preferred in intracavity-doubled solid state lasers because there are large-amplitude fluctuations in the second-harmonic output in multi-axial mode lasers due to longitudinal mode coupling through sum-frequency generation [12]. Single-mode operation can be obtained with either an intracavity etalon or a unidirectional ring laser [13]; however, insertion of additional intracavity elements is required, which has the undesirable effect of increasing complexity and intracavity loss.

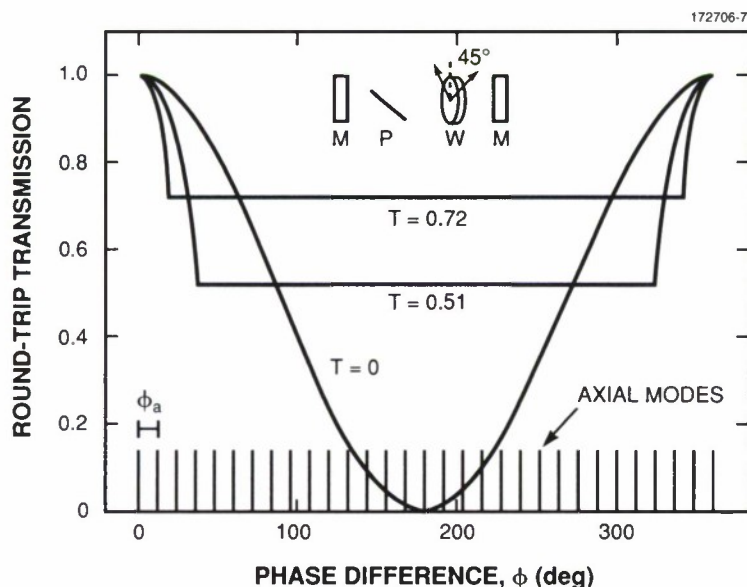


Figure 2-12. Round-trip transmission for a cavity containing a polarizer P and a waveplate W between two mirrors M as a function of ϕ . The curves are for three different values of single-pass power transmission for the lossy polarization through the polarizer, $T = 0$, $T = 0.72$, and $T = 0.51$. These values of T represent an ideal polarizer, a single Brewster-angle surface on YAG, and two Brewster-angle surfaces on YAG, respectively. The axial modes are also plotted assuming that $L/\Delta n l = 30$.

Single-axial-mode operation can be obtained in a standing-wave cavity by including a birefringent filter inside the cavity [14]. The polarizer for the birefringent filter can be a Brewster-angle entrance surface on the gain medium, and the waveplate can be the nonlinear crystal. The birefringent filter causes no loss at wavelengths for which the birefringent medium acts as a zero-wave waveplate. If the adjacent axial mode is separated in wavelength from the zero-loss mode by a sufficient amount, the additional loss will allow only a single mode to oscillate.

The round-trip transmission for a laser cavity containing a birefringent filter and the axial modes is shown in Figure 2-12; the axes of the polarizer are oriented at 45° to the axes of the birefringent element. The phase difference ϕ is given by $\phi = 4\pi\Delta n l/\lambda$ (modulo 2π), where l is the length of the birefringent element, Δn is its birefringence, and λ is the wavelength. The polarizer is assumed to be lossless for the allowed polarization and has a single-pass power transmission of T for the lossy polarization. Between adjacent birefringent filter maxima there are $L/\Delta n l$ axial modes, where L is the single-pass optical path length of the laser. For a sufficiently small $L/\Delta n l$, there can be a significant loss difference between a mode at the peak of the filter and the other modes.

Figure 2-13 shows the single-axial-mode intracavity-doubled laser. The Nd:YAG was 0.55 cm long and oriented for Brewster-angle entrance, and the antireflection-coated KTP was 0.5 cm long. The KTP was mounted on a thermoelectric cooler so that Δn could be adjusted to match a birefringent filter transmission maximum to the peak gain at $1.064 \mu\text{m}$. The two cavity mirrors were high reflectors at $1.064 \mu\text{m}$ with 5- and 50-cm radii of curvature, respectively. The output was taken through the mirror with 50-cm radius of curvature, which had $\sim 75\%$ transmission at $0.532 \mu\text{m}$. The single-pass optical path length of the cavity is ~ 3.8 cm. With these cavity parameters, the mode adjacent to a birefringent filter peak has 0.38% more loss than a mode at the birefringent filter peak. The laser was pumped by a diode array with an emitting aperture width of $100 \mu\text{m}$ with up to 260 mW incident on the Nd:YAG. The second-harmonic output was observed using a scanning confocal Fabry-Perot interferometer.

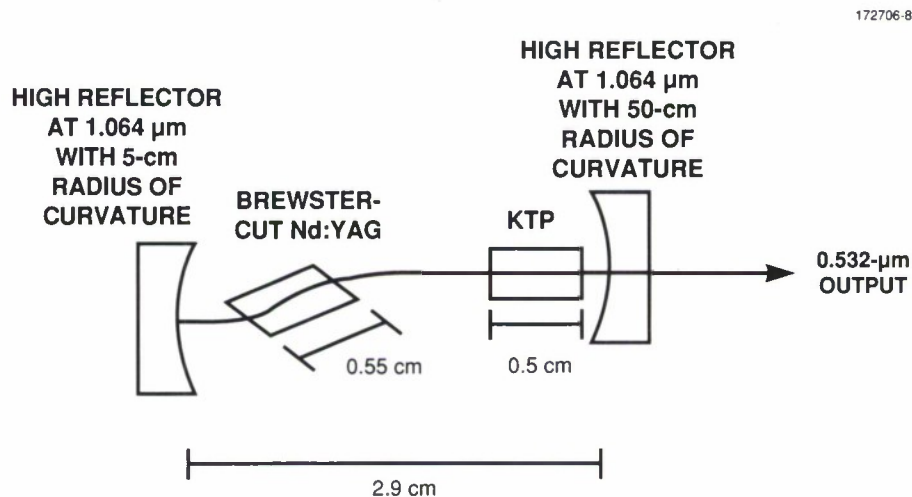


Figure 2-13. Schematic of the single-axial-mode intracavity-doubled Nd:YAG laser. The axes of the KTP are oriented 45° to the axes of the Brewster-angle faces. The Nd:YAG was placed close to the mirror with 5-cm radius of curvature, and the KTP was placed close to the mirror with 50-cm radius of curvature.

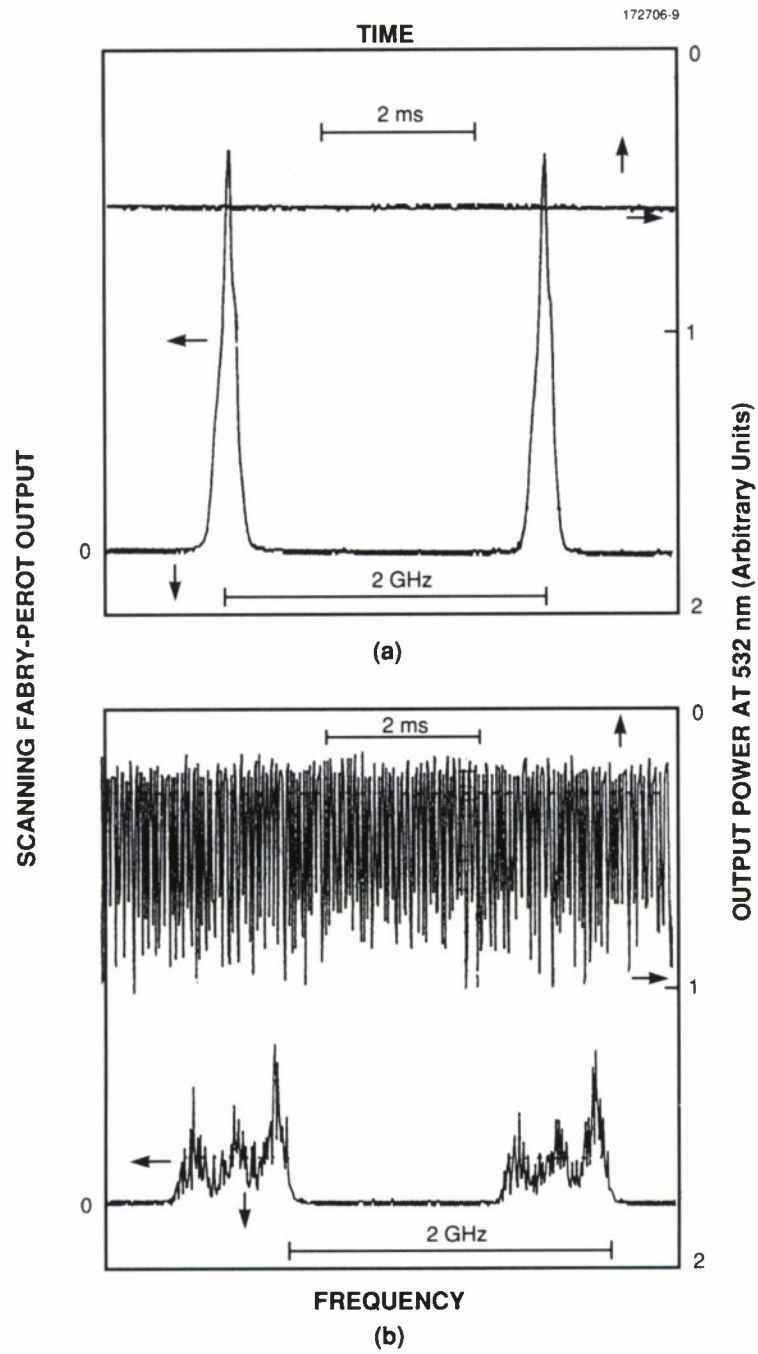


Figure 2-14. Output of the scanning confocal interferometer and a monitor photodiode under (a) single-mode operation and (b) multimode operation.

Figure 2-14 shows the output from the scanning confocal interferometer and a photodiode monitoring the green under single-mode and multimode operation. In multimode operation the output is noisy because of the longitudinal mode coupling effects, as expected. In single-mode operation no large-amplitude noise is present. We were able to attain up to 4-mW output power single ended in single-mode operation with 260 mW incident on the Nd:YAG. Threshold was reached at 31 mW of diode power incident on the Nd:YAG, and thus single-mode operation was attained at up to ~ 8.5 times threshold.

We believe that this laser could be optimized to operate further above threshold and to obtain higher conversion efficiency to the green. Improved mode discrimination could be obtained by using only a single Brewster-angle surface in the cavity. For a single Brewster-angle surface the loss for the adjacent mode would increase to 0.77% from the current 0.38%. The cavity could also be made shorter to space the axial modes farther apart. These improvements should allow single-mode operation further above threshold. Improved efficiency could be achieved by decreasing loss by coating mirrors directly onto the Nd:YAG and KTP. More optimum focusing of the cavity mode into the KTP would also help; the beam radius is $\sim 90\ \mu\text{m}$, while for confocal focusing into the KTP the required radius would be $\sim 22\ \mu\text{m}$.

In summary, we have demonstrated a diode-pumped, single-axial-mode intracavity-doubled Nd:YAG laser with up to 4-mW single-ended output power using only a Brewster-angle-cut piece of Nd:YAG and a KTP doubling crystal inside the laser cavity. Improved operation should be obtainable by optimizing cavity design to lower loss and by increasing longitudinal mode discrimination.

T. Y. Fan

2.6 CW OPERATION OF A DIODE-PUMPED ROTATING Nd:GLASS DISK LASER

A diode-pumped, CW rotating Nd:glass disk laser has been demonstrated, which promises scalability to very high average powers. Nd:glass lasers have previously been limited to relatively low average powers [15] by the poor thermal conductivity of glass, which results in thermally induced lensing, birefringence, or physical damage [16]. It has been proposed that these effects may be overcome in diode-pumped laser systems by rotating the Nd:glass to average the heat load over a much larger volume [17].

As shown in Figure 2-15, a cylindrical disk of Nd-doped phosphate glass, 0.5 cm thick and 5 cm in diameter, was inserted at Brewster's angle into a 12-cm-long linear stable laser cavity consisting of a high reflector (M1) at $1.054\ \mu\text{m}$ with a 5-cm radius of curvature, and a 1% output coupler M2 with a 10-cm radius of curvature. The disk was placed 4 cm from the high reflector such that the laser mode inside the Nd:glass disk had an elliptical cross section with major and minor axes of 315 and 175 μm (FWHM), respectively. The Nd:glass was end pumped through the high reflector by the focused output radiation from four linear GaAlAs diode laser arrays [18]. The diode-laser pump spot was located 2.2 cm from the center of rotation of the Nd:glass disk and had an elliptical cross section of axial dimensions $360 \times 200\ \mu\text{m}$ (FWHM). The laser always operated in the TEM_{00} mode with an output power that depended on both the diode laser pump power and the rate of rotation of the Nd:glass disk. The graph in Figure 2-16 demonstrates that as the rate of rotation of the disk was increased from zero, the output power of the laser increased from zero to a maximum and thereafter decreased. The initial increase in laser power with rotation rate is attributed to distributing the pumping heat load over a larger volume of Nd:glass, which decreases thermal effects. At higher rates of rotation, the decrease

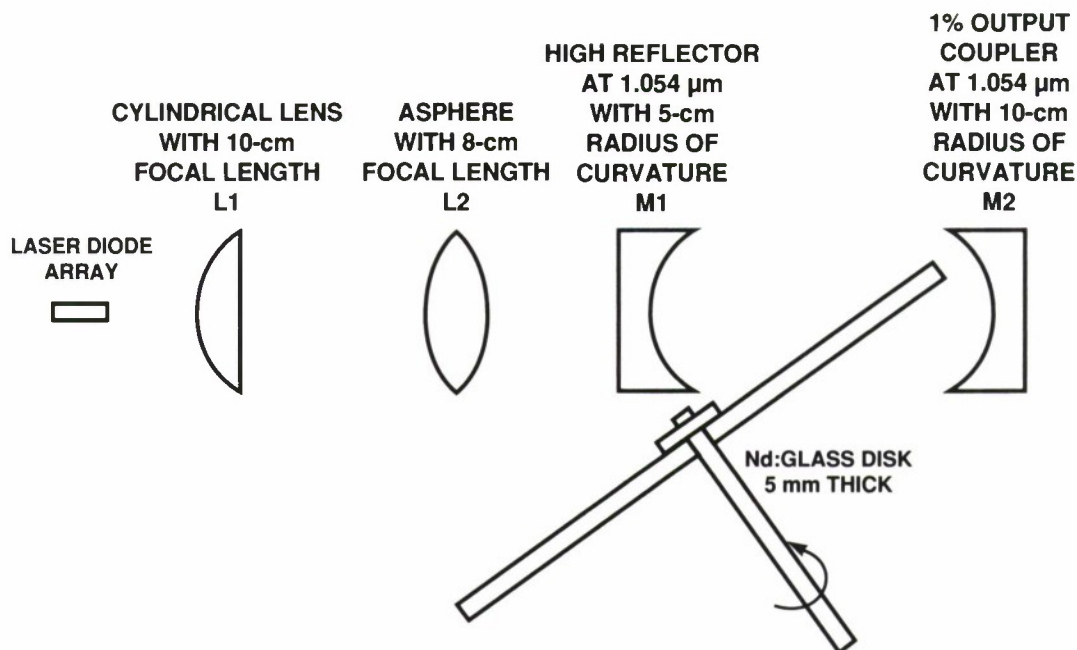


Figure 2-15. Schematic of the end-pumped rotating Nd:glass disk laser. M1 and M2 serve as the cavity mirrors. Lenses L1 and L2 collimate the diode radiation and focus it into the disk.

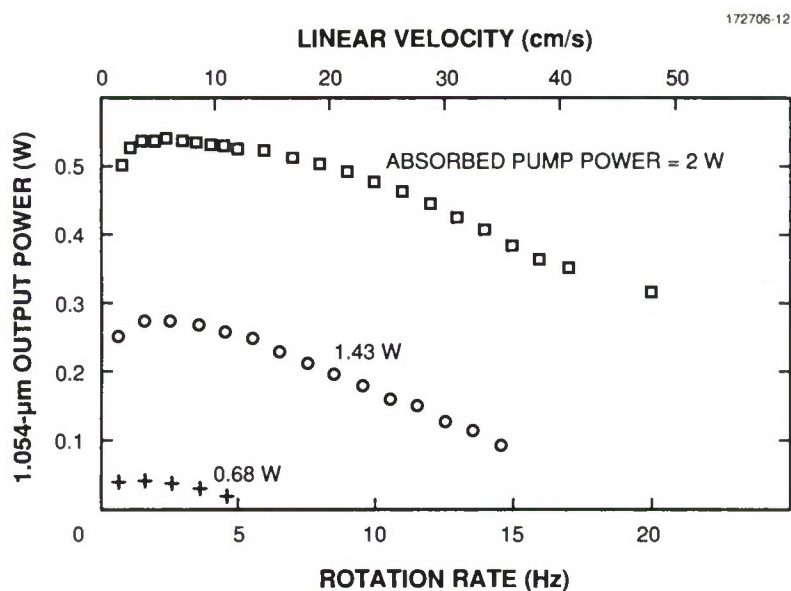


Figure 2-16. 1.054- μm output power vs rotation rate (linear velocity), with absorbed pump power as a parameter.

in laser power is attributed to decreased laser gain caused by moving some of the excited state population out of the laser mode before the energy can be extracted as laser radiation. The optimum rate of rotation of the disk, resulting in maximum laser power, increased as the pump power increased. A maximum at 0.55-W output power was obtained with an absorbed pump power of 2 W and a disk rotation rate of 2.5 Hz. Furthermore, at this rotation rate a slope efficiency of 37% was obtained. To our knowledge this is the highest reported power of a CW Nd:glass laser.

Substantially higher output powers should be possible from rotating disk lasers by increased pump powers and active longitudinal cooling of the disks. Higher-power Nd:glass lasers could operate over a larger spectral bandwidth than other Nd-doped crystals and should allow continuous mode-locked operation with short pulses.

J. Korn
T. H. Jeys
T. Y. Fan

2.7 HIGH-AVERAGE-INTENSITY SUM-FREQUENCY MIXING OF Nd:YAG LASER RADIATION IN LiB_3O_5

The utility of a nonlinear crystal for efficient sum-frequency mixing is determined not only by the nonlinear coefficients of the crystal but often, more importantly, by the phase-matching and optical-damage characteristics of the crystal. Efficient mixing of low-peak-power radiation places severe constraints on the nonlinear crystal. In order to achieve efficient mixing of low-peak-power radiation, the radiation must be tightly focused into the nonlinear crystal to achieve high peak intensities. However, the angular content of the focused radiation must be kept to less than the phase-matching angular acceptance of the crystal. The relatively narrow angular acceptance of such crystals as KD^*P , LiIO_3 , and KNbO_3 limits the degree of focusing that can profitably be applied to the pump radiation.

If, in addition, the radiation is CW or is pulsed with a high duty cycle, tight focusing results in a high average intensity at the focus. The high average intensity can produce substantial local heating of the crystal if there is absorption of even a small fraction of either the incident radiation or the sum-frequency radiation. Local heating of the crystal will bring about a local temperature gradient. This can adversely affect the sum-frequency-mixing efficiency if the gradient exceeds the phase-matching temperature acceptance of the crystal or if the gradient results in physical stress to the crystal; such stress can affect the phase-matching process or cause physical damage to the crystal. High average intensities can also result in photorefractive damage to the crystal. In particular, the small temperature acceptance, relatively high optical absorption coefficients, and high susceptibility to photorefractive damage of crystals such as LiNbO_3 and KNbO_3 severely limit the utility of these crystals in high-average-intensity applications. Table 2-1 lists the phase-matching characteristics for frequency summing of 1.06- and 1.32- μm radiation in several nonlinear crystals.

TABLE 2-1

**Phase-Matching Characteristics for Frequency Summing of 1.06- and 1.32- μ m Radiation
in Several Nonlinear Crystals**

Material	Type of Phase Matching	$d_{\text{eff}}^{(a)}$ (pm/V)	Figure of Merit (pm/V) ²	Walkoff Angle (deg)	FWHM Acceptance		
					Angular (mrad cm)	Spectra ^(b) (Å cm)	Thermal (°C cm)
LiIO ₃	I	1.9 [19]	0.54	3.9	0.4	5.2	Large
β -BaB ₂ O ₄	I	2.1 [19]	1.0	3.0	0.6	58	55 ^(b)
KNbO ₃ ^(c)	I	13.9 [20]	17.7	3.4	0.4	1.2	0.3 ^(b)
KD*P	II ^(d)	0.4 [19]	0.004	1.5	2.0	55	7 ^(b)
KD*P	III ^(d)	0.3 [19]	0.0025	1.1	3.3		
KTP ^(e)	II	2.9 [19]	1.5	2.5	1.5	5.6	25 ^(b)
KTP ^(e)	III	3.2 [19]	1.8	1.3	3.2		
LiNbO ₃ ^(f)	I	5.9 [21]	3.2	0	40		0.35 ^(g)
LiB ₃ O ₅ ^(h)	I	1.24 [22]	0.38	0	50		6 ^(g)

(a) Effective nonlinear coefficient values given in [19] – [22].

(b) 1.06- μ m second-harmonic-generation values (for reference only).

(c) Beams directed in *bc* plane.

(d) Type II, 1.32- and 0.589- μ m polarizations parallel; Type III, 1.06- and 0.589- μ m polarizations parallel.

(e) Beams directed in *xz* plane.

(f) Noncritically temperature phase matched; $T = 227^\circ\text{C}$, $\theta = 90^\circ$.

(g) Sum-generation values.

(h) Noncritically temperature phase matched; $T = 41^\circ\text{C}$, $\theta = 90^\circ$, $\phi = 0^\circ$.

Recently, lithium triborate (LiB₃O₅), a new nonlinear material, has become commercially available. This material has several advantages for efficient mixing of low-peak-power, high-duty-cycle Nd:YAG laser radiation. By temperature tuning, the crystal may be noncritically phase matched and therefore has a very large phase-matching angular acceptance. However, contrary to other temperature-tunable crystals, LiB₃O₅ retains a relatively large phase-matching temperature acceptance [23]. The relative mixing efficiency of LiB₃O₅ as a function of temperature is shown in Figure 2-17. The most interesting characteristic of LiB₃O₅ for high-average-intensity applications is its low optical absorption coefficients, which are [23] 1.2×10^{-3} , 1.8×10^{-3} , and $1.7 \times 10^{-3} \text{ cm}^{-1}$ at 1.32, 1.06, and 0.589 μ m, respectively. These low optical absorption coefficients reduce the deleterious effect of thermal gradients and contribute to the fact that LiB₃O₅ has a high damage threshold. These characteristics also allow tight focusing of high-duty-cycle radiation into LiB₃O₅.

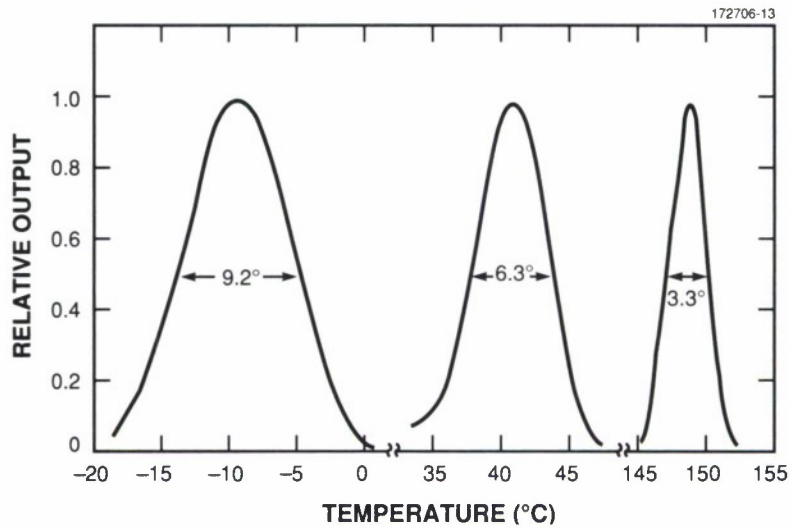


Figure 2-17. Relative doubling and mixing efficiencies of LiB_3O_5 as a function of temperature.

As part of a program to generate high-average-power sodium-resonance radiation by sum-frequency mixing of 1.06- and 1.32- μm Nd:YAG laser radiation [24],[25], we have generated 11 W of 589-nm radiation by focusing 39 and 15 W of 1.06- and 1.32- μm radiation, respectively, into an $\sim 160\text{-}\mu\text{m}$ spot within a LiB_3O_5 crystal. The measured external power conversion efficiency was 19 percent. The crystal was subjected to 0.3 MW/cm^2 of average intensity. The ability of any nonlinear crystal to withstand such a high average intensity is impressive.

The Nd:YAG oscillators, shown in Figure 2-18, were substantially modified commercially available lasers. The lasers produced 60- μs -long, relaxation-oscillation-free macropulses with a repetition rate of 840 Hz. Each of these macropulses consisted of a train of mode-locked micropulses spaced 10 ns apart. Each oscillator was operated in the stable regime and consisted of two flash-lamp-pumped, 4-mm-diam. by 135-mm-long Nd:YAG rods. Between the laser rods was a 90° polarization rotator (for thermal birefringence compensation) and an aperture (to restrict oscillation to the TEM_{00} mode). The intracavity mode lockers were driven by a common frequency source. By adjusting the relative phase of this frequency, the timing of the 1.06- and 1.32- μm micropulses could be adjusted to assure temporal overlap in the sum-frequency-mixing crystal. The FWHM of the micropulses was measured to be ~ 400 and ~ 500 ps for the 1.06- and 1.32- μm oscillators, respectively. Intracavity doubling crystals were used to suppress relaxation oscillations [26],[27] of the $\sim 60\text{-}\mu\text{s}$ macropulses produced by the oscillators. Each oscillator contained an etalon for wavelength control and either a Brewster plate or a dielectric polarizer to polarize the laser. The 1.32- μm oscillator also contained an intracavity dichroic mirror having high reflectivity at 1.06 μm and high transmission at 1.32 μm in order to prohibit lasing at 1.06 μm (the small-signal gain at 1.06 μm is ~ 5 times greater than at 1.32 μm). The 1.06- and 1.32- μm laser oscillators had 60 and 40% output couplers with average output powers of ~ 22 and ~ 11 W, respectively. The output of each oscillator could be amplified by a pair of Nd:YAG amplifiers to yield ~ 45 and ~ 17 W of polarized 1.06- and 1.32- μm laser power, respectively.

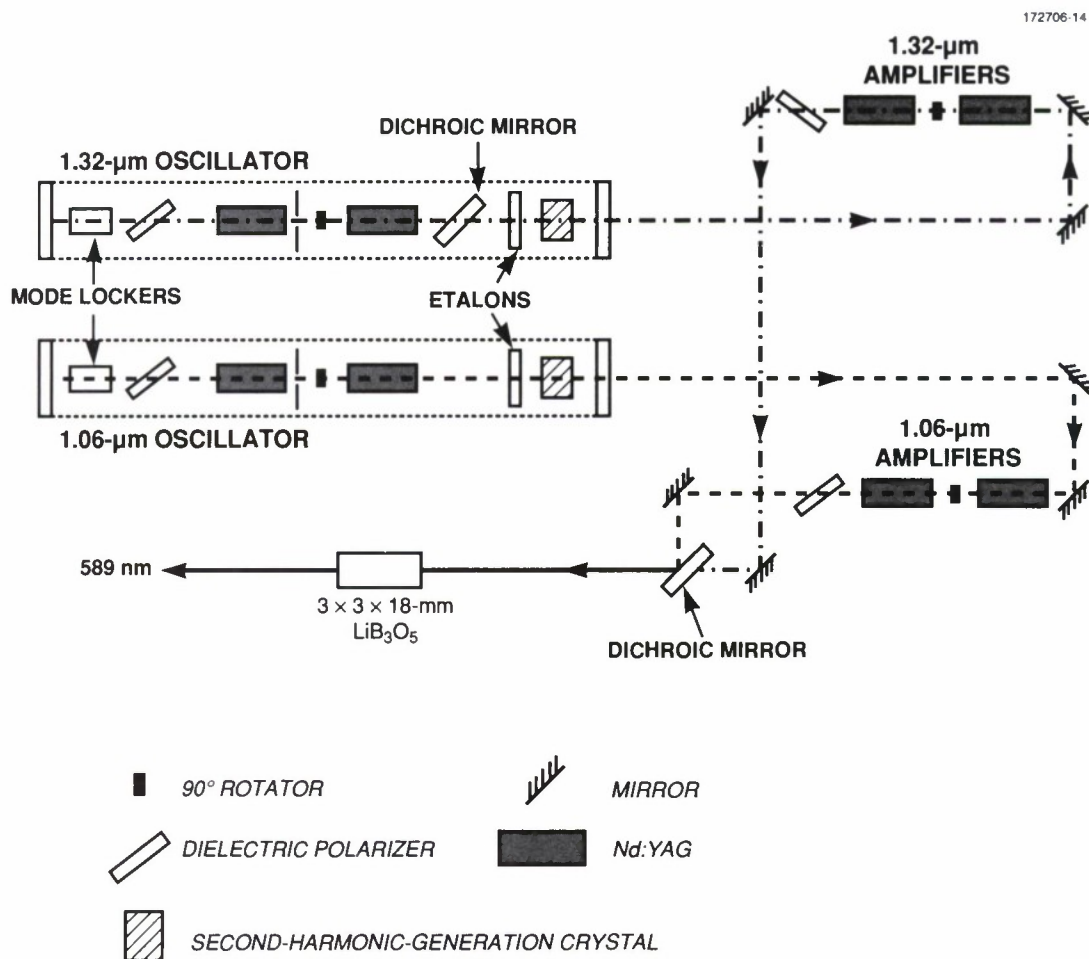


Figure 2-18. Schematic of the 1.06- and 1.32-μm Nd:YAG laser system for sum-frequency mixing in LiB₃O₅.

The 1.06- and 1.32-μm laser beams were combined with a dichroic mirror and focused by a 30-cm-focal-length lens to an $\sim 160\text{-}\mu\text{m}$ -diam. $(1/e^2)$ spot in a $2 \times 3.5 \times 18.2\text{-}\mu\text{m}$ LiB₃O₅ crystal. Tighter focusing of the incident laser beams was not found to be beneficial, even though the experimentally determined optimum beam diameter was found to be 3 times the calculated optimum for second-harmonic generation [28]. The nonlinear crystal was oriented for Type I noncritical phase matching, which was achieved by heating the crystal to a temperature of 41°C. The radiation propagated along the long dimension of the crystal.

The sum-frequency-mixing efficiency, using the oscillators alone, as a function of total input power is shown in Figure 2-19. The input power of the 1.06-μm laser was $1.32/1.06 = 1.24$ times that of the 1.32-μm laser (yielding an equal number of photons) at each point measured except the last point, where the ratio was 1.7. The departure of the last point from the roughly linear dependence of the rest of the data is probably due to the imbalance in the number of photons. The final data point corresponds to an input of 21.5 and 12.5 W for the 1.06- and 1.32-μm lasers, respectively, which yielded 5.2 W of 589-nm radiation.

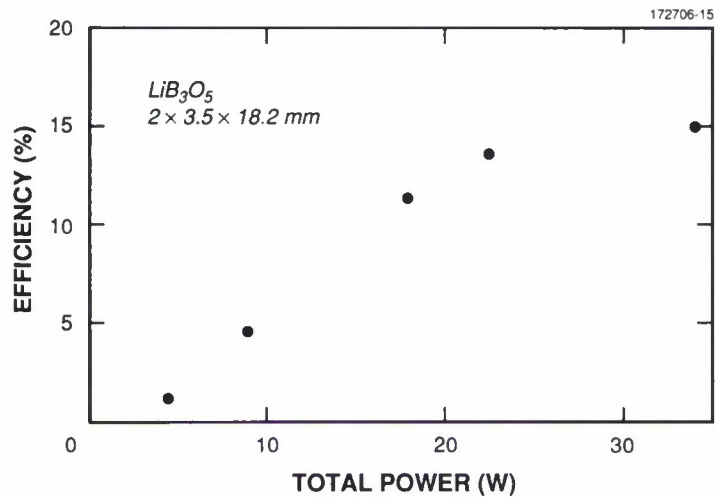


Figure 2-19. Sum-frequency-mixing efficiency as a function of total input power. In this experiment, only the output of the oscillators was used. The resulting data are roughly linear except for the last data point, at which we were no longer able to maintain the ratio of the 1.06- to 1.32- μm radiation at 1.24. The last data point corresponds to the generation of 5.2 W of 589-nm radiation with an input of 21.5 and 12.5 W of 1.06- and 1.32- μm radiation, respectively.

Using the amplifiers, we focused 39 and 15 W of 1.06- and 1.32- μm radiation, respectively, into the LiB_3O_5 and obtained 10.5 W of 589-nm radiation. Under these conditions we obtained an external power conversion of 19% and converted 31% of the 1.32- μm radiation. The average intensity under these conditions was about $0.3 \text{ MW}/\text{cm}^2$, and the peak intensity (at the center of the focused beam and at the time when the maximum intensity occurs) was $\sim 1 \text{ GW}/\text{cm}^2$. No photorefractive or physical damage was observed under these conditions.

In summary, we have found that LiB_3O_5 was able to withstand an average intensity of $0.3 \text{ MW}/\text{cm}^2$ without optical or photorefractive damage. Also, we have been able to achieve an average power conversion efficiency of 19%, which corresponds to the generation of 11 W of 589-nm radiation.

K. F. Wall	T. H. Jeys
N. Menyuk	J. Korn
T. C. Hotelling	W. A. Seemungal
M. E. MacInnis	

REFERENCES

1. K. J. Weingarten, D. C. Shannon, R. W. Wallace, and U. Keller, *Opt. Lett.* **15**, 962 (1990).
2. T. Sizer II, *Appl. Phys. Lett.* **55**, 2694 (1989); S. J. Walker, H. Avramopoulos, and T. Sizer II, *Opt. Lett.* **15**, 1070 (1990).
3. P. A. Schulz and S. R. Henion, to be published in *Opt. Lett.*

4. F. Krausz, C. H. Spielmann, T. Brabec, E. Wintner, and A. J. Schmidt, *Opt. Lett.* **15**, 1082 (1990).
5. A. E. Siegman, in *Lasers* (University Science Books, Mill Valley, CA, 1986), p. 1067.
6. G. T. Maker and A. I. Ferguson, *Opt. Lett.* **14**, 788 (1989).
7. Solid State Research Report, Lincoln Laboratory, MIT, 1990:4, p. 18.
8. A. E. Siegman, in *Lasers* (University Science Books, Mill Valley, CA, 1986), pp. 1008-1019;
A. Yariv, in *Quantum Electronics* (Wiley, New York, 1989), pp. 534-539.
9. Solid State Research Report, Lincoln Laboratory, MIT, 1990:4, p. 21.
10. J. J. Zayhowski and A. Mooradian, *Opt. Lett.* **14**, 24 (1989); *OSA Proc. Tunable Solid State Lasers*
(Optical Society of America, Washington D.C., 1989), p. 288.
11. J. J. Zayhowski, *OSA Proc. Advanced Solid State Lasers* (Optical Society of America, Washington,
D.C., 1990), p. 9; Solid State Research Report, Lincoln Laboratory, MIT, 1989:4, p. 26.
12. T. Baer, *J. Opt. Soc. Am. B* **3**, 1175 (1986).
13. R. Scheps and J. Myers, *1989 Tech. Dig. Series*, Vol. 18 (Optical Society of America, Washington,
D.C., 1989), p. 218.
14. A. Abramovici, *Opt. Commun.* **61**, 401 (1987).
15. T. Dimmick, *Opt. Lett.* **15**, 177 (1990).
16. F. Krausz, E. Winter, A. Schmidt, and A. Dienes, *IEEE J. Quantum Electron.* **26**, 158 (1990).
17. S. Basu and R. Byer, *Opt. Quantum Electron.* **22**, S33 (1990).
18. T. Y. Fan, A. Sanchez, and W. E. DeFeo, *Opt. Lett.* **14**, 1057 (1989).
19. R. C. Eckardt, H. Masuda, T. Y. Fan, and R. L. Byer, *IEEE J. Quantum Electron.* **26**, 922 (1990).
20. J. C. Baumert, J. Hoffnagle, and P. Günter, *Proc. SPIE* **492**, 374 (1984).
21. M. M. Choy and R. L. Byer, *Phys. Rev. B* **14**, 1693 (1976).
22. C. Chen, Y. Wu, A. Jiang, B. Wu, G. You, R. Li, and S. Lin, *J. Opt. Soc. Am. B* **16**, 616 (1989).
23. Solid State Research Report, Lincoln Laboratory, MIT, 1990:1, p.18.
24. T. H. Jeys, A. A. Brailove, and A. Mooradian, *Appl. Opt.* **28**, 2588 (1989).
25. Solid State Research Report, Lincoln Laboratory, MIT, 1989:4, p.18.
26. T. H. Jeys, *OSA Proc. Tunable Solid State Lasers* (Optical Society of America, Washington, D.C.,
1989), p. 337.
27. T. H. Jeys, to be published in *Appl. Opt.*
28. G. D. Boyd and D. A. Kleinman, *J. Appl. Phys.* **39**, 3597 (1968).

3. MATERIALS RESEARCH

3.1 LONG-WAVELENGTH $\text{Ge}_x\text{Si}_{1-x}/\text{Si}$ HETEROJUNCTION INFRARED DETECTORS AND 400×400 -ELEMENT IMAGER ARRAYS

The most highly developed technology currently available for large-area staring infrared focal plane arrays utilizes silicide Schottky-barrier detectors [1]. Since these detectors are fabricated on Si substrates by standard integrated circuit processing techniques, it is possible to manufacture large, highly uniform arrays of detectors that are monolithically integrated with charge-coupled device (CCD) or metal-oxide semiconductor readout circuitry. State-of-the-art Schottky-barrier arrays employ PtSi detectors for thermal imaging in the 3- to 5- μm spectral band [2]. Extension of the photoresponse into the long-wavelength infrared (LWIR) spectral band, ranging from 8 to 14 μm , has been demonstrated for IrSi arrays [3].

Recently, a new type of Si-based LWIR detector, utilizing internal photoemission over the heterojunction barrier [4] between a heavily doped p^+ - $\text{Ge}_x\text{Si}_{1-x}$ epitaxial layer and a p -Si substrate, has been demonstrated [5]. The barrier height (which is determined by the valence-band offset), and therefore the detector cutoff wavelength, can be tailored by varying the composition of the $\text{Ge}_x\text{Si}_{1-x}$ layer. Detectors sensitive out to at least 10 μm were fabricated, but even at 4.4 K these devices had dark-current densities in the range from 2 to $6 \times 10^{-4} \text{ A cm}^{-2}$, values that are much too high for practical applications.

In this investigation, we have fabricated GeSi detectors, with a range of cutoff wavelengths out to 16 μm , that exhibit nearly ideal thermionic-emission dark-current characteristics. (For convenience, we shall generally refer to the generic $\text{Ge}_x\text{Si}_{1-x}$ alloys as GeSi alloys and to GeSi/Si detectors as GeSi detectors.) We have also fabricated 400×400 -element imager arrays integrating $\text{Ge}_{0.44}\text{Si}_{0.56}$ detectors, which have a cutoff wavelength of 9.3 μm , with monolithic CCD readout circuitry. These arrays produce high-quality thermal images in the LWIR spectral band without uniformity correction. The $\text{Ge}_{0.44}\text{Si}_{0.56}$ composition was chosen in order to permit low-dark-current operation at about 50 K.

Individual detectors, incorporating $\text{Ge}_x\text{Si}_{1-x}$ layers 40 nm thick with $x = 0.22, 0.33, \text{ or } 0.42$, were fabricated on p -Si (100) substrates. The detector structure is similar to that previously reported [6] for silicide detectors, except that the GeSi layer replaces the silicide film. The GeSi layers for the individual detectors and the detector arrays were grown by coevaporation of Ge and Si sources in a molecular beam epitaxy system. The layers were doped with boron to a concentration of $\sim 1 \times 10^{20} \text{ cm}^{-3}$.

The 400×400 -element imager arrays utilize an interline transfer architecture with a monolithic CCD readout multiplexer [7]. Figure 3-1 is a schematic cross section of one pixel. Infrared radiation incident on the back side of the Si substrate is absorbed in the GeSi layer by free-carrier absorption, and photoexcited carriers are transferred to the buried-channel CCD controlled by a transfer-gate switch. An optical cavity, formed by deposition of a dielectric film and an Al mirror, is used to enhance optical absorption in the $\text{Ge}_{0.44}\text{Si}_{0.56}$ layer, which is 15 nm thick. The pixel size is $28 \times 28 \mu\text{m}$, and the fill factor is 40%.

The current-voltage characteristics of GeSi detectors were measured at temperatures between 30 and 90 K. These devices show ideal forward characteristics, with diode factors between 1.02 and 1.04. The reverse characteristics closely follow the ideal thermionic-emission equation [8]. Values of the effective barrier height

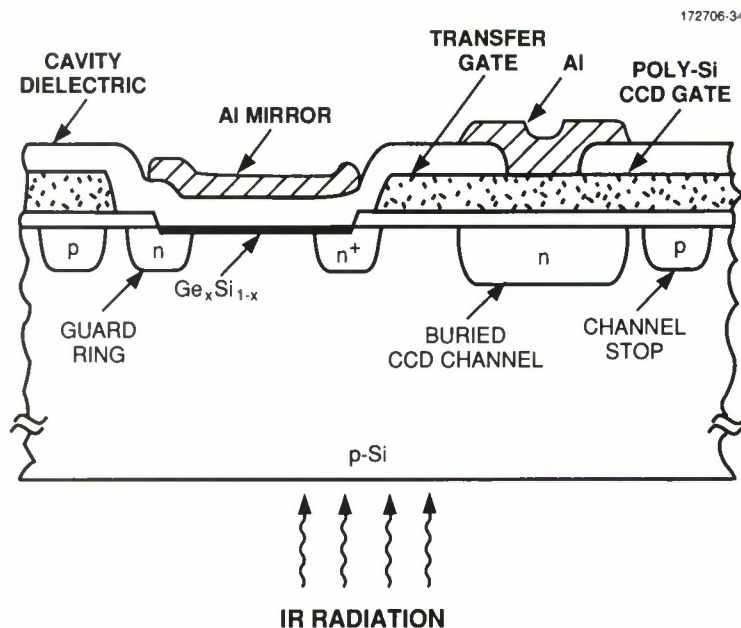


Figure 3-1. Schematic cross section of single pixel of GeSi infrared focal plane array.

ψ have been determined by activation analysis from the slopes of plots of J/T^2 vs $1/T$, where J is reverse-current density and T absolute temperature. Such plots, based on the values of J measured at a reverse voltage of 1 V, are shown in Figure 3-2 for detectors with $x = 0.42, 0.33$, and 0.22 . The values of ψ obtained are 0.125, 0.095, and 0.078 eV, respectively, corresponding to cutoff wavelengths of 9.9, 13.1, and 15.9 μm .

Figure 3-3 shows the quantum efficiency vs wavelength curves measured for the three detectors of Figure 3-2, all of which were operated at a reverse bias voltage of 2 V, and also for a high-performance IrSi detector with $\psi = 0.127$ eV. Like the GeSi detectors, the IrSi detector did not have an optical cavity. In order to reduce the dark current, the $\text{Ge}_{0.42}\text{Si}_{0.58}$ and IrSi detectors were cooled to 50 K, while the $\text{Ge}_{0.33}\text{Si}_{0.67}$ and $\text{Ge}_{0.22}\text{Si}_{0.78}$ detectors were cooled to 40 and 30 K, respectively. As the wavelength increases above 1 μm , the quantum efficiency of the IrSi detector decreases monotonically, but the efficiency of the GeSi detectors initially increases, reaches a maximum of 0.6 to 1.0% at ~ 3 μm , and then decreases. The initial increase in efficiency results from an increase in infrared absorption by the GeSi layer, which occurs because the absorption coefficient for free-carrier absorption in semiconductors exhibits a power-law dependence on wavelength [9]. Beyond the maximum, the efficiency decreases because the continuing increase in absorption is outweighed by the decrease in the probability of photoemission over the GeSi/Si heterojunction barrier as the photon energy and therefore the energy of the photoexcited carriers decreases. The decrease in quantum efficiency with increasing wavelength for the IrSi detector also results from the decrease in photoemission probability. The wavelength dependence of this probability is not the same, however, because the initial free-carrier energies extend over a broad continuum in the silicides, which are metallic, while in the semiconducting p^+ -GeSi alloys these energies are restricted to a narrow band just below the Fermi level.

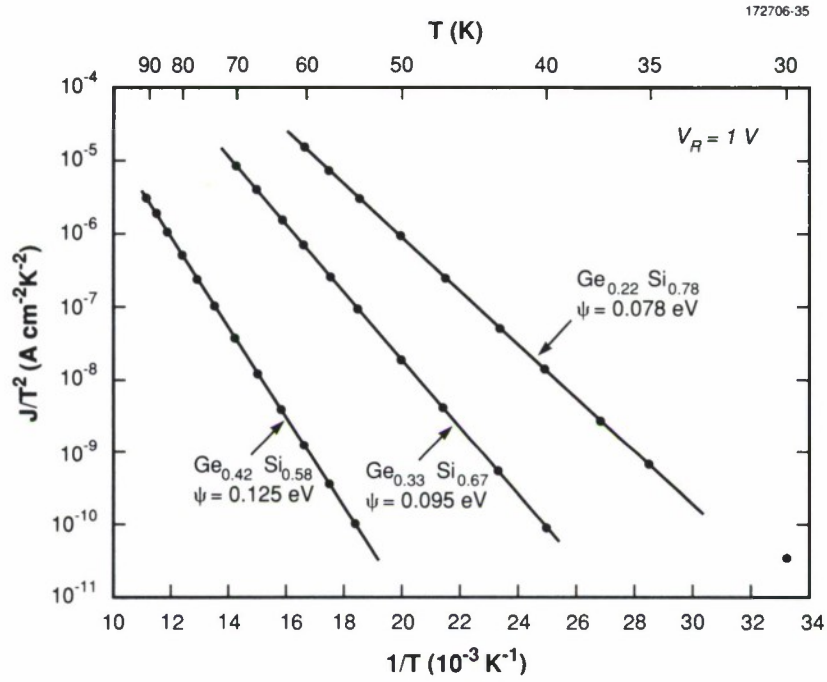


Figure 3-2. Plots of J/T^2 vs $1/T$ for three GeSi detectors operated at a reverse voltage V_R of 1 V.

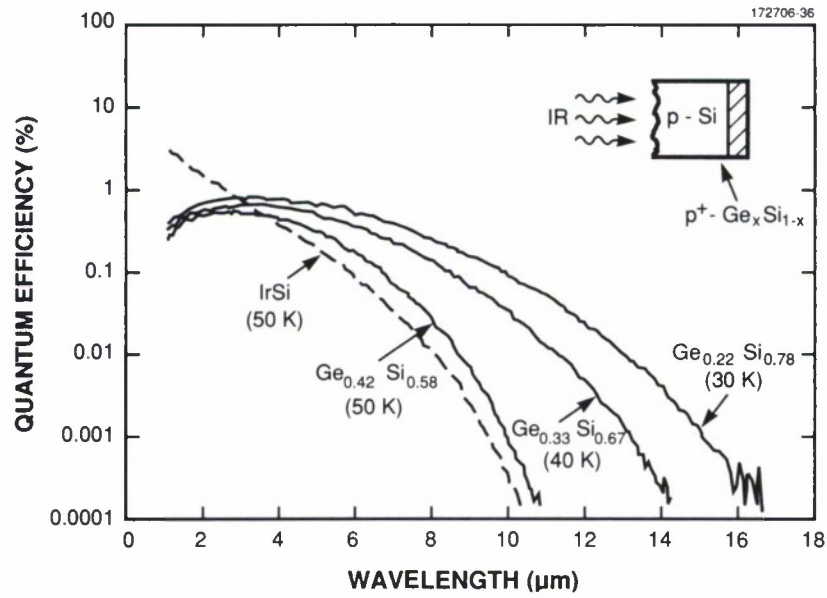


Figure 3-3. Quantum efficiency as a function of wavelength for the detectors of Figure 3-2 and an IrSi detector.

For wavelengths beyond $3\text{ }\mu\text{m}$, the quantum efficiency is systematically higher for the $\text{Ge}_{0.42}\text{Si}_{0.58}$ detector than for the IrSi detector, which has almost exactly the same value of ψ . While it is unlikely that the intrinsic efficiency of IrSi detectors can be substantially increased, the intrinsic efficiency of the GeSi detectors could probably be increased by optimizing the thickness of the GeSi layer and increasing the free-carrier absorption by higher boron doping.

A benchtop imaging camera was used to evaluate the performance of the 400×400 arrays, which were cooled to a nominal temperature of 53 K, where the dark-current density was $\sim 10^{-8}\text{ A cm}^{-2}$. For operation of the output CCD register at 5-MHz clock frequency with a bias charge injection [10] of 20%, the measured charge-transfer efficiency was 0.999 per stage. For imaging of near-room-temperature objects, the background signal charge exceeds 50%, so no bias charge injection is needed. At operating temperatures below 50 K, the transfer efficiency degrades severely even with bias charge injection, resulting in poor imager operation.

Figures 3-4(a) and 3-4(b) show thermal images of a 10-K, 4-bar test pattern and a man's face, respectively, that were obtained without uniformity correction. The imager was cooled to a nominal temperature of 53 K and operated at a frame rate of 30 Hz with an $f/2.35$ cold shield and a $7.5\text{-}\mu\text{m}$ long-pass filter. Visual inspection of the test pattern shows the minimum resolvable temperature is about 0.2 K. The measured responsivity nonuniformity for 295-K background exposure is less than 1% rms.

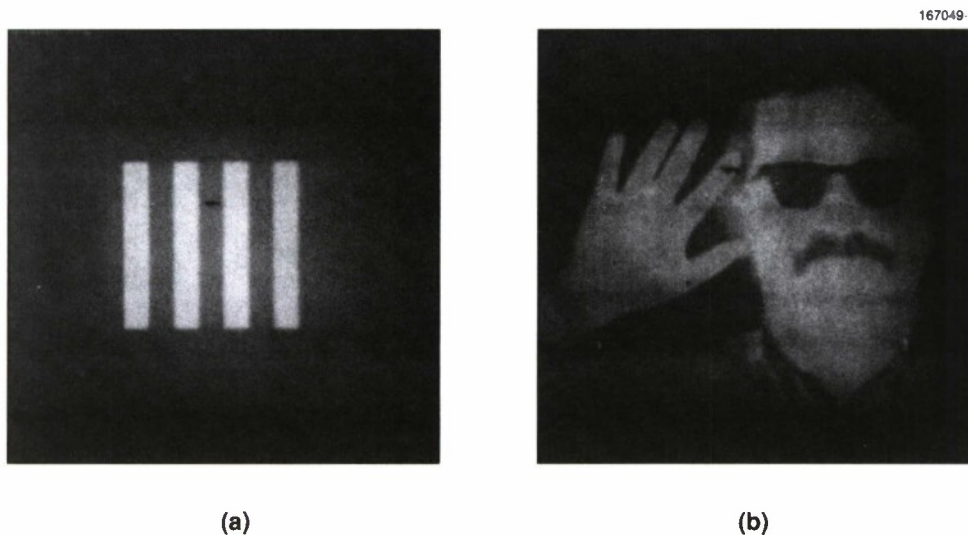


Figure 3-4. Uncorrected thermal images obtained with 400×400 GeSi imager array for (a) a 10-K test pattern and (b) a man's face. The imager was operated at a frame rate of 30 Hz with an $f/2.35$ cold shield and a $7.5\text{-}\mu\text{m}$ long-pass filter.

Like PtSi and IrSi arrays, GeSi arrays have the advantages of excellent uniformity and high yield that are associated with silicon-based technology. Furthermore, the cutoff wavelength can be extended to any desired value by adjusting the GeSi alloy composition. Development of a readout multiplexer capable of efficient operation at temperatures far enough below 50 K would permit the fabrication of very large, high-performance GeSi imager arrays with photoresponse out to 16 μm and beyond.

B-Y. Tsaui
C. K. Chen
S. A. Marino

3.2 HIGH-EFFICIENCY, HIGH-POWER GaInAsSb/AlGaAsSb DIODE LASERS EMITTING AT 2.3 μm

Double-heterostructure diode lasers incorporating a GaInAsSb active layer and AlGaAsSb confining layers lattice matched to a GaSb substrate are being developed to provide emission in the 2- to 5- μm spectral range. Room-temperature CW operation of narrow-stripe GaInAsSb/AlGaAsSb lasers has been achieved by two groups [11],[12]. We have previously reported [13] the room-temperature pulsed operation of broad-stripe GaInAsSb/AlGaAsSb lasers with an emission wavelength of 2.29 μm . These lasers, with a cavity length $L = 300 \mu\text{m}$, had threshold current density $J_{\text{th}} = 1.7 \text{ kA cm}^{-2}$, differential quantum efficiency $\eta_d = 36\%$, and output power of 290 mW per facet. In this report we describe the pulsed room-temperature operation of such lasers with substantially better performance: $\eta_d = 50\%$ and output power of 900 mW per facet [14]. For $L = 700 \mu\text{m}$, these lasers had $J_{\text{th}} = 1.5 \text{ kA cm}^{-2}$.

The GaInAsSb and AlGaAsSb layers were grown by molecular beam epitaxy in the manner described previously [13],[15]. The laser structure consists of the following layers: 0.2- μm -thick n^+ -GaSb buffer, 2- μm -thick n -Al_{0.50}Ga_{0.50}As_{0.04}Sb_{0.96} cladding, 0.4- μm -thick n -Ga_{0.84}In_{0.16}As_{0.14}Sb_{0.86} active, 3- μm -thick p -Al_{0.50}Ga_{0.50}As_{0.04}Sb_{0.96} cladding, 0.05- μm -thick p^+ -GaSb cap. The active layer composition was selected for lasing at 2.3 μm . The carrier concentrations in the n - and p -AlGaAsSb cladding layers are about 1×10^{17} and $6 \times 10^{16} \text{ cm}^{-3}$, respectively.

Lasers 300 μm wide were fabricated by the technique used previously [13] and probe tested under pulsed operation at room temperature. Figure 3-5 shows the emission spectrum of a laser with $L = 300 \mu\text{m}$. The spectrum has multiple longitudinal modes with the peak located at 2.275 μm . From the mode spacing of about 2.3 nm, the group refractive index n^* is about 3.71, where $n^* \equiv n[1 - (\lambda/n)(dn/d\lambda)]$, n is the effective refractive index of the double heterostructure, and λ is the wavelength. Figure 3-6 shows the light output vs current measured using 200-ns pulses for another laser with $L = 300 \mu\text{m}$. The value of η_d is 50%, and the maximum power is 900 mW per facet obtained at 9A. These are the highest room-temperature values obtained for any semiconductor laser emitting beyond 2 μm .

Figure 3-7 shows the dependence of J_{th} on L . As L increases from 300 to 700 μm , J_{th} decreases from 1.85 to 1.5 kA cm^{-2} , which is equal to the lowest reported value for GaInAsSb/AlGaAsSb lasers [11]. Figure 3-8 is a plot of η_d^{-1} vs L obtained using 500-ns pulses. The value of η_d decreases from 47% for $L = 300 \mu\text{m}$ to 27% for $L = 700 \mu\text{m}$. From the slope of the line drawn through the data points, the internal loss coefficient is calculated to be 43 cm^{-1} , which is comparable to values obtained for GaInAsP/InP double-heterostructure lasers. The internal quantum efficiency obtained from the y-intercept is 100%.

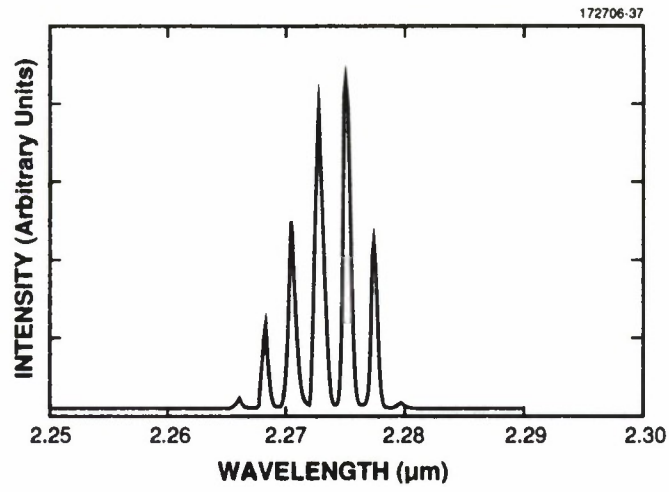


Figure 3-5. Emission spectrum of GaInAsSb/AlGaAsSb diode laser for pulsed operation at room temperature.

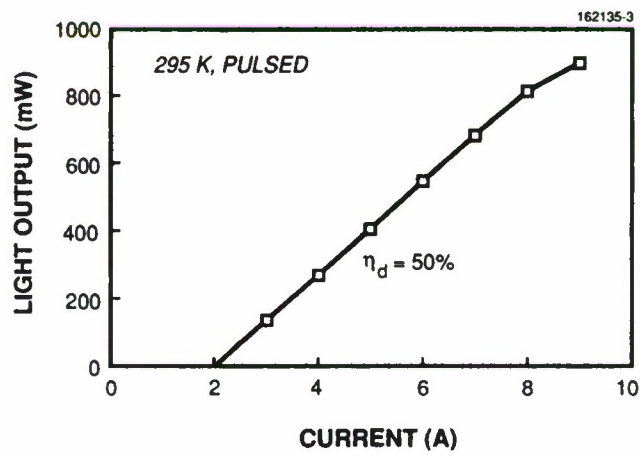


Figure 3-6. Light output vs current for a laser 300 μm wide by 300 μm long.

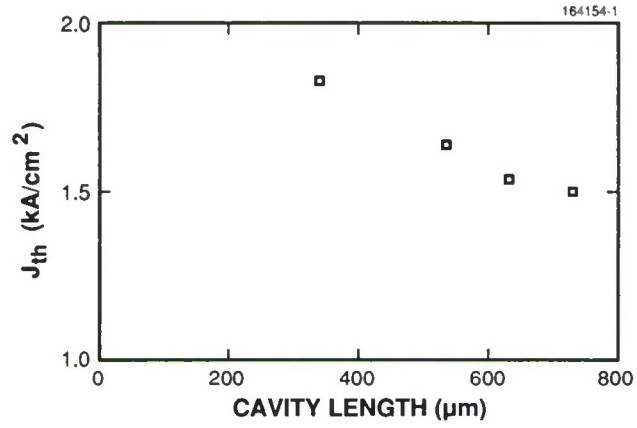


Figure 3-7. Dependence of threshold current density on cavity length.

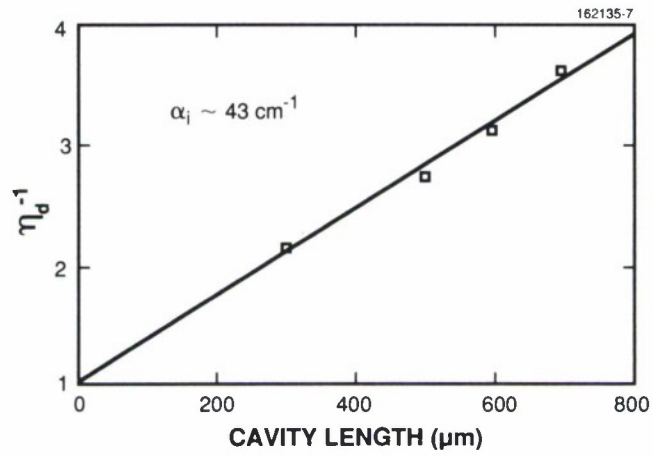


Figure 3-8. Dependence of inverse differential quantum efficiency on cavity length.

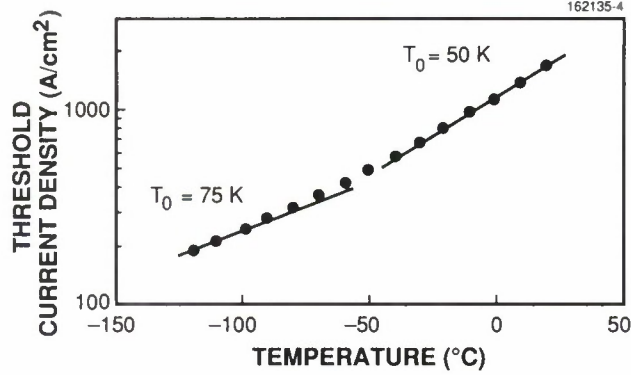


Figure 3-9. Dependence of threshold current density on temperature for a laser 300 μm wide by 300 μm long.

Light output vs current curves were measured at temperatures from -120 to 20°C for a laser with $L = 300 \mu\text{m}$. Figure 3-9 shows J_{th} as a function of temperature. At -120°C , $J_{\text{th}} = 190 \text{ A cm}^{-2}$. The characteristic temperature T is 75 K near -120°C and 50 K near 20°C . These values are comparable to the best values that have been reported for GaInAsSb/AlGaAsSb lasers [11],[16].

H. K. Choi
 S. J. Eglash
 W. L. McGilvary
 J. V. Pantano

3.3 ROLE OF GaAs BOUNDING LAYERS IN OMVPE GROWTH OF STRAINED-LAYER InGaAs/AlGaAs DIODE LASERS

Diode lasers containing a strained InGaAs quantum-well active layer are attracting great interest because these devices can exhibit significantly better performance and lower degradation rates than GaAs/AlGaAs lasers. In addition, the emission wavelength can be extended from 870 nm for GaAs active layers to about $1.1 \mu\text{m}$ for InGaAs layers [17]. The performance of the strained-layer lasers depends on both the device structure and the epitaxial growth procedure. Besides the InGaAs active layer, the basic structure typically includes AlGaAs or GaAs confining layers, AlGaAs cladding layers, and GaAs buffer and contact layers. High-performance devices have been grown by both organometallic vapor phase epitaxy (OMVPE) [18]-[21] and molecular beam epitaxy [22],[23]. In all cases, the InGaAs layer was grown at a temperature much lower, generally by 100 to 200°C , than the temperature used for the AlGaAs layers. Before and after deposition of the InGaAs layer, alloy growth was interrupted while the substrate temperature was being decreased and increased, respectively, and thin lower and upper GaAs bounding layers sandwiching the InGaAs layer were grown during the two alloy growth interruptions.

In two of the earlier studies [19],[21], it was shown that the GaAs bounding layers produce a strong improvement in InGaAs/AlGaAs laser performance. In the second of these studies, we compared the pulsed operating characteristics of graded-index separate-confinement heterostructure single-quantum-well (GRINSCH-SQW) lasers having an $\text{In}_{0.25}\text{Ga}_{0.75}\text{As}$ active layer that were grown by OMVPE with and without 10-nm-thick bounding layers. For broad-area devices with a cavity length of $500\text{ }\mu\text{m}$, incorporation of these layers decreased the threshold current density J_{th} from 550 to 125 A cm^{-2} and increased the differential quantum efficiency η_d from 46 to 80%.

The present investigation was undertaken to determine the role of the bounding layers in improving InGaAs/AlGaAs laser performance. Initial experiments on GRINSCH-SQW lasers showed that this performance is influenced more by the upper bounding layer than by the lower one. Further experiments on InGaAs/GaAs test structures showed that the role of the upper bounding layer is to prevent the loss of In from the InGaAs layer by evaporation during the time when the substrate is being heated to the temperature required for growing the upper AlGaAs and GaAs layers.

The GRINSCH-SQW structures and test structures were grown on GaAs substrates in a vertical rotating-disk OMVPE reactor [24] by using the technique described previously [21]. Figure 3-10 is a schematic diagram of the GRINSCH-SQW structure, which has an $\text{In}_{0.25}\text{Ga}_{0.75}\text{As}$ active layer. The substrate temperatures used in growing this structure were selected on the basis of experiments that had been performed to establish the optimum conditions for deposition of GaAs, AlGaAs, and InGaAs. First, the GaAs buffer and lower AlGaAs cladding and confining layers were grown at 800°C . Alloy growth was then interrupted for ~ 3 min while the temperature was lowered to 640°C . The lower GaAs bounding layer (if one was used) was

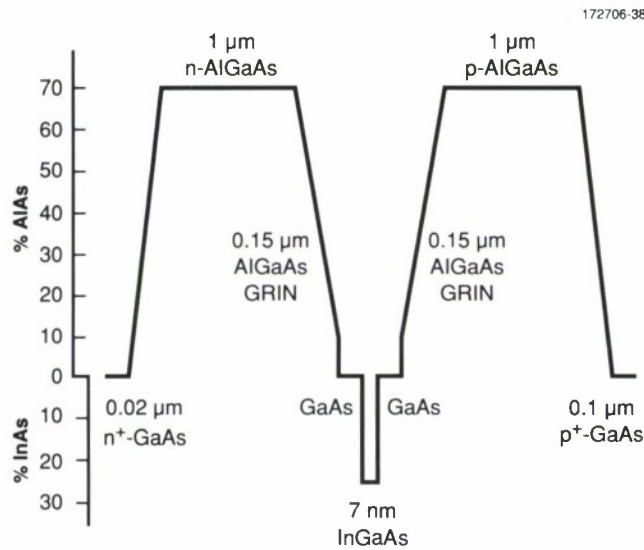


Figure 3-10. Schematic diagram showing structure of InGaAs/AlGaAs GRINSCH-SQW diode laser.

deposited during this time. After growth of the InGaAs active layer at 640°C, alloy growth was again interrupted for ~ 3 min, and the upper bounding layer (if one was used) was deposited while the temperature was increased to 800°C. The upper AlGaAs confining and cladding layers were grown at 800°C, and the temperature was lowered to 640°C for growth of the p^+ -GaAs cap layer. During all growth interruptions, a flow of arsine was maintained to prevent formation of a metal-rich surface.

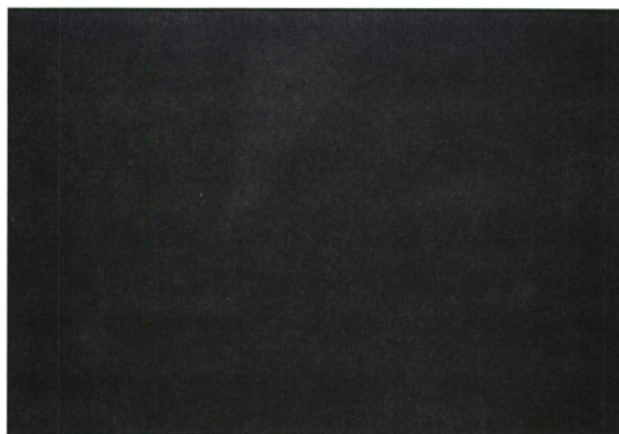
Table 3-1 compares the properties of five GRINSCH-SQW structures with upper and lower GaAs bounding layers of various thicknesses. Bounding layers 10 nm thick were grown in seven deposition steps with an interruption time of about 20 s between successive depositions, while 2- and 2.5-nm-thick bounding layers were grown in one step. For each structure, broad-stripe lasers were fabricated and tested in the manner described previously [21]. Scanning electron micrographs of the surface of structures A and E are shown in Figure 3-11, and room-temperature photoluminescence (PL) spectra for all but structure B are shown in Figure 3-12. Structure A, with upper and lower bounding layers both 10 nm thick, had the best properties. This structure had smooth surface morphology, the strongest PL peak (indicating the best InGaAs crystal quality), the lowest J_{th} (114 A cm⁻²), and the highest η_d (80%). (Almost the same operating characteristics were obtained previously for lasers of similar GRINSCH-SQW structure that also had 10-nm-thick upper and lower bounding layers [21].) The properties were almost as good for the other two structures with an upper bounding layer 10 nm thick, which had either a lower bounding layer only 2.5 nm thick (structure B) or no lower bounding layer at all (structure C). In comparison to structure A, these structures had equally smooth surface morphology and the same value of η_d , but their PL intensities were somewhat lower and their J_{th} values somewhat higher.

TABLE 3-1
Effect of Upper and Lower GaAs Bounding Layers on Laser Structures

Laser Structure	Boundary Layer Thickness		Surface Morphology	Relative PL	J_{th} (A cm ⁻²)	η_d (%)
	Lower (nm)	Upper (nm)				
A	10	10	Smooth	1	114	80
B	2.5	10	Smooth	0.94	124	80
C	0	10	Smooth	0.74	130	80
D	10	2	Rough	0.52	129	78
E	10	0	Rough	0.44	216	66

For the two structures that had a 10-nm-thick lower bounding layer but for which the upper bounding layer was either only 2 nm thick (structure D) or omitted altogether (structure E), the surface morphology was rough and the PL intensity considerably lower than for structures A, B, and C, while η_d was reduced to 78 and 66%, respectively. For structure D, J_{th} (129 A cm⁻²) was almost the same as for structure C (130 A cm⁻²). For structure E, however, J_{th} increased sharply to 216 A cm⁻². Thus, the omission of the upper bounding layer produces a much larger increase in J_{th} than omission of the lower bounding layer (as in structure C). However, the increase is greatly reduced by the deposition of an upper bounding layer only 2 nm thick in one step immediately after InGaAs growth (as in structure D).

172706-53



(a)



1 μm

(b)

Figure 3-11. Scanning electron micrographs showing surface morphology of (a) GRINSCH-SQW structure A and (b) GRINSCH-SQW structure E.

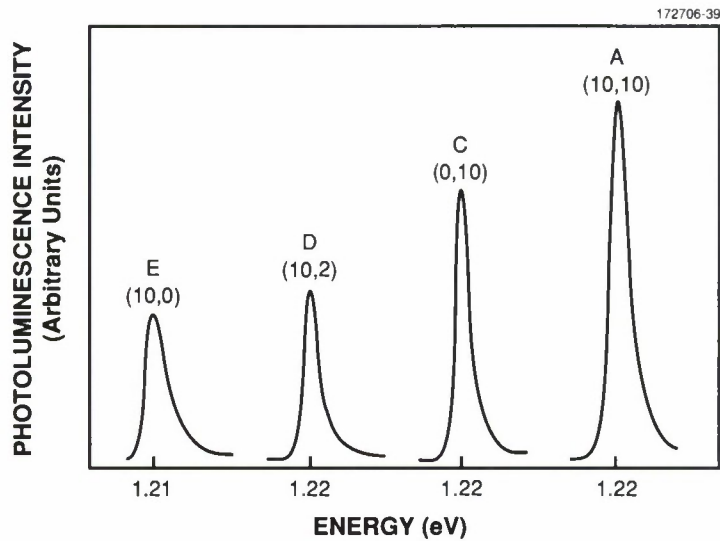


Figure 3-12. Room-temperature PL spectra for GRINSCH-SQW structures A, C, D, and E. For each sample the thicknesses (in nanometers) of the lower and upper GaAs bounding layers, respectively, are given by the first and second numbers in parentheses (see Table 3-1).

In view of the importance of the upper bounding layer in achieving the best laser performance, we have employed an InGaAs/GaAs SQW test structure to investigate the role played by this layer. Figure 3-13 is a schematic cross-sectional diagram of the test structure, which consists of a 0.5- μm -thick GaAs lower layer, a 10-nm-thick $\text{In}_{0.25}\text{Ga}_{0.75}\text{As}$ quantum well, and a 20-nm-thick GaAs upper layer. Most of the lower GaAs layer was grown at 800°C. The substrate was then cooled to 640°C over a period of several minutes without interrupting GaAs growth. Next, the InGaAs layer was grown at 640°C. Two different procedures were followed for growing the upper GaAs layer. For sample A, this layer was deposited at 640°C with no growth interruption. For sample B, growth was interrupted for 4 min while the substrate was heated to 800°C under a constant arsine flow, and the upper GaAs layer was then deposited at 800°C. Thus, the treatment of the InGaAs layers in samples A and B was similar to the treatment of the active layers in the GRINSCH-SQW laser structures grown with and without an upper bounding layer, respectively.

Scanning electron micrographs comparing the surface morphologies of samples A and B are shown in Figure 3-14. Consistent with the results for the GRINSCH-SQW structures, the surface of sample A is smooth and featureless, while that of sample B is rough. Room-temperature PL spectra for the two samples are shown in Figure 3-15. Although the wavelength of the peak is about the same in the two spectra, the peak for sample B is broader and only about half as intense as that for sample A. The broadening can be attributed to the poorer surface morphology. The reduction in intensity, which is also observed for the GRINSCH-SQW structures without an upper bounding layer, indicates an increase in the density of nonradiative recombination centers.

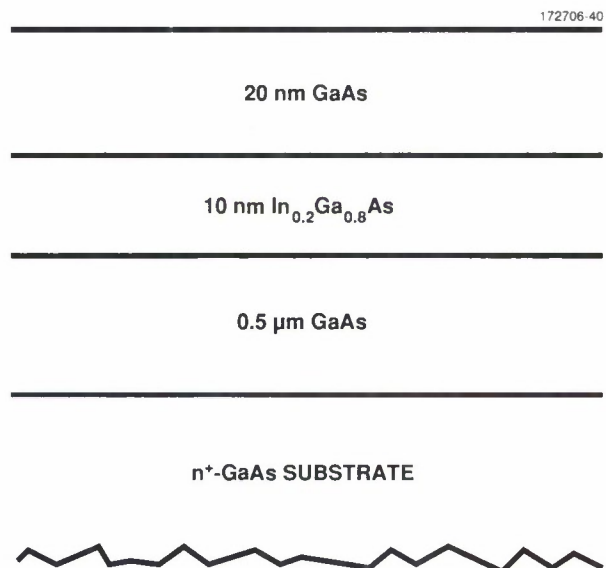


Figure 3-13. Schematic cross-sectional diagram of InGaAs/GaAs test structure.

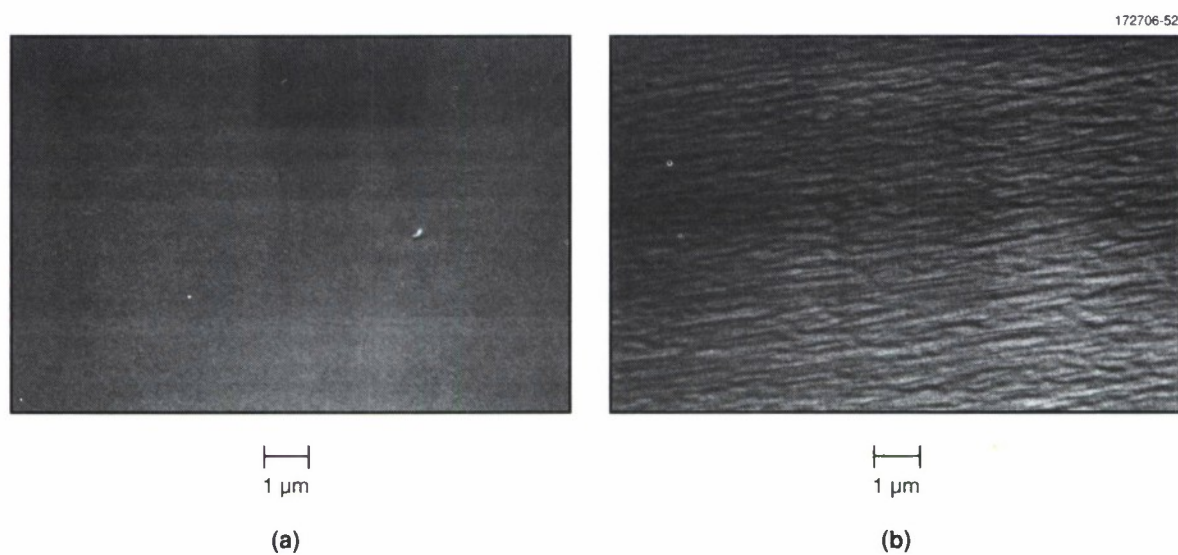


Figure 3-14. Scanning electron micrographs showing surface morphology of (a) test-structure sample A and (b) test-structure sample B.

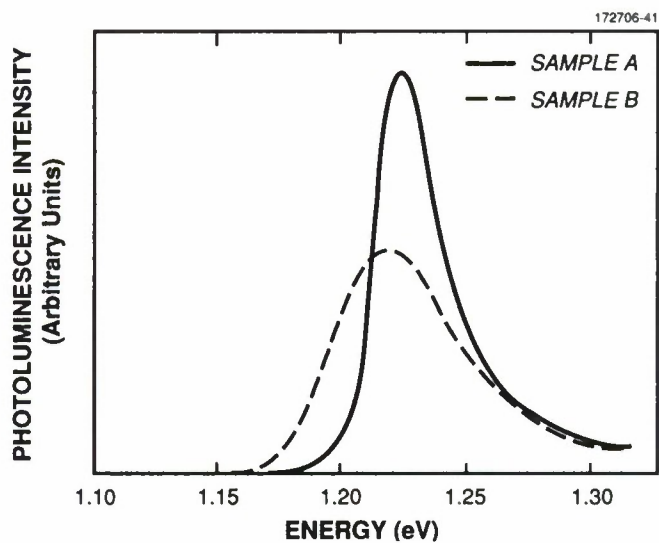


Figure 3-15. Room-temperature PL spectra for test-structure samples A and B.

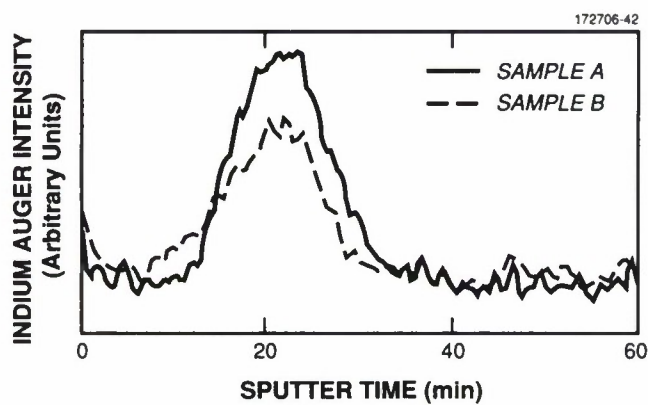


Figure 3-16. Depth profiles of In concentration, obtained by Auger electron spectroscopy combined with Ar-ion sputtering, for test-structure samples A and B.

The dependence of In concentration on depth below the surface was measured for samples A and B by means of Auger electron spectroscopy in combination with Ar-ion sputtering. The measured depth profiles are shown in Figure 3-16, where the intensity of the In Auger peak is plotted against sputtering time. The profile for sample A is symmetric, while the profile for sample B is broadened at the upper InGaAs/GaAs interface and shows a reduction in In content. This reduction can be attributed to the evaporation of In from the InGaAs layer of sample B during the time when the temperature was being increased prior to the deposition of the upper GaAs layer. For sample A, on the other hand, deposition of the upper GaAs layer immediately after InGaAs growth prevented the loss of In and the associated surface roughening. We conclude that the same mechanism is responsible for the improved performance of the GRINSCH-SQW lasers with an upper GaAs bounding layer.

C. A. Wang	H. K. Choi
M. C. Finn	P. M. Nitishin
G. W. Turner	J. W. Chludzinski

REFERENCES

1. F. D. Shepherd and A. C. Yang, *Int. Electron Devices Mtg. Tech. Dig.* (IEEE, New York, 1973), p. 310.
2. E. T. Nelson, K. Y. Wong, S. Yoshizumi, D. Rockafellow, W. DesJardin, M. Elzinga, J. P. Lavine, T. J. Tredwell, R. P. Khosla, P. Sorlie, B. Howe, S. Brickman, and S. Reformat, *Proc. SPIE* **1308**, 36 (1990).
3. B-Y. Tsaur, M. J. McNutt, R. A. Bredthauer, and R. B. Mattson, *IEEE Electron Device Lett.* **10**, 361 (1989).
4. F. D. Shepherd, V. E. Vickers, and A. C. Yang, U.S. Patent No. 3,603,847, June 11, 1969.
5. T. L. Lin and J. Maserjian, *Appl. Phys. Lett.* **57**, 422 (1990).
6. B-Y. Tsaur, M. M. Weeks, R. Trubiano, and P. W. Pellegrini, *IEEE Electron Device Lett.* **9**, 650 (1988).
7. W. F. Kosonocky, F. V. Shallcross, T. S. Villani, and J. V. Groppe, *IEEE Trans. Electron Devices* **ED-32**, 1564 (1985).
8. S. M. Sze, *Physics of Semiconductor Devices*, 2nd ed. (Wiley, New York, 1981), Chap. 5.
9. H. Hara and Y. Nishi, *J. Phys. Soc. Jpn.* **21**, 1222 (1966).
10. J. E. Carnes and W. F. Kosonocky, *Appl. Phys. Lett.* **20**, 261 (1972).
11. A. E. Bochkarev, L. M. Dolginov, A. E. Drakin, P. G. Eliseev, and B. N. Sverdlov, *Sov. J. Quantum Electron.* **18**, 1362 (1988).
12. A. N. Baranov, T. N. Danilova, B. E. Dzhurtanov, A. N. Imenkov, S. G. Konnikov, A. M. Litvak, V. E. Usanskii, and Yu. P. Yakovlev, *Sov. Tech. Phys. Lett.* **14**, 727 (1988).

13. Solid State Research Report, Lincoln Laboratory, MIT, 1989:4, p. 38; S. J. Eglash and H. K. Choi, *Appl. Phys. Lett.* **57**, 1292 (1990).
14. H. K. Choi and S. J. Eglash, to be published in *IEEE J. Quantum Electron.*
15. S. J. Eglash, H. K. Choi, and G. W. Turner, to be published in *J. Cryst. Growth.*
16. J. L. Zyskind, J. C. DeWinter, C. A. Burrus, J. C. Centanni, and M. A. Pollack, *Electron. Lett.* **25**, 568 (1989).
17. R. M. Kolbas, N. G. Anderson, W. D. Laidig, Y. Sun, Y. C. Lo, K. Y. Hsieh, and Y. J. Yang, *IEEE J. Quantum Electron.* **24**, 1605 (1988).
18. D. Fekete, K. T. Chan, J. M. Ballantyne, and L. F. Eastman, *Appl. Phys. Lett.* **49**, 1659 (1986).
19. W. Stutius, P. Gavrilovic, J. E. Williams, K. Meehan, and J. H. Zarrabi, *Electron. Lett.* **24**, 1493 (1988).
20. P. K. York, K. J. Beernink, G. E. Fernandez, and J. J. Coleman, *Appl. Phys. Lett.* **54**, 499 (1989).
21. H. K. Choi and C. A. Wang, *Appl. Phys. Lett.* **57**, 321 (1990); C. A. Wang and H. K. Choi, to be published in *IEEE J. Quantum Electron.*, March 1991.
22. S. D. Offsey, W. J. Schaff, P. J. Tasker, H. Ennen, and L. F. Eastman, *Appl. Phys. Lett.* **54**, 2527 (1989).
23. A. Larsson, J. Cody, and R. J. Lang, *Appl. Phys. Lett.* **55**, 2268 (1989).
24. C. A. Wang, S. Patnaik, J. W. Caunt, and R. A. Brown, *J. Cryst. Growth* **93**, 228 (1988).

4. SUBMICROMETER TECHNOLOGY

4.1 LARGE-AREA MOSAIC DIAMOND FILMS APPROACHING SINGLE-CRYSTAL QUALITY

Despite diamond's excellent electrical properties [1], the inability to obtain large-area single-crystal diamond films has limited the development of diamond device technology. Several attempts to obtain such films by heteroepitaxy have been unsuccessful, and only recently has heteroepitaxy over very limited areas of $< 10^{-4} \text{ cm}^2$ been reported. Hirabayashi et al. [2] used lithographic techniques to control diamond nucleation and growth, but these methods produced only polycrystalline films. In this report, we discuss a lithography-based technique that produces arbitrarily large area mosaic films that approach single-crystal quality. These films are grown from oriented single-crystal seeds $\sim 100 \mu\text{m}$ in size that deviate from the average crystal orientation by a few degrees or less. This deviation results in low-angle grain boundaries, yet for many electrical properties the films are believed to be equivalent to single-crystal diamond films.

The films are produced by first etching relief structures into a Si substrate. The structures match the characteristic shape of macroscopic (111)-faceted diamond seed crystals. The seed crystals are then deposited from a fluid medium or slurry and become fixed and oriented in the etched structures. Subsequent growth of the diamond seed crystals using chemical vapor deposition leads to coalescence and, eventually, a continuous film. This approach of forcing microcrystals to settle out from a fluid medium onto a relief pattern corresponding to the external shape of the microcrystal is called artificial epitaxy, or diataxy, and was first described by Sheftal [3]. It differs from the approach of Filby and Nielsen [4], who proposed relief-structure-induced oriented nucleation, a process in which relief structures are used to induce recrystallization or preferential growth [5]. The latter approach, which can be applied to a wide range of materials, including liquid crystals, and which is generally referred to as graphoepitaxy, does not utilize faceted crystals.

In the technique described here, Si substrates with (100) orientation are patterned and etched to form either a (111)-faceted sawtooth-profile grating or a square array of inverted pyramidal pits that match commercially available (111)-faceted diamond seeds. Patterning is accomplished by first growing a 100-nm-thick thermal SiO_2 film on the Si substrate. The SiO_2 is then patterned using standard photolithographic and etching techniques to form either a grating, with its axis aligned to the $\langle 110 \rangle$ in-plane direction of the substrate, or a square array of similarly oriented regularly spaced square openings ($90 \mu\text{m}$ on a side) on 100- or 200- μm centers. With the SiO_2 as a mask, the Si substrate is then immersed in a water solution of 10% $(\text{CH}_3)_4\text{NOH}$ at 90°C . This solution is very selective, etching the Si (100) planes at least 1000 times faster than the (111) planes. After the etching is completed, the SiO_2 is removed in a HF solution. This procedure results in a substrate whose surface consists primarily of intersecting (111) planes.

The faceted diamond seeds, which are produced by a high-pressure process, are obtained from General Electric or De Beers. The seeds measure 75 to $100 \mu\text{m}$ in diameter and are faceted on (111) planes. They are cleaned by immersion in NaNO_3 at 350 to 400°C for 10 min and in a concentrated solution of HF and HNO_3 for 10 min, and are then rinsed in deionized water and acetone and dried. The diamonds are deposited on the substrates from a slurry of seeds in a 0.01% solution of a novolac polymer and a cellosolve solvent. The addition of a polymer glues the seeds in the etched structures and prevents their falling out during later processing. Following the seeding, the liquid carrier is removed from the substrate by heating.

The crystal orientation depends upon the patterning of the substrate. For the (111)-faceted seeds used in these experiments, a (111) texture is obtained on smooth surfaces and a (100) texture on patterned substrates. The degree of texturing can be determined from the distribution of the $\langle 100 \rangle$ crystal axes of the seeds about the $\langle 100 \rangle$ axis of the Si substrate, as shown in Figure 4-1. The half-width at half-maximum (HWHM) of the distribution is defined as the tip angle. Tip angles are between 0.2 and 0.8° for substrates patterned with etched pyramidal pits and between 1 and 5° for grating-patterned substrates.

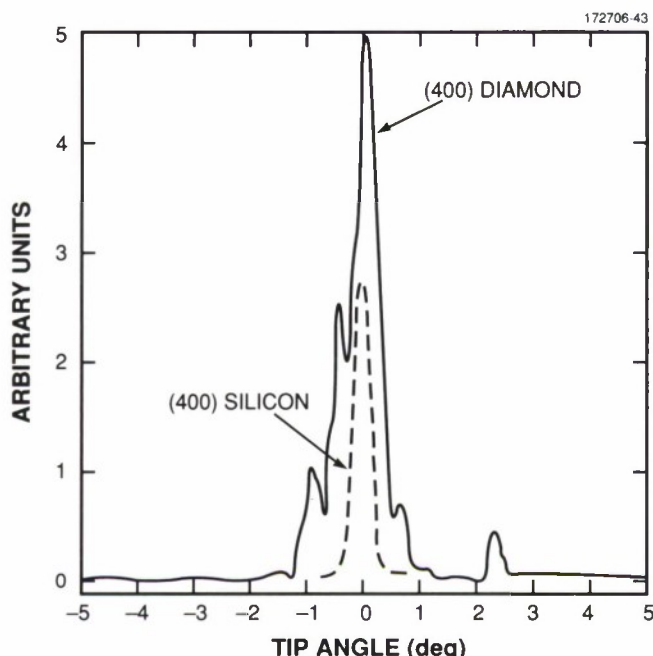


Figure 4-1. X-ray diffraction from the (400) plane of diamond seeds on a pit-patterned Si substrate as a function of the angle between the $\langle 400 \rangle$ axis of the Si substrate and the axis bisecting the primary and diffracted x-ray beams. The tip angle (HWHM) of the diamond seeds is $\sim 0.35^\circ$. The x-ray diffraction from the Si substrate is intended to show the resolution of the system and is not to scale.

The average in-plane orientation of the seeds was also determined by x-ray diffraction. The $\langle 100 \rangle$ axis of the Si substrate was tipped 24.2° from the plane formed by the incoming and diffracted x-ray beams to obtain diffraction from the (311) of diamond planes. In-plane angular distribution was then obtained by plotting the x-ray diffraction intensity as a function of rotation angle about the Si $\langle 100 \rangle$ axis, as shown in Figure 4-2. The spread angle, which is the HWHM of the x-ray intensity from the (311) planes, varies from 0.8 to 5° for substrates with etched pyramidal pits and is larger for grating-patterned substrates.

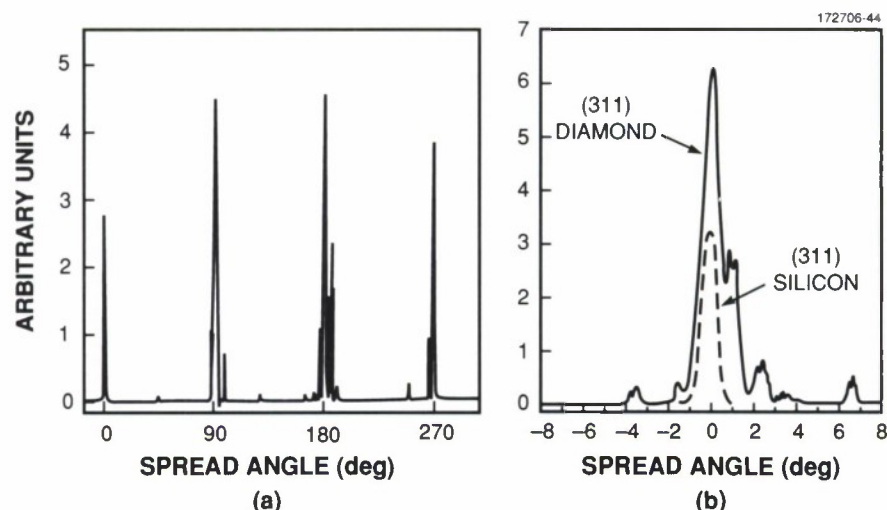


Figure 4-2. (a) X-ray diffraction from the $\{311\}$ planes of diamond on a seeded substrate as a function of rotation in the substrate plane. (b) Expanded view of the x-ray diffraction intensity centered about 270° . The x-ray diffraction from a (311) Si plane is superimposed.

From inspection, the compliance, or percentage of etched-pit structures containing properly oriented diamond seeds, is from 60 to 98%. The compliance depends upon the seed facet smoothness, the dimensions of the patterned structures, and the seeding technique. The best results are achieved with etched pits that are just large enough for the top of an embedded seed to be level with the top of the pit. After seeding, larger pits often contain more than one seed while smaller pits may be empty. Gentle agitation of the seeds on the substrate can improve compliance, but this technique is not yet established.

To grow a continuous diamond film, the seeded substrates are heated to 350°C before chemical vapor deposition to evaporate and carbonize any remaining organic material trapped behind the seeds in the pits. The samples are then cleaned in an O_2 plasma to minimize undesirable seeding from submicrometer-diameter crystals between the larger, oriented seeds. Figure 4-3 shows scanning electron micrographs of samples before and after hot-filament [6], coalescing epitaxial overgrowth. The seeds coalesce over the randomly oriented microcrystals between the oriented seeds until only the oriented seeds are visible.

In summary, we have developed a simple technique to orient faceted single-crystal diamond seeds on substrates. These seeds can be used as the starting material for epitaxial diamond growth to form large-area, continuous mosaic diamond films with crystallographic properties approaching those of single-crystal diamond. Although this technique uses relief structures etched in a single-crystal Si substrate, any substrate in which structures with similar orientation can be formed could be used to orient diamond seeds for subsequent overgrowth. The low-angle grain boundaries found in the films described here are often no worse than those present in so-called single-crystal, natural diamond substrates. We believe that such boundaries will

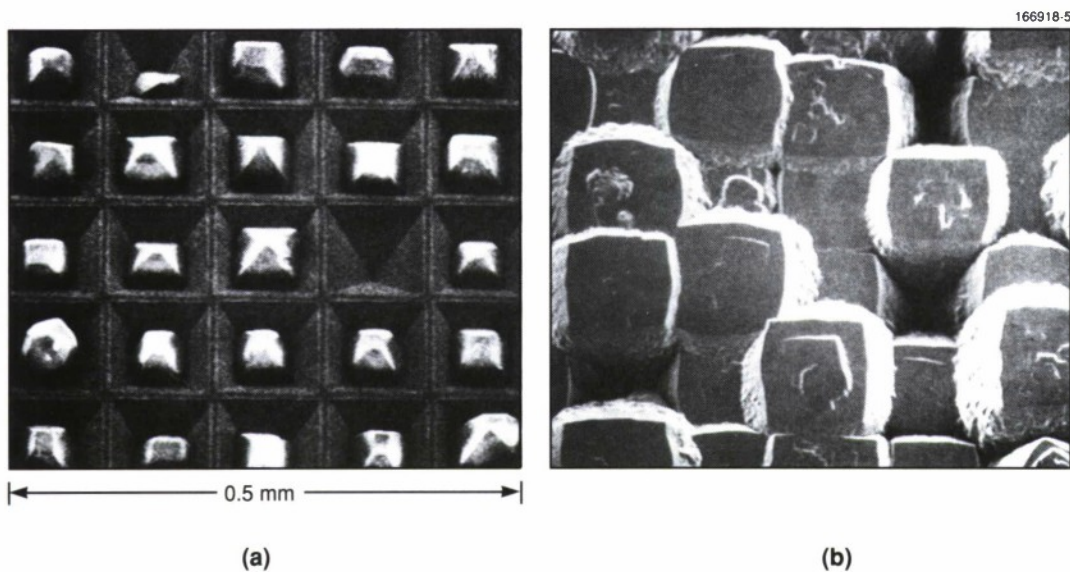


Figure 4-3. Scanning electron micrographs of (a) a diamond-seeded Si substrate having an array of pyramidal pits with one unseeded pit in the second column from the right, and (b) a similar sample after epitaxial diamond overgrowth to $\sim 240 \mu\text{m}$ (80 h), where the effect of missing seeds can be seen as holes in the film. The micrographs are to the same scale.

not affect the electrical properties of majority carrier devices, since similar boundaries in Si films do not affect majority carrier devices. The crystalline quality of these diamond films is expected to improve with more uniformly shaped, smoother-faceted diamond seeds and with growth techniques better suited for coalescent growth.

M. W. Geis
H. I. Smith*

4.2 SILYLATION OF RESISTS EXPOSED BY FOCUSED ION BEAMS

The use of silylation processes has extended the resolution of optical lithography beyond that attainable with conventional resist processing [7],[8]. Since the resist need not be exposed through the entire thickness the problems of reflectivity are reduced, and a shallower depth of focus can be tolerated. In a silylation process, silicon is incorporated into either the exposed or unexposed regions. The pattern is then developed by oxygen plasma etching rather than by a liquid solvent. For silylation processing of novolac/diazoquinone photoresists at typical exposure wavelengths (436 and 365 nm), thermal crosslinking of the unexposed resist is used to

* MIT Department of Electrical Engineering and Computer Science.

generate diffusion selectivity [9]. This results in negative-tone imaging after plasma development. To achieve positive-tone imaging, resists have been developed that crosslink upon exposure, in which case the silicon diffuses more readily into the unexposed areas [10],[11]. These materials have been developed for 248-nm and electron-beam lithography but find application in 193-nm lithography as well [12].

Ion-beam lithography has generally relied upon poly(methyl methacrylate) (PMMA) as a resist, although novolac/diazoquinone materials have also been used [13]. These are generally solvent developed after exposure, so the ion species and energy must be chosen to expose the resist through the entire film thickness to ensure complete development. Thus, Be ions [13],[14] at 260 and 280 keV have been used, as well as H and He ions [15],[16], and heavier ions such as Si and Ga have been employed with very thin resists [17],[18]. In addition, penetration of the ions into the substrate may be an undesirable side effect. We report here a novel process of silylating resists exposed using focused ion beams (FIB), where exposure may be confined to the upper 100 nm of the resist.

The process for silylation of FIB-exposed resists is shown schematically in Figure 4-4. Exposure of the resist by the ion beam results in crosslinking, which hinders the diffusion of the silicon-containing reagent during the silylation. Development in an oxygen reactive ion etching (RIE) plasma selectively removes the crosslinked areas, which have no silicon, resulting in a positive-tone image.

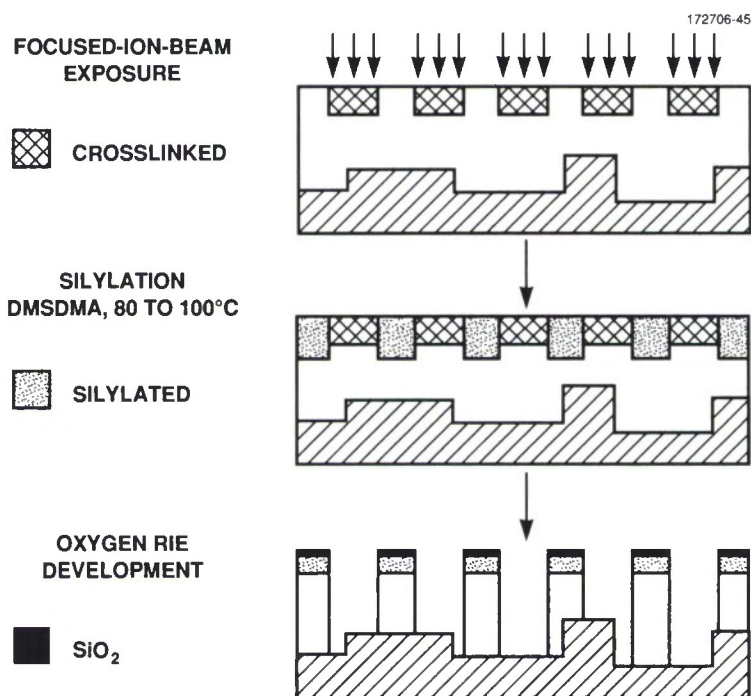


Figure 4-4. Schematic representation of the process for silylation of FIB-exposed resists.

In our experiments, a novolac-based resist (SAL 601) was used, which contains a photoacid generator and a crosslinking reagent. Exposure to radiation produces an acid that catalytically crosslinks the resist, leading to very high sensitivities. This resist generally relies upon postexposure baking in the range from 110 to 170°C, which triggers the crosslinking reaction [19]. For the results reported here, a postexposure baking step was not used.

The exposures were performed in a FIB system with a maximum accelerating voltage of 150 kV using either a Be/Si/Au alloy or a Ga liquid-metal ion source. The pattern used consisted of $50 \times 50\text{-}\mu\text{m}$ squares and fine lines and was exposed at doses incremented between 1×10^{12} and 1×10^{14} ions/cm². Acceleration voltages between 40 and 120 kV were used, and mass/energy selection from the alloy source permitted doubly ionized or dimer species. Thus, ion energies between 20 and 240 keV were available. The silylation was carried out in a heated chamber by exposure to 10 Torr of dimethylsilyldimethylamine (DMSDMA) at 80°C for 1 min. The development was performed in a parallel-plate oxygen RIE plasma at a pressure of 10 mTorr and a dc bias of -200 V. Unsilylated resist etched at 40 to 50 nm/min under these conditions.

Table 4-1 summarizes the sensitivity found for the resist across the range of ion species and energies. Sensitivity is defined as the dose required to prevent silylation (and thus permit reactive ion etching) in a patterned area consisting of a $50 \times 50\text{-}\mu\text{m}$ square. While $1\text{-}\mu\text{m}$ lines could be patterned at the same doses, slightly higher doses were required to print $0.25\text{-}\mu\text{m}$ lines. For example, exposure with 240-keV Si⁺⁺ required a dose of 9×10^{12} ions/cm² for the large square and $1\text{-}\mu\text{m}$ features, while a dose of 3×10^{13} ions/cm² was needed to print the $0.25\text{-}\mu\text{m}$ lines. This well-known effect results from the cumulative dose from the tail of the ion-beam profile for large areas.

TABLE 4-1
Sensitivity of SAL 601 Resist for a Range of Ion Species

Beam Voltage (keV)	Dosage (ions/cm ²)			
	Be	Si	Ga	Au
50	—	—	4×10^{12}	—
80	—	4×10^{12}	5×10^{12}	3×10^{12}
100	8×10^{12}	5×10^{12}	—	2×10^{12}
120	—	7×10^{12}	5×10^{12}	2×10^{12}
240	2×10^{13}	9×10^{12}	—	3×10^{12}

As expected, the sensitivity improved as heavier ions or lower energies were used, resulting in a greater energy deposition density. The energy dependence seemed stronger for the lighter ions, while essentially no difference was seen for Au ions. Previous results using SAL 601 exposed by FIB with 260-keV

Be ions for solvent-based development have shown even higher sensitivity than our studies with Be ions; a dose of 2×10^{12} ions/cm² with postexposure baking at 105°C for 7 min has been reported [13]. The increased sensitivity can be attributed to the postexposure baking process. Figure 4-5 shows a scanning electron micrograph of 80- and 100-nm lines patterned in the resist using 240-keV Be⁺⁺ at a dose of 8 and 9×10^{13} ions/cm², respectively. This is near the resolution limit of the exposure tool, which has printed 50-nm lines in thin PMMA [14].

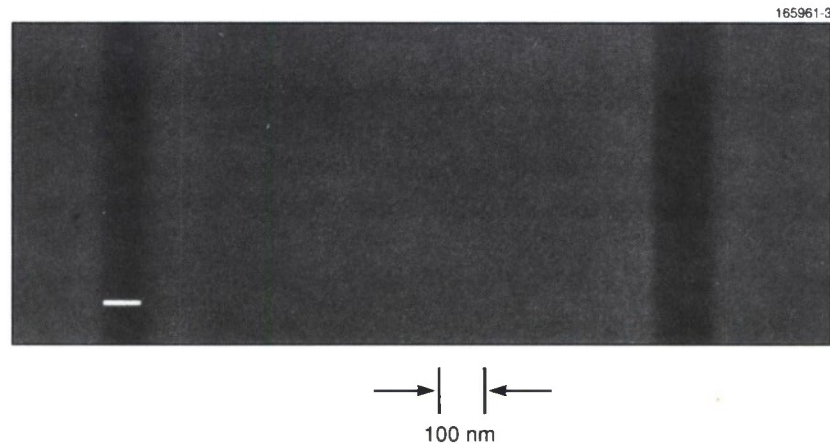


Figure 4-5. Scanning electron micrograph of 80- and 100-nm lines patterned in SAL 601 with a single beam pass of 240-keV Be⁺⁺ at a dose of 8 and 9×10^{13} ions/cm², respectively. Silylation was carried out at 100°C for this sample.

When conventional wet-developed resist is FIB exposed no proximity effect is observed [13], while in electron-beam lithography the proximity effect is a well-known impediment. The proximity effect with electron beams appears to be even more severe with a silylation process than with conventional processing [20]. This is attributed to the catalytic nature of the crosslinking of the resist, which results from the absence of the mitigating effect of nonlinearity (high contrast) that occurs with conventional resists. The lack of the proximity effect for the silylated acid-catalyzed resist exposed with a dose of 4×10^{13} ions/cm² using 240-keV Be⁺⁺ is evident in Figure 4-6. Minimal linewidth change is seen between the section in which the line is isolated ($0.5 \mu\text{m}$ wide) and the section in which it is written between two $5 \times 5\text{-}\mu\text{m}$ pads spaced $0.3 \mu\text{m}$ to either side.

Processes using FIB exposure systems have generally been perceived as slow relative to electron-beam processes. Direct processing often requires doses in the 10^{14} -ions/cm² range, and while FIB lithography can exhibit sensitivities in the 10^{12} -ions/cm² range, the low-mass sources required for complete penetration of the resist do not exhibit the brightness of alternative sources such as Ga. The silylation process described here is well suited for such a high-mass source, and it can take advantage of the increased current density without resorting to a thin imaging resist as part of a multilayer process.

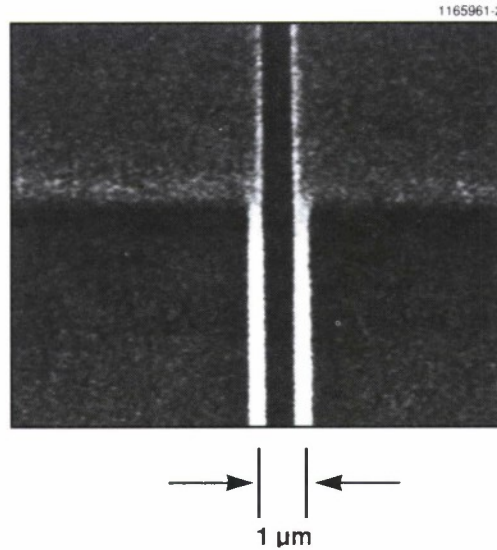


Figure 4-6. Scanning electron micrograph of a 0.5- μm line patterned in SAL 601 using 240-keV Be^{++} at a dose of 4×10^{13} ions/ cm^2 . The pattern changes from an isolated line to one separated from $5 \times 5\text{-}\mu\text{m}$ exposed areas by 0.3 μm on either side.

Table 4-2 compares the writing times for the FIB silylation process to the times for both electron beams and ion beams in conventional resists. The results for electron beams were obtained with a field emission system, which yields the highest available current density [21]. Actual experimental conditions are given, except as indicated. Although the beam currents in the table are those used to write fine features, the sensitivity values are for large areas. (As described earlier, single lines often require a larger dose, but this is hard to specify per unit area.) Since low-energy Ga^+ ions can be used for the silylation process, high current densities are available. Thus, the projected writing time per unit area for the FIB silylation process is a factor of 5 lower than previous FIB results and a factor of 2.5 lower than the fastest projected writing time for electron beams.

In summary, a silylation process has been developed for FIB-exposed resists. This approach eliminates the requirement for exposure completely through the resist film, and it can simplify multilayer processes and take advantage of alternative, brighter FIB sources. A wide selection of ion species and energies has been successfully used, from 280-keV Be ions with a range $> 1 \mu\text{m}$ to 20-keV Au ions with a range $< 50 \text{ nm}$. Resolution has been obtained below 100 nm, and diffusion of silicon is not perceived as a limitation for resolution. The lack of a proximity effect has also been demonstrated for this process. Thus, FIB patterning with silylation presents an attractive alternative to electron-beam lithography for x-ray mask making and direct writing on a wafer.

M. A. Hartney
D. C. Shaver
M. I. Shepard

J. S. Huh
J. Melngailis

TABLE 4-2
Comparison of Observed and Projected Electron-Beam and Ion-Beam Writing Times

	Sensitivity	Beam Current	Minimum Feature Size (μm)	Writing Time over Large Area (s/mm^2)
Electron beam*				
Novolac	$25 \mu\text{C/cm}^2$	$0.78 \rightarrow 3.0 \text{ nA}^\dagger$	0.1	$320 \rightarrow 83$
PMMA	$150 \mu\text{C/cm}^2$	1.17 nA	0.075	1300
Ion beam				
Novolac [13] SAL 601 (negative)	$10^{12} \text{ ions/cm}^2$ (Be^{++} , 260 keV)	20 pA †	0.1	170
PMMA [14]	$10^{13} \text{ ions/cm}^2$ (Be^{++} , 280 keV)	20 pA	0.05	1700
Silylation SAL 601 (positive)	$10^{13} \text{ ions/cm}^2$ (Be^{++} , 280 keV)	20 pA	0.08	1700
Silylation SAL 601 (positive)	$4 \times 10^{12} \text{ ions/cm}^2$ (Ga^+ , 49 keV)	200 pA [22] †	0.1 †	33

*25-kV field emission [21].

† Projected.

REFERENCES

1. M. W. Geis, N. N. Efremow, and D. D. Rathman, *J. Vac. Sci. Technol. A* **6**, 1953 (1988).
2. K. Hirabayashi, Y. Taniguchi, O. Takamatsu, T. Ikeda, K. Ikoma, and N. I. Kurihara, *Appl. Phys. Lett.* **53**, 1815 (1988).
3. N. N. Sheftal, in *Growth of Crystals*, Vol. 10, edited by N. N. Sheftal (Consultants Bureau, New York, 1976).
4. J. D. Filby and S. Nielsen, *Brit. J. Appl. Phys.* **18**, 1357 (1967).
5. H. I. Smith, M. W. Geis, C. V. Thompson, and H. A. Atwater, *J. Cryst. Growth* **63**, 527 (1983).
6. M. W. Geis, *Proc. Diamond, SiC and Related Wide Bandgap Semiconductors*, Vol. 62 (Materials Research Society, Pittsburgh, PA, 1990), p. 15.
7. C. M. Garza, G. R. Misium, R. R. Doering, B. Roland, and R. Lombaerts, *Proc. SPIE* **1086**, 229 (1989).

8. F. Vinet, M. Chevallier, J. C. Guibert, and C. Pierrat, *Proc. SPIE* **1086**, 433 (1989).
9. B. Roland, J. Vandendriessche, R. Lombaerts, B. Denturck, and C. Jakus, *Proc. SPIE* **920**, 120 (1988).
10. J. P. W. Schellekens and R. J. Visser, *Proc. SPIE* **1086**, 220 (1989).
11. J. W. Thackeray, J. F. Bohland, E. K. Pavelchek, G. W. Orsula, A. W. McCullough, S. K. Jones, and S. M. Bobbio, *Proc. SPIE* **1185**, 2 (1990).
12. M. A. Hartney, R. R. Kunz, D. J. Ehrlich, and D. C. Shaver, *Proc. SPIE* **1262**, 119 (1990).
13. S. Matsui, Y. Kojima, and Y. Ochiai, *Appl. Phys. Lett.* **53**, 868 (1988).
14. W. Chu, A. Yen, K. Ismail, M. I. Shepard, H. J. Lezec, C. R. Musil, J. Melngailis, Y-C. Ku, J. M. Carter, and H. I. Smith, *J. Vac. Sci. Technol. B* **7**, 1583 (1989).
15. H. Ryssel, H. Kranz, K. Habberger, and J. Bosch, in *Microcircuit Engineering*, edited by R. P. Kramer (Delft University, Delft, Holland, 1981), p. 293.
16. M. Komuro, N. Atoda, and H. Kawakatsu, *J. Electrochem. Soc.* **126**, 483 (1979).
17. S. Matsui, K. Mori, T. Shiokawa, K. Toyoda, and S. Namba, *J. Vac. Sci. Technol. B* **5**, 853 (1987).
18. R. L. Kubena, F. P. Stratton, J. W. Ward, G. M. Atkinson, and R. J. Joyce, *J. Vac. Sci. Technol. B* **7**, 1798 (1989).
19. W. E. Feely, J. C. Imhof, and C. M. Stein, *Polym. Eng. Sci.* **26**, 1101 (1986).
20. T. G. Vachette, P. J. Paniez, F. Lalanne, and M. Madore, to be published in *Microcircuit Engineering '90* (Elsevier, Amsterdam).
21. M. A. Gesley, F. J. Hohn, R. G. Viswanathan, and A. D. Wilson, *J. Vac. Sci. Technol. B* **6**, 2014 (1988).
22. P. Heard, Rutherford Appleton Laboratory, Chilcot, England, private communication.

5. HIGH SPEED ELECTRONICS

5.1 GaAs MISFET WITH A LOW-TEMPERATURE-GROWN EPITAXIAL LAYER AS THE INSULATOR

A high-resistivity GaAs epitaxial layer grown by molecular beam epitaxy at low temperature has been utilized as the buffer layer in a metal-semiconductor field-effect transistor (MESFET) to reduce sidegating [1]. Such layers are grown at a substrate temperature of 200°C, which is significantly lower than the 580°C typically used to grow high-quality GaAs. Recently, a low-temperature (LT) GaAs layer has been used as the insulating gate in a GaAs metal-insulator-semiconductor FET (MISFET). Compared with a MESFET, a MISFET has a higher gate breakdown voltage and lower forward-bias gate current, which result in a greater power handling capability. Our MISFETs made with the LT GaAs layer have demonstrated the highest power density reported to date for GaAs-based FETs.

The epitaxial layer structure of the GaAs MISFET is shown in Figure 5-1. All layers were grown at 580°C, except for the buffer layer and the gate insulating layer, which were grown at 200°C. The device was fabricated with our standard MESFET process. Ohmic contacts were formed by etching through the top LT GaAs and AlAs layers and then depositing Ni/Ge/Au contact pads directly on the conducting *n*-GaAs layer. Ti/Au was used for the gate metallization and was deposited on the top LT GaAs layer without a gate recess. The gate length, drain-source spacing, and gate width are 1.5, 6, and 600 μm , respectively. Proton implantation was used to isolate the devices, and the substrate was thinned to 175 μm to achieve reasonable heat sinking.

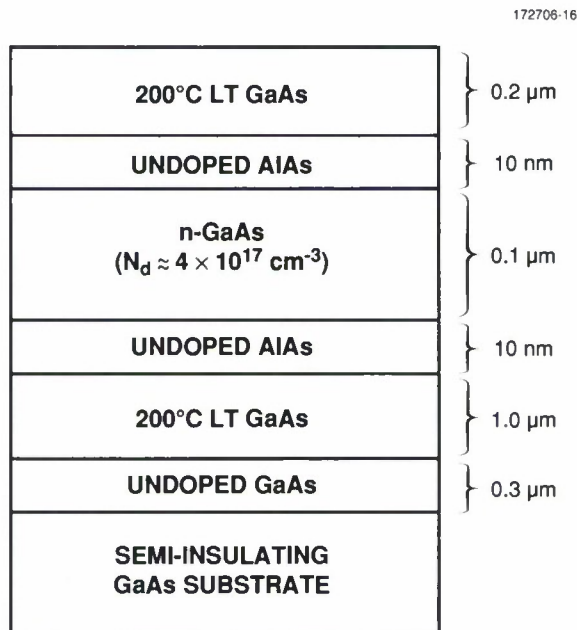


Figure 5-1. Schematic cross section of the epitaxial layer structure of the GaAs MISFET.

Typical dc current-voltage (I-V) characteristics of the GaAs power MISFET are shown in Figure 5-2. The transconductance g_m is ~ 120 mS/mm of gate width, and the maximum density of the drain-source current I_{DS} reaches 750 mA/mm at a drain-source voltage V_{DS} of 4 V and a gate-source voltage V_{GS} of 2 V. This density is about a factor of 2 higher than is typically used in GaAs power MESFETs. The gate reverse-breakdown voltage of the MISFET is 42 V, which is much higher than the ~ 15 V typical for a MESFET. The gate of the MISFET requires a forward bias of 9.3 V to reach the 1-mA/mm gate current seen at 0.6 V in a conventional MESFET. Therefore, the LT GaAs MISFET has a much greater resistance to gate burnout, allowing an expanded dynamic range.

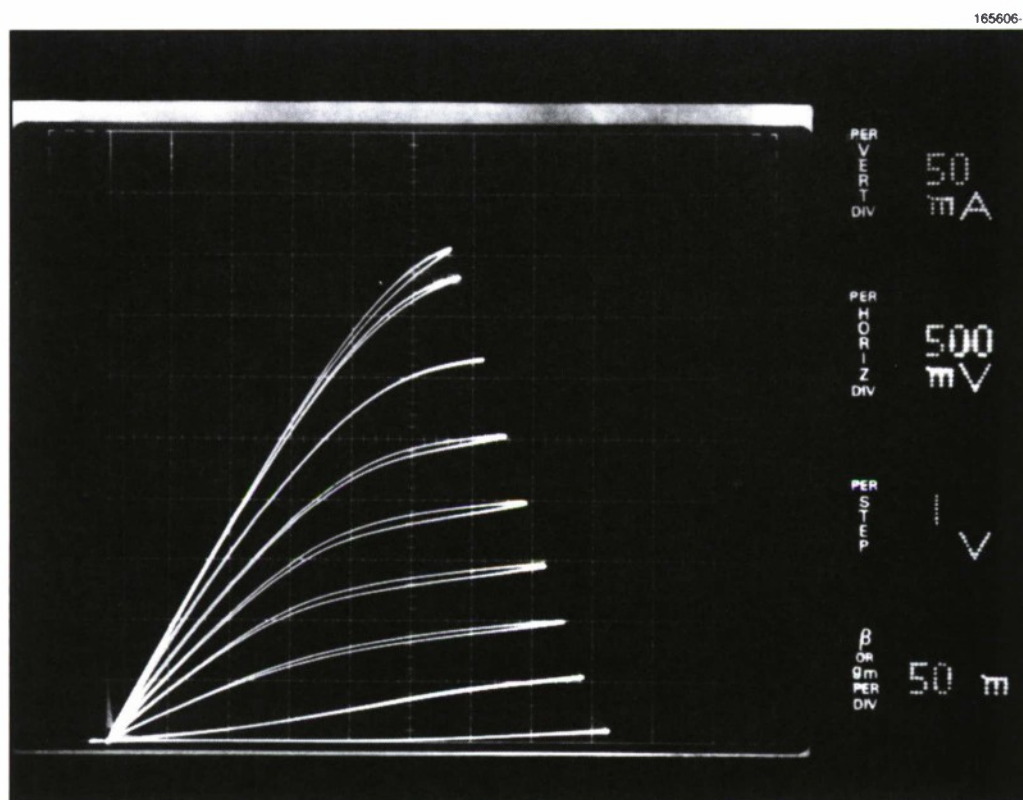


Figure 5-2. I_{DS} - V_{DS} characteristics of a 600- μ m-wide GaAs MISFET. The upper trace is for $V_{GS} = 2$ V.

Typical values of the maximum frequency of oscillation f_{max} and the unity-current-gain frequency f_T for the GaAs MISFET are 14 and 8.5 GHz, respectively. These numbers are comparable to those for a MESFET with similar device dimensions. Continuous-wave power measurements were performed on

600- μm -wide MISFETs at 1.1 GHz. The resulting output power and power-added efficiency as a function of the input power are shown in Figure 5-3. For each drain bias the matching circuits were tuned for maximum output power. At $V_{DS} = 18.5\text{ V}$, the GaAs MISFET delivered a maximum output power of 940 mW (1.57-W/mm power density) with 4.4-dB gain and 27.3% power-added efficiency. This power density exceeds the highest value (1.4 W/mm) previously reported for GaAs-based FETs [2]. The highest power-added efficiency for the MISFET was 31.4% with 6.1-dB gain, measured at an input power of 194 mW.

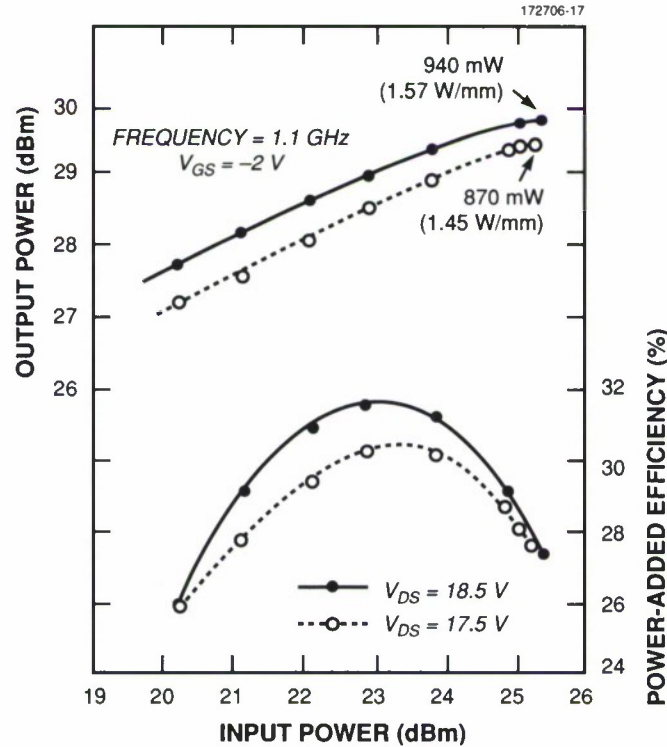


Figure 5-3. Measured output power and power-added efficiency vs input power for a GaAs MISFET.

Preliminary test results on the GaAs MISFET indicate that it could also be an excellent microwave switch. In addition, with their high forward turn-on voltage, GaAs MISFETs used in digital integrated circuits would allow a larger logic swing and noise margin than are found in conventional MESFET circuits.

C. L. Chen	M. J. Manfra
F. W. Smith	B. J. Clifton
L. J. Mahoney	A. R. Calawa

5.2 MAGNETOOPTICAL STUDY OF DONOR LEVEL CROSSING IN TIPPED GaAs/AlGaAs QUANTUM WELLS

Donor level crossing in quantum wells has been investigated using the photoconductivity method in conjunction with far-infrared (FIR) laser sources [3]. To achieve photoconductive detection in GaAs films, an electric field is applied in the plane of the sample, which is held at liquid-He temperatures. Optical excitation of donors is detected as a change in sample conductivity. Employing this method, which is capable of extreme sensitivity in the detection of donor absorption in bulk epitaxial GaAs, we obtained relatively sharp spectral lines with high signal-to-noise ratios in quantum-well samples. This allowed us to explore, with high precision, differences between the spectra of shallow donors in GaAs quantum wells and in bulk GaAs. In particular, we made a critical study of an effect that has not previously been reported, namely, the anticrossing of two p -like levels of donors in the center of a quantum well.

In the limit of an infinitely wide well, the energy levels of a donor in the center of the well must become indistinguishable from those of a bulk donor. Here, we identify the energy levels of the donor in the center of the well by the label we attach to bulk states into which the well state adiabatically evolves as the quantum-well width is slowly increased to infinity, with the donor always remaining in the center of the well. This labeling scheme does not lead to ambiguities for any of the states of interest described below.

Many interesting differences exist between the spectra of hydrogenic donors confined in the center of a one-dimensional quantum well and those of hydrogenic donors in bulk GaAs (the latter behave very nearly like weakly bound hydrogen atoms [4],[5]), and these differences persist even for wells as wide as several donor Bohr radii. For example, the spectra of (isotropic) bulk donors depend only on the strength of the magnetic field, whereas well-donor spectra depend on both the magnitude of the field and the angle θ that it makes with the normal to the plane of the well. Another difference between bulk- and well-donor spectra is that at zero magnetic field the well potential lifts certain degeneracies that exist for a spinless electron in the Coulomb field of a point positive charge in vacuum. States having the same principal hydrogenic quantum number n , but labeled by different values of orbital angular momentum l , are not degenerate for the donor in the well. For example, the $2p$ levels of the well are not degenerate with the $2s$ level. In addition, the quantum-well barriers break the degeneracy of states with the same n and l but different magnitudes of the quantum number M (where M is the projection of the orbital angular momentum on the z -axis). Thus, at zero magnetic field the $2p_0$ level always lies above the degenerate $2p_{+1}$ and $2p_{-1}$ levels in a quantum well, whereas all three levels are degenerate in the simple hydrogenic model.

The splitting of these levels in the well results in a wealth of level crossings that occur as a function of magnetic field strength for $\theta = 0^\circ$. Of special interest is the crossing between the $2p_{+1}$ and $2p_0$ levels. Since M remains a good quantum number in magnetic fields along the z -axis ($\theta = 0^\circ$) and since these levels have different M values, they may cross. However, if the sample is tipped ($\theta \neq 0^\circ$), M is no longer a good quantum number and the levels can no longer cross, resulting in an anticrossing due to the presence of a nonzero component of the field in the plane of the well. This component couples the $2p_{+1}$ and $2p_0$ levels, causing them to “repel” each other.

GaAs/AlGaAs quantum-well samples were grown using elemental-source molecular beam epitaxy. Each sample consisted of a (100)-oriented semi-insulating liquid-encapsulated Czochralski substrate with the following epitaxial layers: an unintentionally doped GaAs buffer layer, an unintentionally doped $\text{Al}_{0.2}\text{Ga}_{0.8}\text{As}$

buffer layer, a 25-period quantum-well structure with 35-nm-thick $\text{Al}_{0.2}\text{Ga}_{0.8}\text{As}$ barriers and center-doped ~ 50 -nm-wide GaAs quantum wells, an unintentionally doped 100-nm-thick $\text{Al}_{0.2}\text{Ga}_{0.8}\text{As}$ isolation layer, and an unintentionally doped 10-nm-thick GaAs cap layer. The center third of the quantum wells was lightly doped ($5 \times 10^{15} \text{ cm}^{-3}$) with silicon donors. Photoluminescence measurements confirmed that the samples were of high quality and lightly doped. The fabrication procedure for forming electrical contacts to the samples consisted of the following steps: beveling a pair of opposite edges of a 6×6 -mm sample to expose the quantum wells; forming contacts by metallization of the edges with layers of Ni, Ge, and Au followed by a lift-off process; alloying the contacts; and attaching 50- μm -thick gold wires to the contacts with conducting epoxy.

The measurements were carried out at about 20 wavelengths from 890 to 70.5 μm using CO_2 -laser-pumped FIR gas lasers. Samples immersed in liquid He were illuminated by white light from an external 20-W tungsten filament lamp in order to free carriers from traps in the AlGaAs prior to the spectroscopy runs. Photoconductivity spectra obtained by sweeping the magnetic field at fixed laser frequency are displayed in Figure 5-4. These measurements were taken in the Faraday configuration ($\theta = 0^\circ$), where the light is incident along the

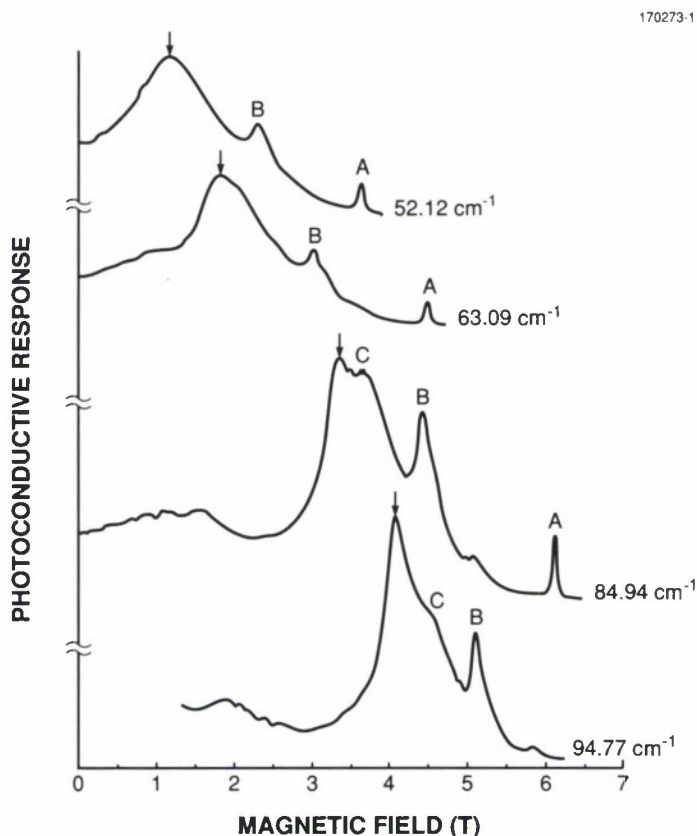


Figure 5-4. Photoconductivity spectra obtained by sweeping the magnetic field at fixed laser frequency. The arrows indicate the $1s \rightarrow 2p_{+1}$ transitions. Other prominent features that appear in the spectra are labeled A, B, and C.

sample normal. A typical field sweep took approximately 3 min. The spectra shown are not averaged, but each spectrum is taken in a single sweep. The arrows indicate the peak of the $1s \rightarrow 2p_{+1}$ transition. Other sharp, prominent features appearing in the spectra, e.g., lines A, B, and C in Figure 5-4, are relatively sensitive to the magnitude and polarity of the bias voltage applied and, to a lesser extent, to the intensity of the laser. We do not at present understand the origin of the extra structure in Figure 5-4.

Figure 5-5 shows a plot of peak positions vs magnetic field for the $1s \rightarrow 2p_{+1}$ transition, which we believe are the most accurate data yet published for any shallow donor transition in a quantum well. Error bars are given only for the four lowest points of the $1s \rightarrow 2p_{+1}$ transition and represent the uncertainty in locating these points in the magnetic field. No vertical error bars are given since the laser-line frequencies are known to better than one part per million. The spectral peak positions corresponding with the dashed line in Figure 5-5 are obtained when the sample is rotated into the Voigt configuration ($\theta = 90^\circ$), where the radiation is deflected by a mirror so that the light remains incident along the sample normal. We have used the Voigt data to establish a working value for L , the width of the GaAs quantum wells. The theoretical curve for the Voigt geometry in Figure 5-5 is for $L = 51$ nm, which is consistent with a measured value of 50 ± 5 nm obtained with a scanning electron microscope.

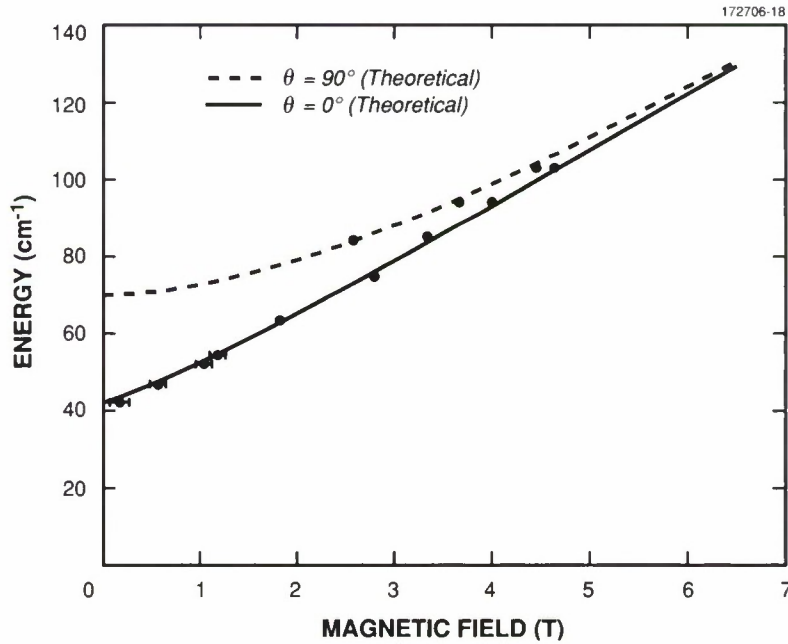


Figure 5-5. Plots of peak positions of the transition energy vs magnetic field for the $1s \rightarrow 2p_{+1}$ transition. The theoretical curves for the Faraday ($\theta = 0^\circ$) and Voigt ($\theta = 90^\circ$) geometries are shown, with the corresponding points representing experimental results.

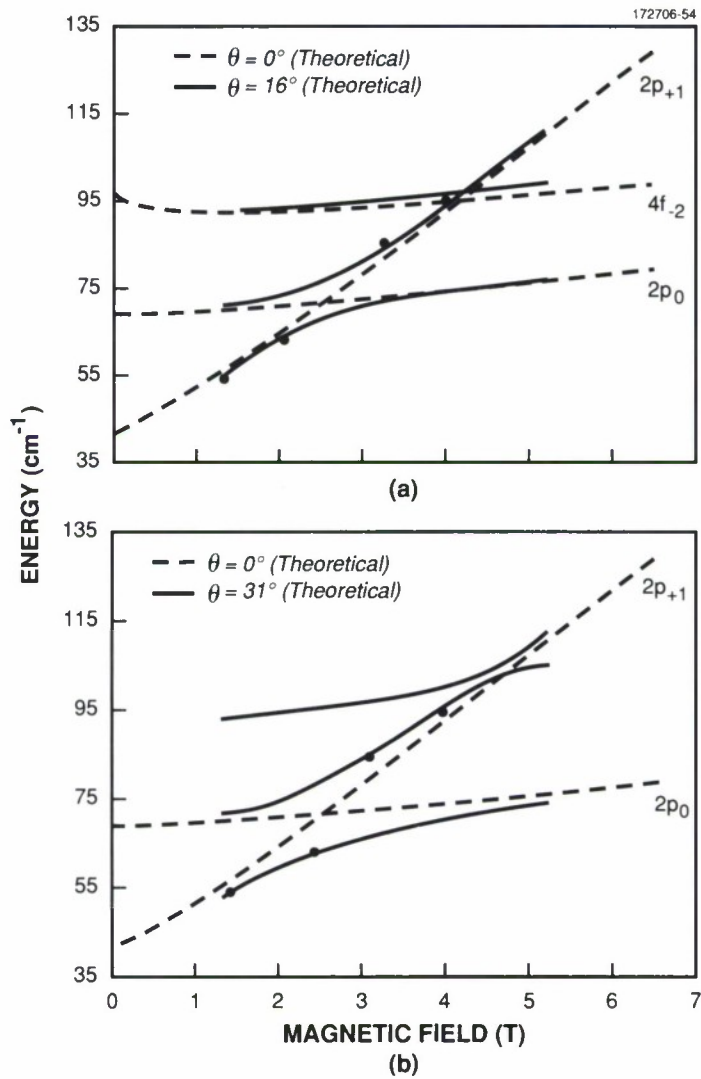


Figure 5-6. (a) Plots of peak positions of the transition energy vs magnetic field, showing the theoretical curves for the Faraday geometry ($\theta = 0^\circ$) and the theoretical curves and experimental points for $\theta = 16^\circ$. (b) Plots of peak positions of the transition energy vs magnetic field, showing the theoretical curves for the Faraday geometry ($\theta = 0^\circ$) and the theoretical curves and experimental points for $\theta = 31^\circ$.

As shown in Figures 5-6(a) and 5-6(b), respectively, the experimental data for $\theta = 16^\circ$ and $\theta = 31^\circ$ agree with our coupled-state theory. In these configurations the radiation propagates along the direction of the magnetic field. The agreement is very satisfactory considering that no adjustable parameters were used in the

theory. (Bulk values of 46.1 cm^{-1} for the donor Rydberg energy and 0.0665 for the ratio of the conduction band mass to the vacuum electron mass were utilized.) This agreement is also strong evidence for the $2p_0$ - $2p_{+1}$ anticrossing.

W. D. Goodhue	D. M. Larsen*
J. W. Bales	J. Waldman*
E. R. Mueller*	

REFERENCES

1. F. W. Smith, A. R. Calawa, C. L. Chen, M. J. Manfra, and L. J. Mahoney, *IEEE Electron Device Lett.* **9**, 77 (1988).
2. H. M. Macksey and F. H. Doerbeck, *IEEE Electron Device Lett.* **EDL-2**, 147 (1981).
3. R. T. Grimes, M. B. Stanaway, J. M. Chamberlain, J. L. Dunn, M. Henini, O. H. Hughes, and G. Hill, *Semicond. Sci. Technol.* **5**, 305 (1990).
4. G. E. Stillman, D. M. Larsen, C. M. Wolfe, and R. C. Brandt, *Solid State Commun.* **9**, 2245 (1971).
5. H. R. Fetterman, D. M. Larsen, G. E. Stillman, P. E. Tannenwald, and J. Waldman, *Phys. Rev. Lett.* **16**, 975 (1971).

* Author not at Lincoln Laboratory.

6. MICROELECTRONICS

6.1 IMPROVEMENTS TO AN ANALOG-SIGNAL-PROCESSING CHAIN FOR A CCD CAMERA

Continued reduction of the noise associated with the on-chip output amplifier of our high-frame-rate charge-coupled device (CCD) imagers has required the redesign of the camera post-signal-processing analog chain. Objectives of the redesign were first to reduce the degradation in the signal-to-noise ratio as the signal was processed through the analog chain and second to minimize the drift associated with the chain.

Block diagrams and schematics of the analog chain before and after redesign, respectively, are shown in Figures 6-1(a) and 6-1(b). The initial design has a buffer-amplifier input, which drives the capacitive load of the wiring and the following preamplifier stage, increases the signal above the noise of the next two stages, and provides a low-pass filter to limit the thermal noise contribution to the signal. The correlated-double-sampler (CDS) stage receives the amplified signal and continues signal conditioning by removing reset and low-frequency $1/f$ noise [1] introduced by the on-chip source-follower output amplifier. Additional signal gain after the CDS amplifies the signal above the remaining circuit noise in the analog chain. The gain stage is followed by a black-level-reference track-and-hold (BLRTH) stage, which generates a zero reference for the image-signal pixels. The analog signal is subsequently digitized by a 12-bit analog-to-digital (A/D) converter.

In the redesigned chain, shown in Figure 6-1(b), the BLRTH stage has been eliminated. Present applications of the CCD camera create a dark reference through software subtraction of an averaged dark background, thus eliminating the need for this stage. In operation, the BLRTH establishes the reference by subtracting a dark-signal-reference pixel from the image-signal pixel. Since both image and dark pixels contain white thermal noise, the subtraction process increases the output to input noise by a factor of $\sqrt{2}$. The dark pixels are sampled and subtracted once per row of image pixels, causing a correlated noise component between pixels in the same row. Bench measurement of the redesigned analog chain confirmed a noise reduction of slightly less than the expected factor of $\sqrt{2}$, from 17 to < 13 noise equivalent electrons at a clock frequency of 4.16×10^6 pixels/s. Removal of the BLRTH stage also reduced the drift of the analog chain output. The drift was caused by the clamp and buffer transistor leakage currents, which slowly discharged the clamp capacitor.

Two further changes were made to the analog chain to stabilize the output and eliminate drift. First, the entire gain of the chain was placed before the CDS. As a result, the CDS now eliminates the slow drift component (both thermal and ac couple related) of the amplifier. The second modification was to the voltage reference of the CDS. The original design used a resistive network to generate a reference voltage that was sensitive to temperature and to the noise of the dc bias line. The resistive network was replaced by a voltage regulator, which is much less sensitive to temperature and bias-line noise. These improvements to the analog chain, along with a change to the packaged part of the CCD, have reduced the drift from as much as 4.3 mV to $< 488 \mu\text{V}$, which is equivalent to 1 least-significant bit of the A/D converter.

W. H. McGonagle
J. C. Twichell
R. K. Reich

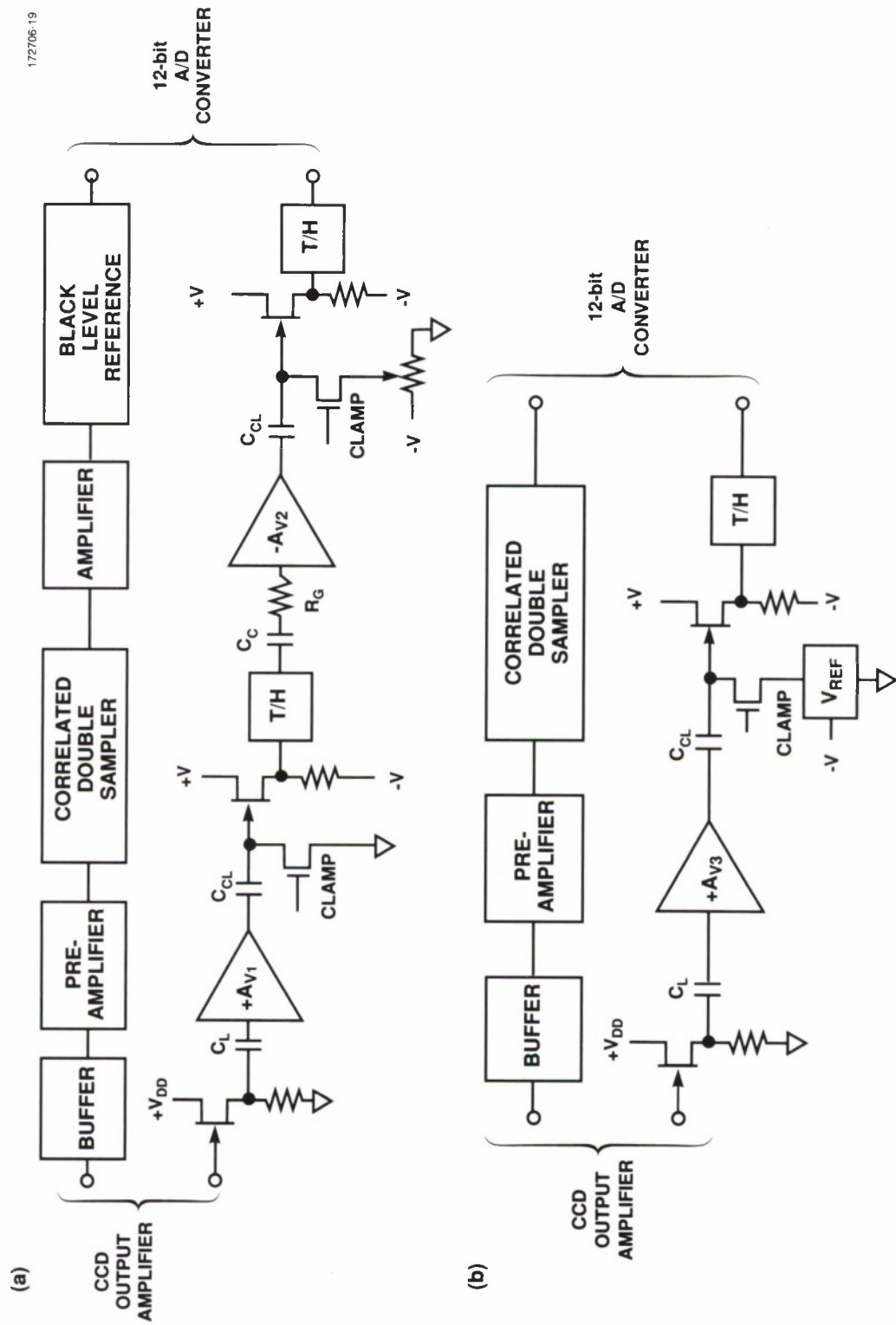


Figure 6-1. Block diagram and schematic of (a) original and (b) redesigned analog-signal-processing chain starting with the CCD output as the analog chain input and ending at the A/D converter at the chain output.

6.2 FABRICATION PROCESS FOR NON-OVERLAPPING-GATE CCDs

One of the key processes in the fabrication of a CCD is the formation of narrow spacing between electrodes to allow the fringing field to efficiently transfer charge between adjacent potential wells. The most common approach to accomplish this has been to use multilayer overlapping polysilicon gate structures. The electrodes on different layers are separated by thermally grown polysilicon oxide, and the spacing between them can be easily kept to $< 0.5 \mu\text{m}$. However, it has been reported that sharp corners on the edges of the electrodes caused by the oxidation of polysilicon in this process can cause local trapping of charge [2]. In addition, the parasitic capacitance of the overlapping electrodes is not desirable for high-speed CCDs.

Several approaches have been employed to produce non-overlapping-gate CCDs with submicrometer spacing in a single level of polysilicon. Nonconventional technologies such as electron-beam lithography and edge-etch processes have been used for the CCD fabrication, resulting in devices with reliable charge-transfer efficiencies [3],[4]. In this report, we describe the fabrication of non-overlapping-gate CCDs utilizing local oxidation of silicon (LOCOS) on the polysilicon layer. The oxide encroachment under the nitride mask in the LOCOS process forms an oxide mask for etching the polysilicon with $0.4\text{-}\mu\text{m}$ spacings, starting from $1.5\text{-}\mu\text{m}$ -wide resist lines defined by a conventional projection aligner.

Figure 6-2 shows the major patterning steps in this non-overlapping-gate process. The polysilicon gate layer is deposited over the gate-oxide- and field-oxide-coated wafer and is then coated with a pad oxide and a deposited nitride layer. A layer of photoresist is applied, exposed with a modest-capability projection aligner to form $1.5\text{-}\mu\text{m}$ -wide lines, and developed. The nitride layer is then etched to yield a wafer cross section, as shown in Figure 6-2(a). Next, oxide is grown on the exposed areas of polysilicon, while nitride protects the underlying polysilicon against oxidation. However, the oxide at the edges of a nitride line will encroach underneath the nitride reducing the $1.5\text{-}\mu\text{m}$ -wide nitride lines to submicrometer spacings between adjacent oxide lines, as shown in Figure 6-2(b). The nitride, the pad oxide and the underlying polysilicon are subsequently etched to form CCD electrodes and interconnects, as is illustrated in Figure 6-2(c). After the polysilicon is patterned, the gaps are filled with low-pressure chemical vapor deposited oxide.

Three-phase, 64×64 -pixel frame-transfer buried-channel CCD imagers with electrode spacings of 0.2 to $1 \mu\text{m}$ have been fabricated using the above-described process. Figure 6-3 is a scanning electron micrograph of a cross section of a finished device, showing the submicrometer spacing between two adjacent CCD electrodes. A top view of an array of CCD polysilicon electrodes and a close-up of the submicrometer spacing are shown in Figure 6-4. Unlike the smoothly tapered LOCOS oxide seen on crystalline silicon, the LOCOS oxide on polysilicon is not uniform at the edges, which accounts for the low yield of devices with electrode spacings $< 0.4 \mu\text{m}$. The measured charge-transfer inefficiency (CTI) ranges from 0.0003 to 0.001 for $0.4\text{-}\mu\text{m}$ electrode spacings and from 0.015 to 0.1 for $0.8\text{-}\mu\text{m}$ spacings. To better understand the relationship between gap size and CTI, we used a two-dimensional numerical simulator to calculate the potential profile by solving Poisson's equation. Figure 6-5 shows the channel potential minimum between two adjacent electrodes separated by 0.4 and $0.8 \mu\text{m}$, respectively. The potential minima seen in the interelectrode region are deeper for the larger-gap devices, qualitatively explaining the undesirable CTI, which is due to charges trapped in the wells.

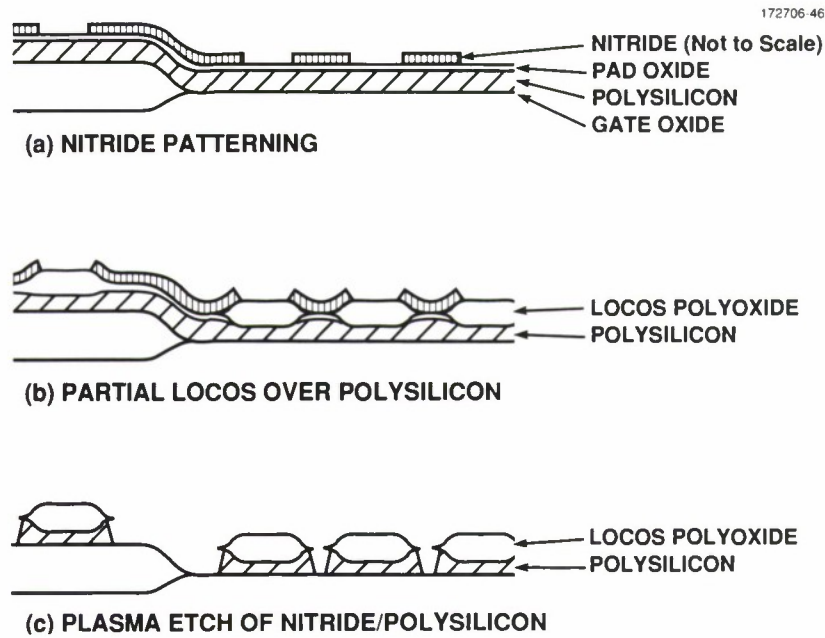


Figure 6-2. Major patterning steps of the non-overlapping-gate CCD process. Shown is a cross section of the wafer (a) after the polysilicon, pad oxide, and nitride deposition, the photoresist definition, and the nitride etch and photoresist strip, (b) after the LOCOS process, demonstrating oxide encroachment under the nitride, and (c) after the etch of the nitride and the etch of the polysilicon using the oxide as a mask.

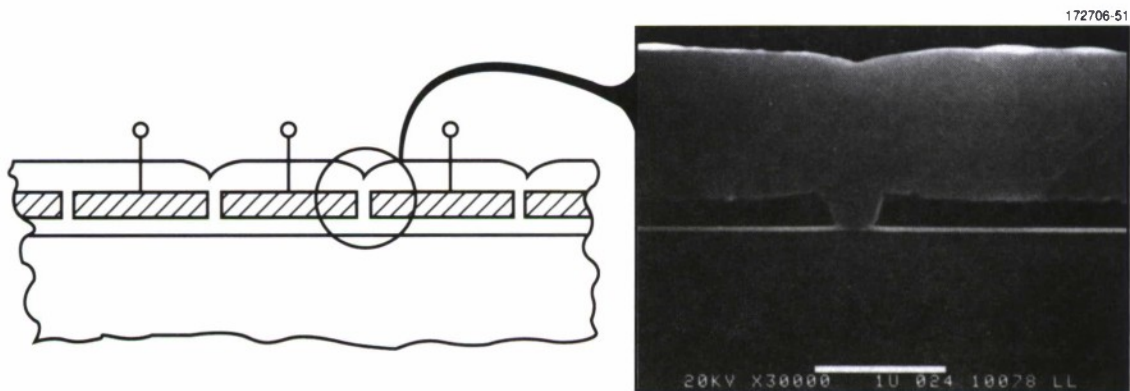


Figure 6-3. Cross section of the finished non-overlapping-gate CCD, showing the submicrometer spacings.

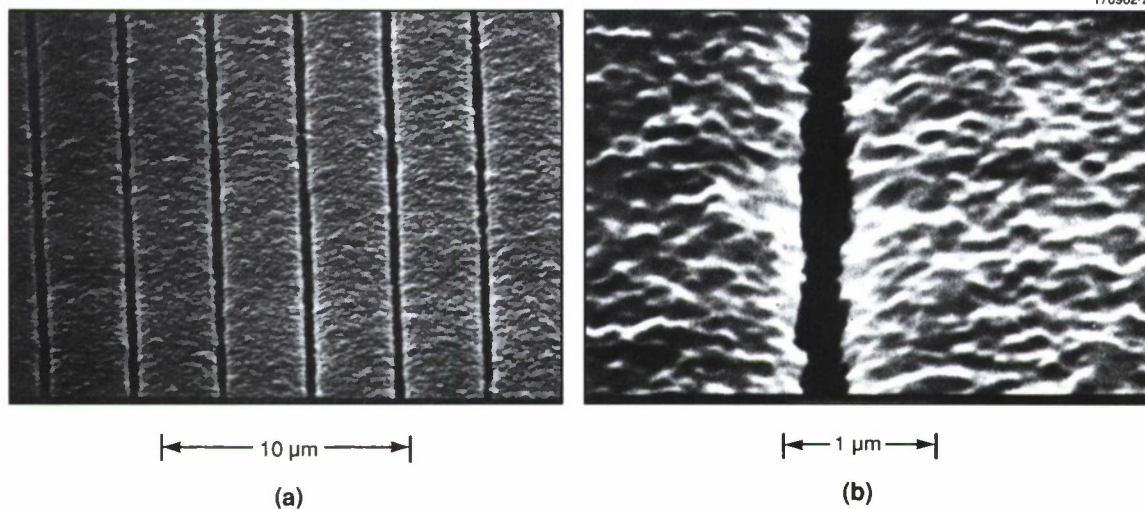


Figure 6-4. (a) Top view of array of CCD polysilicon electrodes. (b) Expanded view showing etched submicrometer spacing between the electrodes.

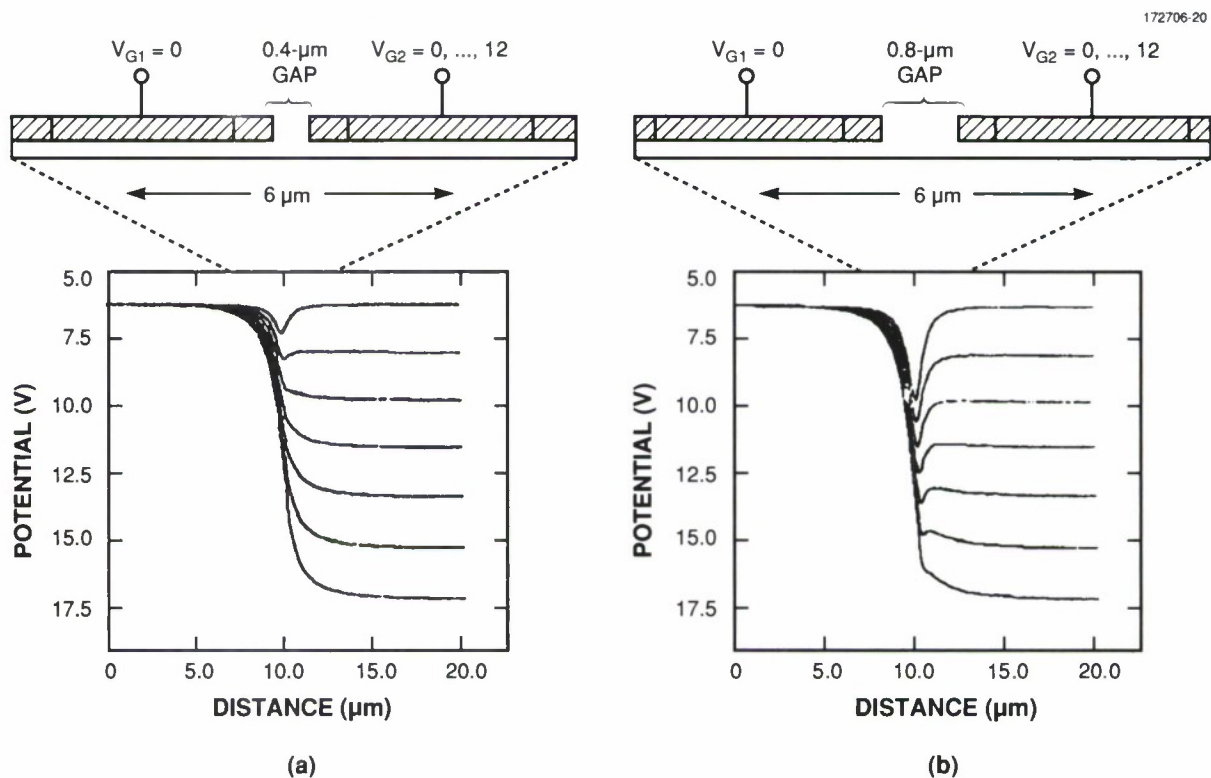


Figure 6-5. Channel potential under two successive electrodes separated by submicrometer spacings of (a) $0.4\ \mu\text{m}$ and (b) $0.8\ \mu\text{m}$. An effective oxide surface charge of 10^{11} charges/ cm^2 and a gate-oxide thickness of $800\ \text{nm}$ were used.

In summary, we have developed a process for the fabrication of non-overlapping-gate CCDs that uses conventional techniques together with LOCOS over polysilicon to produce single-level polysilicon CCDs with $0.4\text{-}\mu\text{m}$ electrode spacings. Simulation measurements indicate that the electrode spacings must be $< 0.4\text{ }\mu\text{m}$ to achieve adequately low CTI. Modifying the properties of the polysilicon through improved deposition and annealing schedules may result in more uniform polysilicon edges after LOCOS as well as improvement in the yield of devices with electrode spacings $< 0.4\text{ }\mu\text{m}$.

C. M. Huang	A. H. Loomis
G. A. Lincoln	A. L. Lattes
R. K. Reich	B. E. Burke

REFERENCES

1. M. H. White, D. R. Lampe, F. C. Blaha, and I. A. Mack, *IEEE J. Solid-State Circuits* **SC-9**, 1 (1974).
2. F. H. Yang, M. M. Blouke, D. L. Heidtmann, B. Corrie, L. D. Riley, and H. H. Marsh, *Proc. SPIE* **1071**, 213 (1989).
3. C. K. Kim, *Int. Electron Devices Mtg. Tech. Dig.* (IEEE, New York, 1974), p. 55.
4. J. W. Slotboom, J. W. Bartsen, J. G. Dil, M. J. M. Pelgrom, J. J. M. J. de Klerk, R. D. J. Verhaar, C. A. H. Juffermans, D. J. Vinton, and J. P. Swetman, *Int. Electron Devices Mtg. Tech. Dig.* (IEEE, New York, 1984), p. 308.

7. ANALOG DEVICE TECHNOLOGY

7.1 OFF-AXIS SPUTTER DEPOSITION OF $\text{YBa}_2\text{Cu}_3\text{O}_{7-x}$

Superconducting $\text{YBa}_2\text{Cu}_3\text{O}_{7-x}$ (YBCO) thin films have been deposited on LaAlO_3 substrates by single-target off-axis magnetron sputtering, the simplest method to produce high-quality YBCO thin films in situ. The target, which is a high-density pressed powder of stoichiometric superconducting YBCO, is situated at a 90° angle to the substrate to minimize the adverse effects of film bombardment, which is probably caused by negative oxygen ions originating at the target. To understand the relationship between film deposition parameters and resulting film properties, the films were deposited over a wide range of conditions by varying the substrate temperature and oxygen pressure while keeping the RF sputtering power constant at 125 W. The oxygen pressure was varied from 10 to 100 mTorr with the argon pressure adjusted to maintain a total pressure of 160 mTorr, and the substrate temperature was varied from 640 to 780°C . Under these deposition conditions, summarized in Figure 7-1, the growth rate of the films increased with increasing substrate temperature and decreasing oxygen pressure, varying from 4.2 to $11.4 \text{ \AA}/\text{min}$.

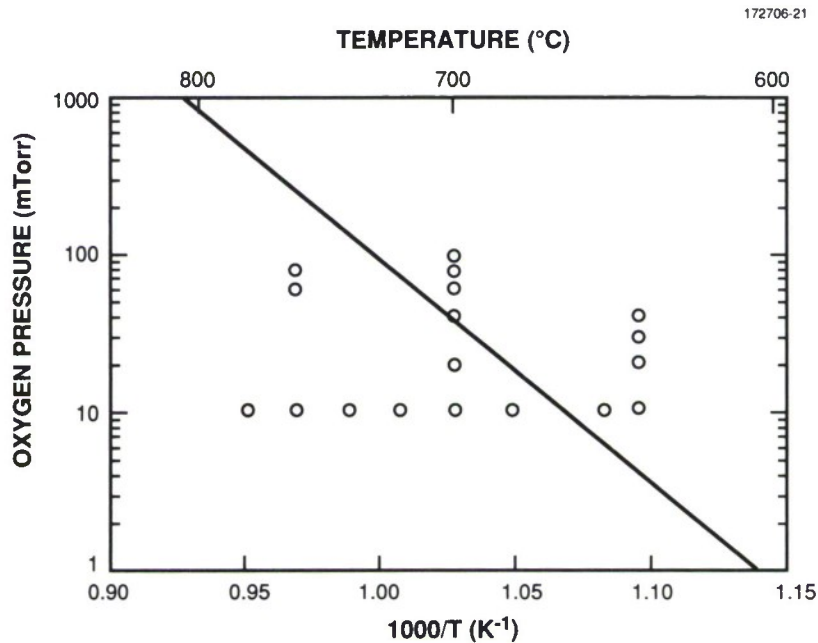


Figure 7-1. Summary of the deposition conditions used to produce in-situ superconducting YBCO. The solid line indicates the perovskite stability line established by Bormann and Nölting [3]. Under equilibrium conditions the perovskite structure of bulk YBCO is stable above the line and unstable below it.

After deposition, all films were cooled in the same way: the substrate temperature was decreased to 400°C in 20 min and held at 400°C for 1 h, while the oxygen pressure was linearly ramped at a rate of 2 Torr/min. During this oxygen “soak,” oxygen diffuses into the YBCO lattice and converts the film from the tetragonal semiconducting phase to the orthorhombic superconducting phase [1]. Changes in oxygen content are accommodated by changes in the oxygen occupancy of the oxygen sites in the Cu-O plane between Ba ions, usually referred to as chain sites [1]. Since the films were identically cooled, differences in film properties resulting from different oxygen pressures during deposition are believed not to result from differences in the occupancy of chain sites.

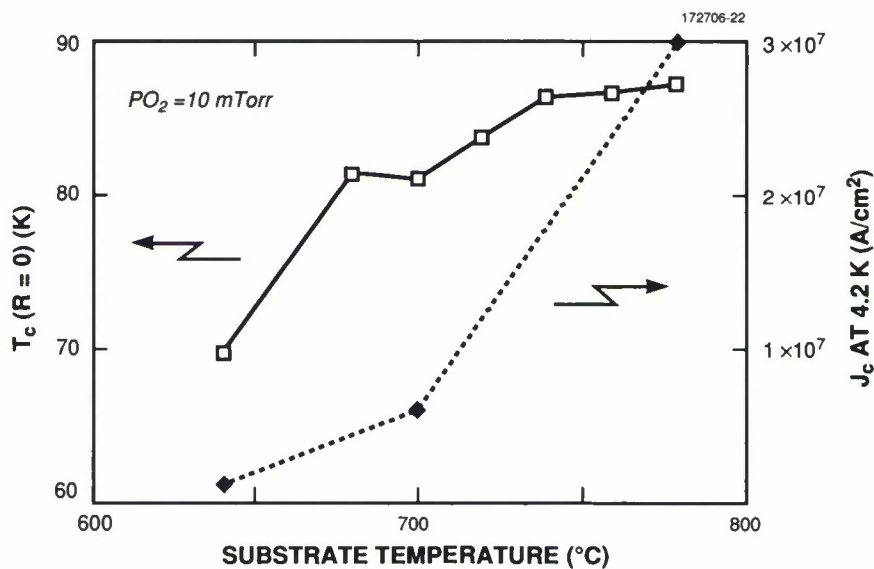
As the substrate temperature and the oxygen pressure are varied during deposition, the electrical and structural properties of the films change. The variation of transition temperature T_c and critical current density J_c as a function of substrate temperature is shown in Figure 7-2(a). For a given oxygen pressure, both T_c and J_c increase as the substrate temperature increases. The variation of T_c with oxygen pressure is shown in Figure 7-2(b). The value of T_c ($R = 0$) tends to increase with increasing oxygen pressure during the deposition. The highest T_c ($R = 0$) measured was 90.5 K for a film deposited at a substrate temperature of 760°C with an oxygen pressure of 80 mTorr. The highest J_c measured was 3.0×10^7 A/cm² at 4.2 K for a film deposited at 780°C with an oxygen pressure of 10 mTorr.

The surface morphology of our films was investigated using scanning electron microscopy. All films, except those grown at 640°C, exhibit surface agglomerates, which have been identified by scanning Auger spectroscopy as both Cu and Ba rich. These agglomerates increase in size and decrease in areal density with increasing temperature and oxygen pressure. The smooth surface morphology of films deposited at low temperature make them highly desirable for fabricating multilayer structures.

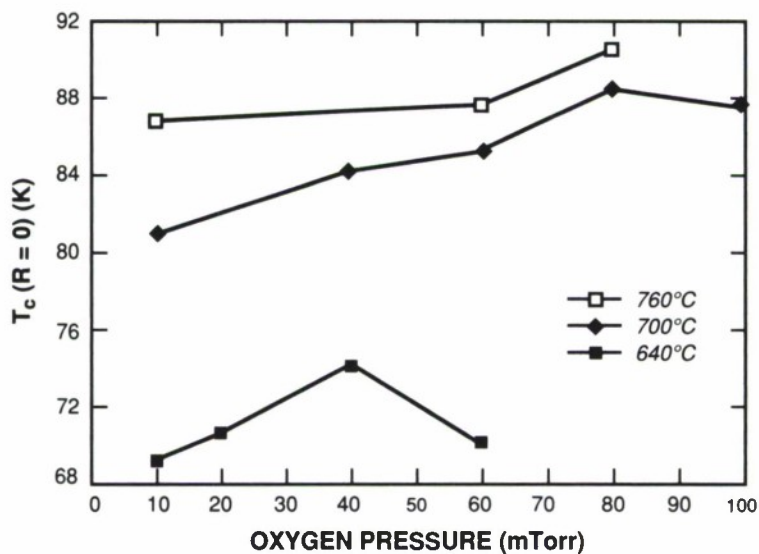
The epitaxial growth orientation of the films was also found to vary with deposition conditions. Fully oxygenated bulk YBCO has the following lattice parameters: $a = 3.819$ Å, $b = 3.891$ Å, and $c = 11.689$ Å. The differences in lattice constants for a , b , and $c/3$ are small, which means that there are three possible growth orientations on a cubic lattice-matched substrate. In our experiments, films deposited at high substrate temperatures were oriented with the c -axis perpendicular to the substrate, while films deposited at 640°C were oriented with the a -axis perpendicular to the substrate. Figure 7-3 compares the x-ray diffraction patterns of two films, one deposited at 780°C and the other at 640°C. For the 780°C film the (00ℓ) peaks are very intense, while for the 640°C film they are absent. For the film deposited at 640°C the (400) peak is the only $(h00)$ peak resolved because of the very small difference in lattice constant between the film and the substrate. Films with a -axis orientation are of great technological importance for tunnel devices, since the superconducting coherence length is ~ 13 Å parallel to the Cu-O planes (a - b planes) and only 2 Å perpendicular to these planes [2].

Formation of in-situ superconducting YBCO thin films resulted under all deposition conditions explored, including those outside the region of thermodynamic stability for bulk YBCO. Figure 7-1 shows the YBCO perovskite stability line established by Bormann and Nölting [3] below which, under equilibrium conditions, bulk YBCO decomposes. The role of oxygen for thin-film formation is twofold: the oxygen partial pressure must be high enough to allow formation of the perovskite structure and also to prevent decomposition of the film. Even at conditions far from the stability line, 780°C and 10 mTorr of oxygen, a high-quality film with T_c of 87 K and J_c of 3×10^7 A/cm² was deposited. One possible explanation for this is the presence of

atomic oxygen in the plasma, which has been confirmed by the observation of the 5330- and 6158-Å atomic oxygen lines by optical emission spectroscopy [4]. Since atomic oxygen is more reactive than molecular oxygen, less atomic oxygen is needed to grow a YBCO film at a given temperature. However, it should be noted that although the films are deposited from a stoichiometric target, the films are off stoichiometry with a typical cation ratio of 1.2:2:3.1. The resulting defects and strain in the films probably affect stability.



(a)



(b)

Figure 7-2. (a) Variation of T_c and J_c with substrate temperature for films deposited using an oxygen pressure of 10 mTorr. The argon pressure was 150 mTorr. (b) Variation of T_c with oxygen pressure for films deposited at substrate temperatures of 760, 700, and 640°C. The argon pressure was adjusted to maintain a total pressure of 160 mTorr.

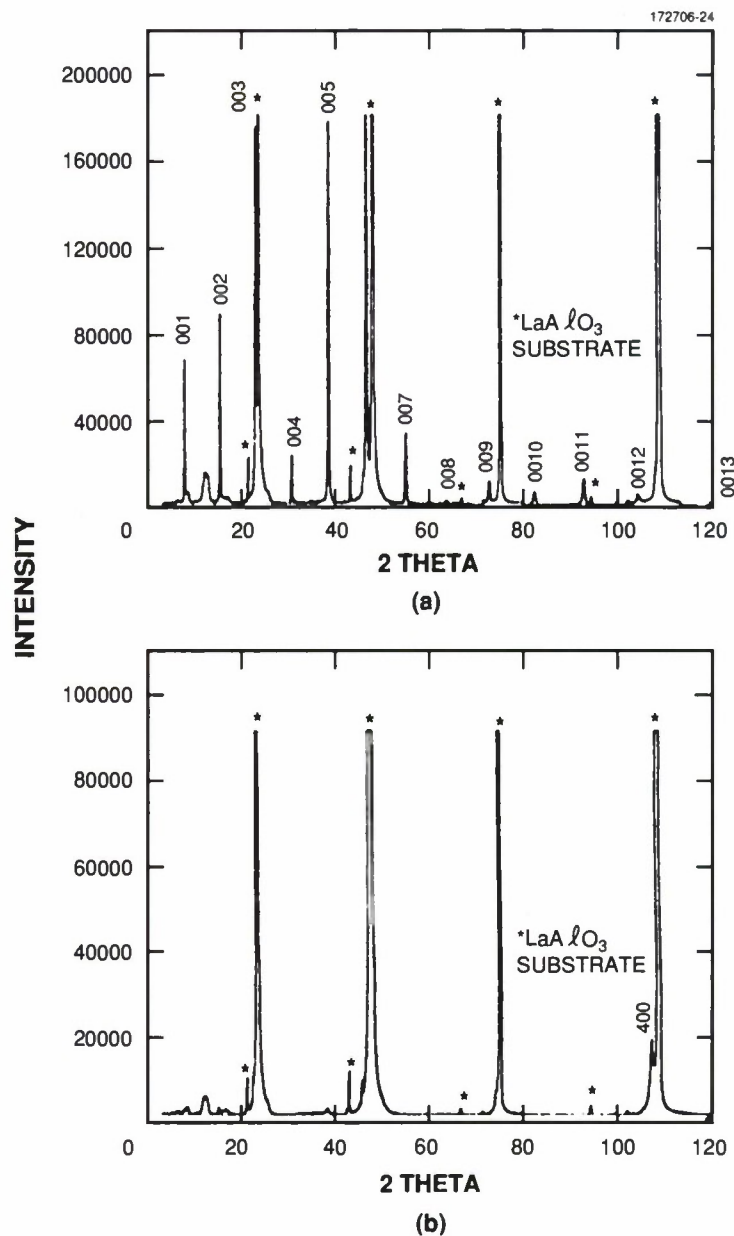


Figure 7-3. X-ray diffraction pattern of (a) a c-axis-oriented film deposited at 780°C using an oxygen pressure of 10 mTorr, and (b) an a-axis-oriented film deposited at 640°C using an oxygen pressure of 20 mTorr.

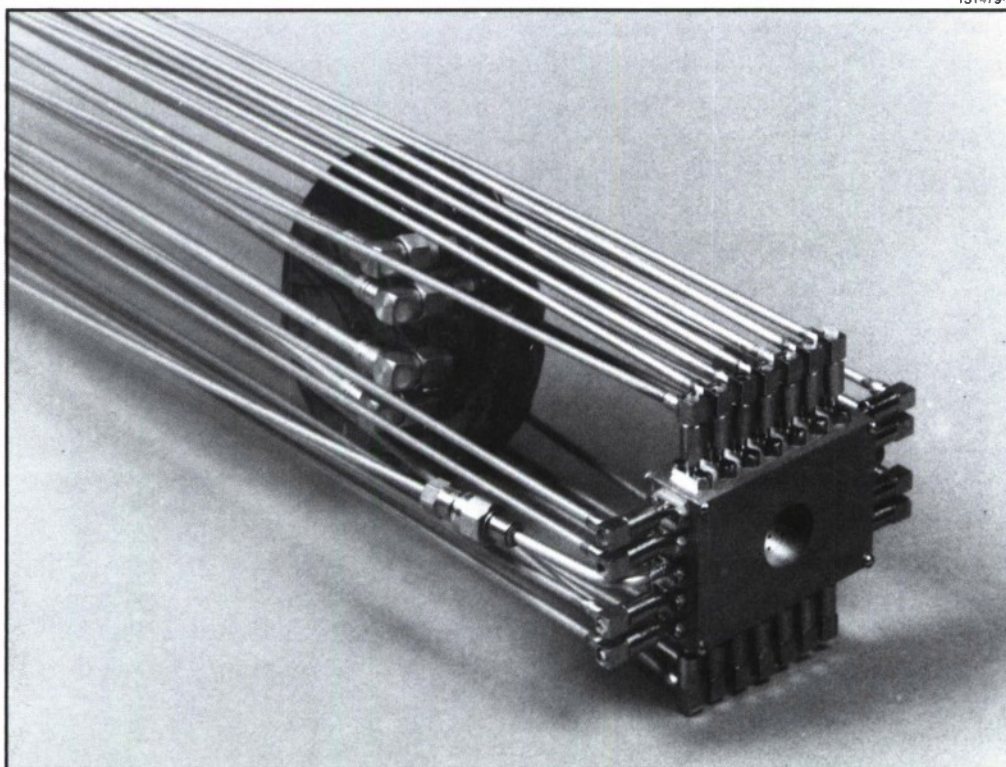
In summary, in-situ superconducting YBCO thin films have been fabricated over a wide range of substrate temperatures and oxygen pressures, including conditions outside the region of thermodynamic stability of the perovskite structure. Film properties such as T_c , J_c , surface morphology, and crystalline orientation were found to vary systematically with substrate temperature and oxygen pressure during deposition.

Since deposition conditions that optimize one film property may degrade another, deposition conditions must be selected to suit a desired application.

A. C. Westerheim
L. S. Yu-Jahnes
A. C. Anderson

7.2 INTEGRATION OF SUPERCONDUCTIVE DEVICES FOR ANALOG-SIGNAL-PROCESSING APPLICATIONS

A prototype spread-spectrum communications subsystem has been demonstrated that integrates two superconductive components, a dispersive delay line [5] and a time-integrating correlator [6]. In this system the delay line and correlator are individually packaged and mounted on the same cryogenic probe and immersed in liquid He. Figure 7-4 shows the bottom end of the probe with both devices attached.



131479-2

Figure 7-4. End view of the cryogenic probe, with the superconductive dispersive delay line (circular package) and time-integrating correlator (rectangular package) mounted.

A block diagram of the experimental setup is shown in Figure 7-5. The superconductive dispersive delay line is Hamming weighted with a 2.6-GHz bandwidth centered at 4 GHz. The device is used to generate chirp waveforms on application of a wideband impulse to its input. Since the delay line has a dispersion time of 38 ns, it is repetitively fed impulses to create a waveform $\sim 3 \mu\text{s}$ in duration. This wideband waveform is split into two paths. One path passes through a variable-length delay line used to simulate propagation through the atmosphere, while the other leads directly into the tapped delay line of the superconductive time-integrating correlator. The signal at this input to the correlator is the reference waveform in this spread-spectrum application.

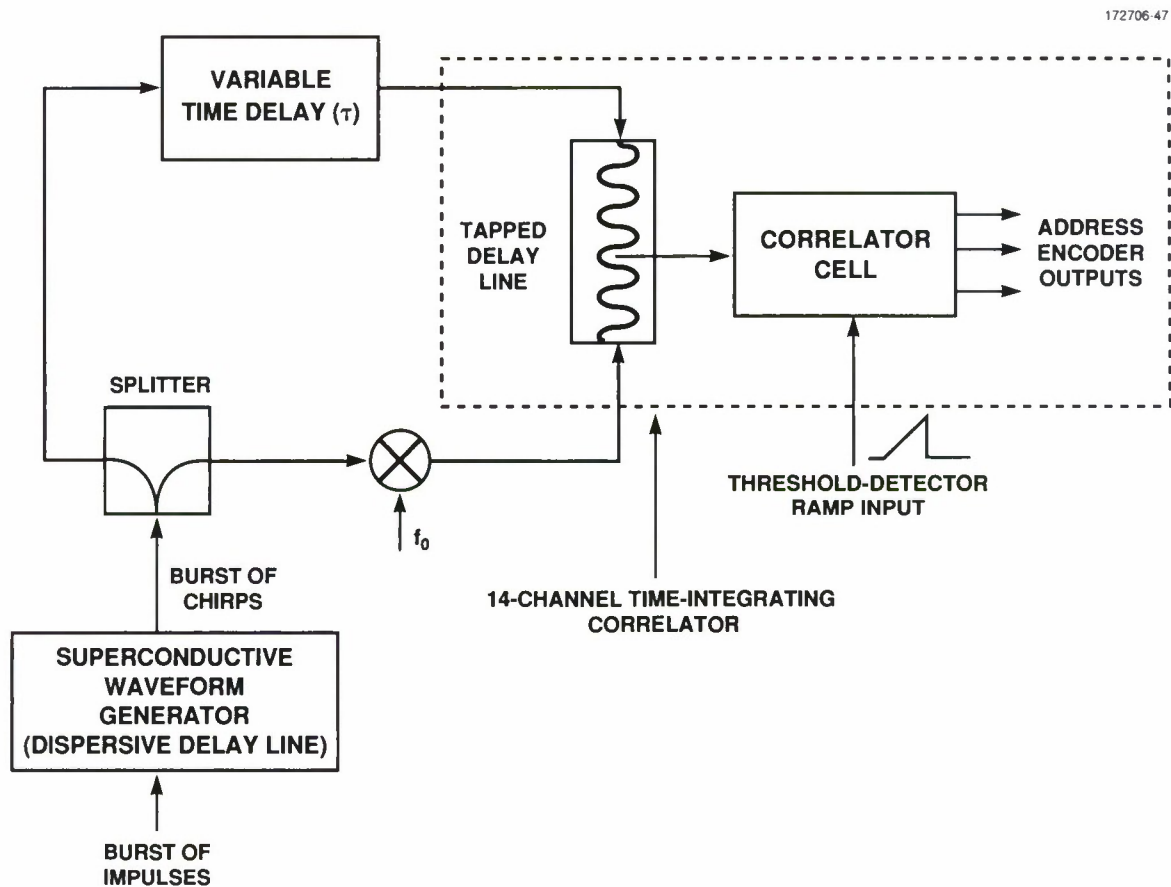


Figure 7-5. Block diagram showing the integration of superconductive components to measure the autocorrelation of wideband chirp waveforms.

The superconductive correlator has 14 parallel channels with the output of each channel controlling the input to a digital address encoder, as shown in Figure 7-6. All components in the figure are integrated into a single circuit on a 1×1.4 -in. silicon substrate. As described previously [6], the timing of the address encoder output reflects the time-integrated correlation value, while the digital address reflects the correlator channel reporting its contents. In operation the correlator has supported $3\text{-}\mu\text{s}$ -long waveforms with bandwidths $> 2.6\text{ GHz}$.

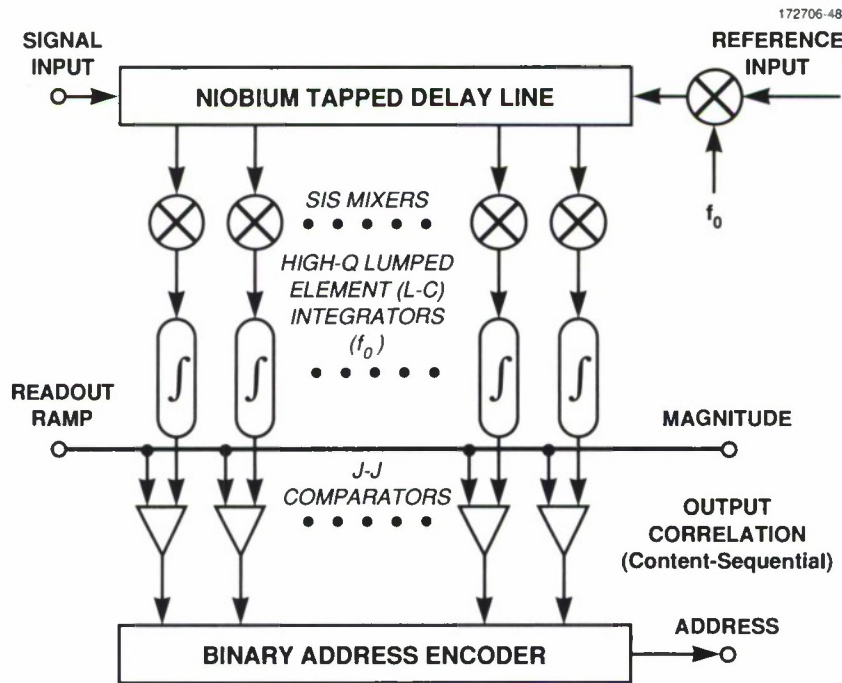


Figure 7-6. Block diagram of time-integrating correlator showing the on-chip integration of analog and digital superconductive circuitry.

The plot in Figure 7-7(a) shows the reconstructed correlation output measured by correlator channel 8 as a function of the synchronization offset introduced by the variable-length delay line shown in Figure 7-5. The agreement with the mathematically calculated correlation function of ideal Hamming-weighted chirp waveforms, shown in Figure 7-7(b), is excellent.

J. B. Green
R. R. Boisvert

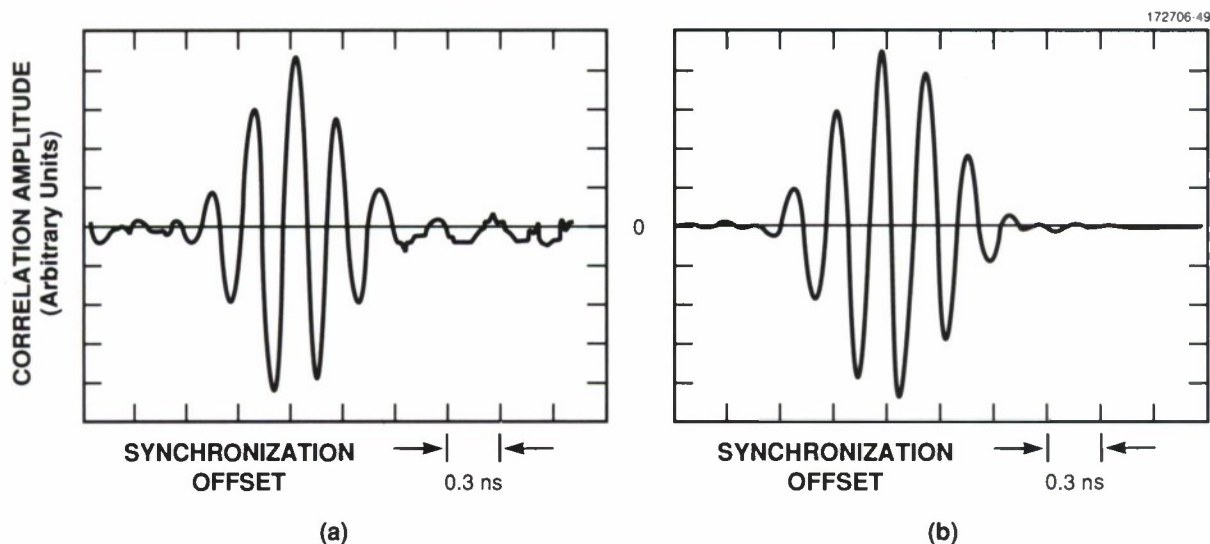


Figure 7-7. (a) Reconstructed output of the time-integrating correlator, showing the measured autocorrelation of a 2.6-GHz chirp waveform. (b) Mathematical calculation of the chirp autocorrelation function.

REFERENCES

1. J. D. Jorgensen, M. A. Beno, D. G. Hinks, L. Soderholm, K. J. Volin, R. L. Hitterman, J. D. Grace, I. K. Schuller, C. U. Segre, K. Zhang, and M. S. Kleefish, *Phys. Rev. B* **36**, 3608 (1987).
2. B. Oh, K. Char, A. D. Kent, M. Naito, M. R. Beasley, T. H. Geballe, R. H. Hammond, and A. Kapitulnik, *Phys. Rev. B* **37**, 7861 (1988).
3. R. Bormann and J. Nölting, *Appl. Phys. Lett.* **54**, 2148 (1989).
4. A. C. Westerheim, L-S. Yu-Jahnes, and A. C. Anderson, *IEEE Trans. Magn.* **27**, 1001 (1991).
5. R. S. Withers, A. C. Anderson, J. B. Green, and S. A. Reible, *IEEE Trans. Magn.* **MAG-21**, 186 (1985).
6. J. B. Green, A. C. Anderson, and R. S. Withers, *Proc. SPIE* **879**, 71 (1988).

